DOCTOR OF PHILOSOPHY

Electrokinetic manipulation of particles : computer aided studies.

Hughes, Michael Pycraft.

Award date:
1995

Awarding institution:
Bangor University

A thesis submitted to the University of Wales

in candidature for the degree of

Doctor of Philosophy

Electrokinetic Manipulation of Particles: Computer Aided Studies

by

Michael Pycraft Hughes M.Eng.

School of Electronic Engineering and Computer Systems

University of Wales

Bangor, Gwynedd

1995

To my beloved wife

Alisan:

$M\text{-}2A,\ 4(\infty)$

Acknowledgements

I would like to thank the following for their support in the undertaking of the work in this thesis:

Firstly, great credit for this work must go to my supervisor, Professor Ron Pethig, to whom I am greatly indebted. I am also grateful to Drs Peter Gascoyne and Fred Becker for the organisation of, and support and advice during, my stay at the University of Texas MD Anderson Cancer Center.

Thanks also are due to Dr Julian Burt and Dr Xiao-Bo Wang for their advice and guidance in the formulation of the Finite Element and Moment Method models respectively.

I would also like to thank my colleagues, both at UWB and UTMDACC: Stephen Bellis, Ka Lok Chan, Ying Huang, John Kerslake, Richard Lee, Gerard & Sian Markx, Frank Marini, Jamileh Noshari, John Phelps, Robin Rhea, Juliette Rousselet, Mark Talary, Jody Vykoukal, Lionel Watkins and Xiao-Feng Zhou, for their friendship, advice and valuable discussions.

Finally I wish to thank my wife Alisan and my parents Eric and Ceri for their support, patience and love during this studentship.

Summary

AC electrokinetics - encompassing dielectrophoresis, electrorotation and travelling wave dielectrophoresis - is the phenomenon of induced motion of colloidal particles through the application of AC electric fields. Motion may be induced in either rotational or translational senses, and the nature of the induced force is dependent on the time-dependent morphology of the electric field, as well as the dielectric characteristics of the particle and the suspending medium.

The work presented in this thesis is concerned with the examination of the underlying principles of this phenomenon in a variety of practical applications through the medium of computer simulation. Various computer models are described, with the two used for the simulations presented here being described in greater detail. Applying these models to separate cases of dielectrophoresis, electrorotation and travelling wave dielectrophoresis, the nature of the force distributions may be studies. This allows a more thorough study of such phenomena than is possible through the experimental study of particle motion.

A primary function of this work is to examine the means of optimising electrode design for particle manipulation, separation and characterisation through the application of AC electrokinetic forces. As a consequence of this study, the underlying principles of force distribution have become apparent. In many cases, the detailed study of electric fields and forces generated near the electrodes have demonstrated previously unknown particle behaviours, many of which have been confirmed by experimentation.

Contents

Chapter 1
Introduction and Aims of Work

1.1 Introduction

The study of AC electrokinetics - the induced motion of colloidal particles through the application of alternating electric fields - is one which is gaining an increasing interest from a wide variety of researchers in many disciplines. The ability to electrically manipulate bioparticles is being investigated by researchers for possible applications in medical diagnostics and treatment. For example, observation of electrokinetic effects on cells provides a non-invasive method for the study of the dielectric properties of the cell interior. Also, manipulation of microscopic objects offers great potential in the expanding nanotechnology field.

The nature of AC electrokinetics is such that motion is induced by the interaction of the dielectric properties of the bioparticles with the applied electric fiield, rather than any charge carried by the particles themselves [1] as is the case in electrophoresis. The electric field morphology is therefore of major significance in determining the direction of particle motion. Whilst generating electric fields in the laboratory is not a difficult task, the precise form the electric field takes and hence the exact motion particles within such fields will undergo is potentially far more difficult to predict. With the introduction of electrodes which use differing phases of the electric fields to generate more complex motive patterns the only accurate method of interpreting the particle motion observed in experimentation is through the building of computer models. To this end, the work presented here analyses the electric fields and applied forces as generated by three separate but related phenomena; dielectrophoresis, electrorotation and travelling-wave dielectrophoresis.

Dielectrophoresis is the translational motion of particles induced by polarisation effects in non-uniform electric fields, as defined by Pohl [2] and described further by Pethig [3]. Consider a particle suspended in a medium of lesser polarisability and subjected to a non-uniform electric field, such as that shown in figure 1.1(a). The electric field induces a dipole in the particle, the poles of which interact with the electric field and generate electrostatic forces. Due to the greater electric field strength across the pole facing the pin-shaped electrode, the force induced is greater than the force induced on the opposing side of the particle and a net force towards the pin electrode is exerted. This force will act towards the region of greatest electric field, regardless of whether the pin electrode is positively or negatively charged, and will thus also be present when an AC electric field is applied between the electrodes. This motion of the particle is termed *positive dielectrophoresis.* However, if the particle is suspended in a medium of higher polarisability than itself, the force on the particle is directed away from the high-field regions, towards the low-field regions (see figure 1.1b). This motion is referred to as *negative dielectrophoresis.* Since the polarisability of the particle and medium are frequency dependent, it is possible for a particle to experience either positive or negative dielectrophoresis according to the frequency of the applied electric field.

The first experimental observations of the motion of particles in non-uniform electric fields were undertaken by Hatescheck and Thorne [4], in the study of nickel suspended in toluene and benzene. The phenomenon was named dielectrophoresis by Pohl in 1951 [5], who later published an in-depth treatise on the subject in his 1978 book of the same title [2]. Pohl's work advanced the use of dielectrophoresis for investigating the properties of suspensoids, and for providing a means of separating particles from suspension.

Similar investigations have been conducted using a frequency-based examination of dielectrophoretic collection rates of populations of cells to study dielectric properties of yeast [6] and bacteria [7]. Practical applications of dielectrophoresis have included the building of separators for the removal of PVC polmers [8], lubricating oils [9], and minerals [10] from solution. The use of positive and negative dielecrophoresis has

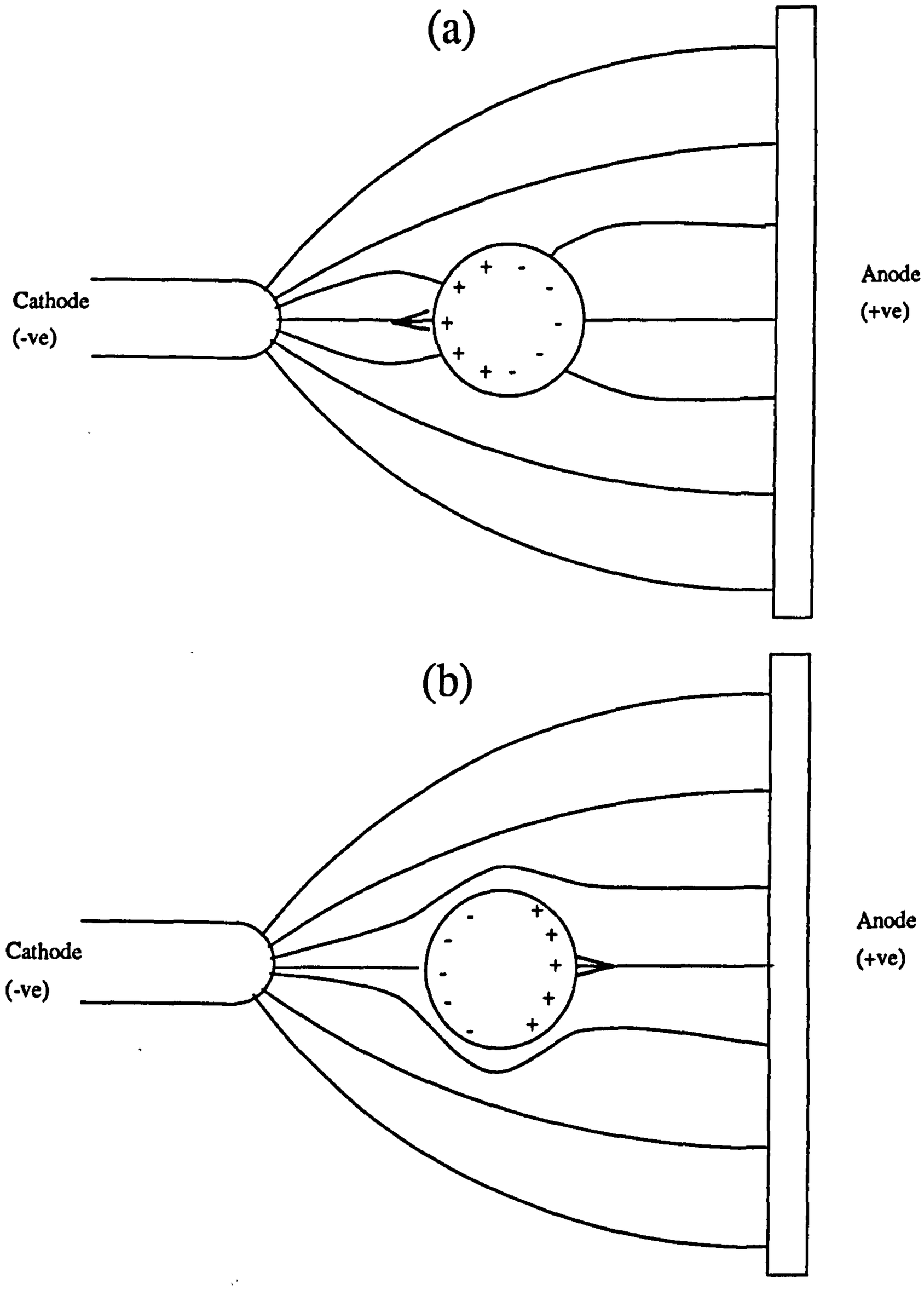

1.1 A neutral particle in a non-uniform electric field. (a) If the particle is of greater polarisability than the surrounding medium, the diplole aligns with the electric field and the particle experiences positive dielectrophoresis. (b) If the particle is less polarisable, the dipole orients counter to the applied field and the particle undergoes negative dielectrophoresis.

been used to separate mixtures of viable and non-viable yeast cells [11] and mixtures of healthy and leukaemic blood cells [12]. Recent work by Rousselet *et al* [13] has applied dielectrophoresis to the induction of continuous linear motion of particles, expanding on the basic concept of dielectrophoresis as a means of trapping particles in a specific region in space.

Another important form of AC electrokinetics is that of *electrorotation*, the continuous rotation of particles suspended within rotating electric fields. Cell rotation was observed and reported by experiments on AC dielectrophoresis [eg 14], and was later suggested to be the result of the dipole-dipole interaction of neighbouring cells [15]. This led Arnold and Zimmerman [16] to the principle of suspending single particles in a rotating field, and thus to a more amenable means of studying the phenomenon.

Electrorotation occurs when a dipole is induced by a rotating electric field, as shown in figure 1.2. The dipole takes a finite time (the relaxation time) to establish, by which time the electric field has rotated slightly. There is thus a phase lag between the orientation of the electric field and that of the dipole moment, and thus a torque is induced as the dipole moves to re-orient itself with the electric field. Due to the continuous rotation of the electric field, the torque is induced continually and the cell rotates. The direction of rotation is determined by the phase angle between the dipole moment and the electric field; if the phase lag is less than 180° the particle rotation will follow that of the applied field, referred to as co-field rotation. If the phase angle is greater than 180° the shortest path for the dipole to align with the electric field is by rotating in a counterwise fashion to that of the electric field, and hence particle rotation will act in this direction (anti-field rotation).

As with dielectrophoresis, the rate and direction of cell rotation is related to the dielectric properties of both the particle and the suspending medium. The technique can thus be used as an investigative technique for studying these properties. Electrorotation has been used to study the dielectric properties of matter, such as the interior properties of biological cells [17]. The ease and accuracy of observation of the effect - that of a continuous rotation of small numbers of particles, rather than studying

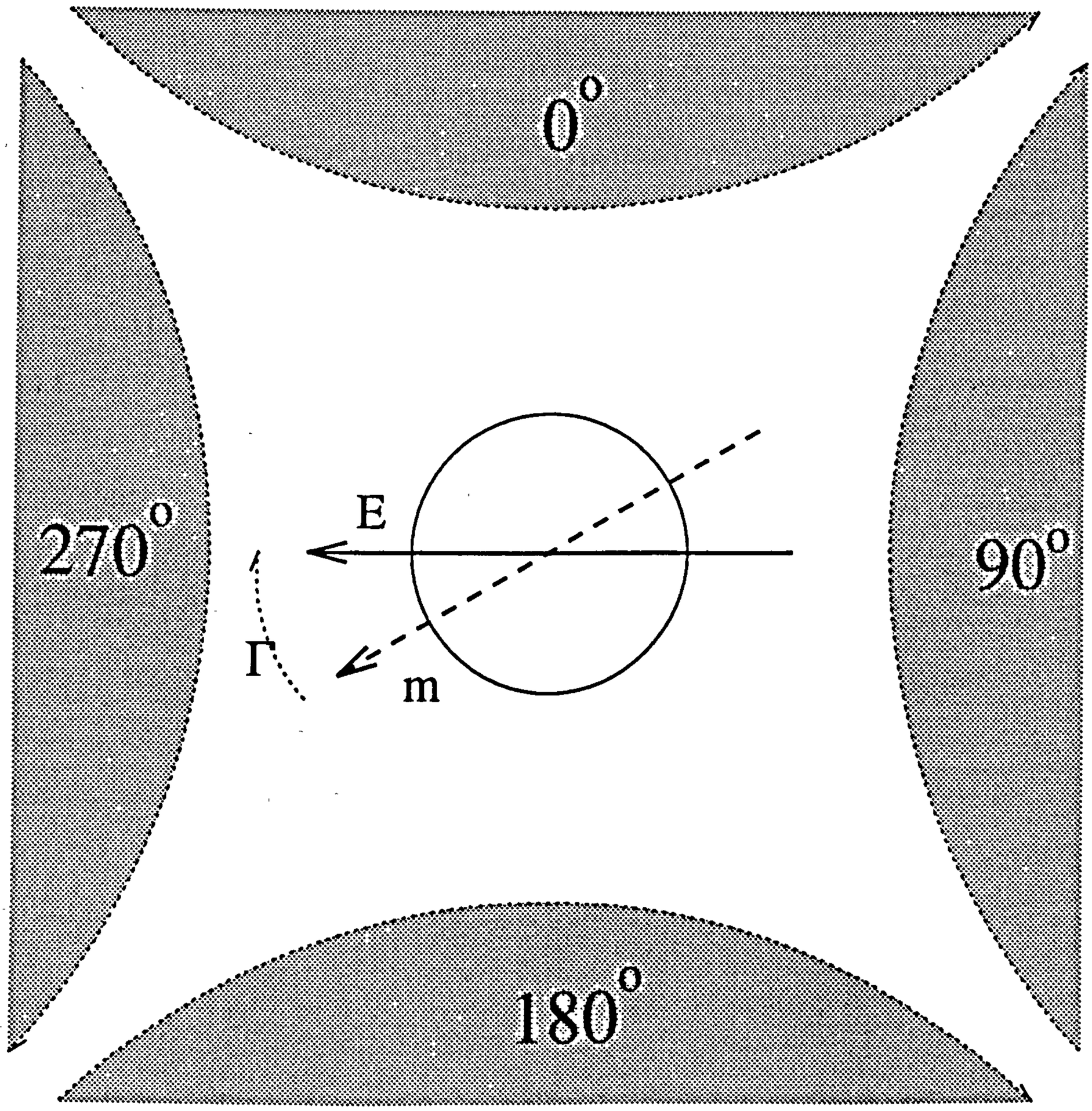

1.2 When a dielectric particle is suspended in a rotating electric field E, the dipole moment forms out-of-phase with the field due to the relaxation time for the dipole to form. This phase difference generates a torque Γ which causes the particle to rotate.

the collection rates of large populations - have resulted in electrorotation largely supplanting dielectrophoresis as a means of investigating subtle variations in the dielectric properties of particles, such as the aggregation of biofilms on the surface of beads [18].

The final example of AC electrokinetics discussed here is that of *travelling-wave dielectrophoresis*. The phenomenon was first reported by Masuda *et al* [19], where the electric fields "travel" along a series of bar-shaped electrodes where low frequency (0.1Hz to 100Hz) sinusoidal potentials, advanced 120° for each successive electrode, were applied. This was found to induce controlled translational motion in lycopodium particles [19] and red blood cells [20]. At low frequencies the translational force was largely electrophoretic, and it was proposed that such travelling fields could eventually find application in the separation of particles according to their size or electrical charge. However, later work by Fuhr and co-workers [21], using applied travelling fields at much higher frequency ranges (10 kHz to 30 MHz), demonstrated the induction of linear motion in pollen and cellulose particles. Huang *et al* [22] have used travelling fields at frequencies between 1 kHz and 10 MHz to linearly move yeast cells and separate them from a heterogeneous population of yeast and bacteria, and have demonstrated that the mechanism inducing travelling motion at these higher frequencies is dielectrophoretic, rather than electrophoretic, in origin.

Travelling-wave dielectrophoresis is effectively an extension of the principle of electrorotation to include a linear case. As shown in figure 1.3, an AC electric field is generated which travels linearly along a series of electrodes. Particles suspended within the field establish dipoles which, due to the relaxation time, are displaced from the regions of high electric field. This induces a force in the particle as the dipole moves to align with the field. The principle of phase lag remains, in that as the applied travelling wave is a sinusoid, the dipole occupies a physical space at a given part of the cycle. If the dipole lags within half a cycle of the applied field net motion acts in the direction of the applied field, whilst a lag greater than this results in motion counter to the applied field.

0°			180°
270°			90°
180°	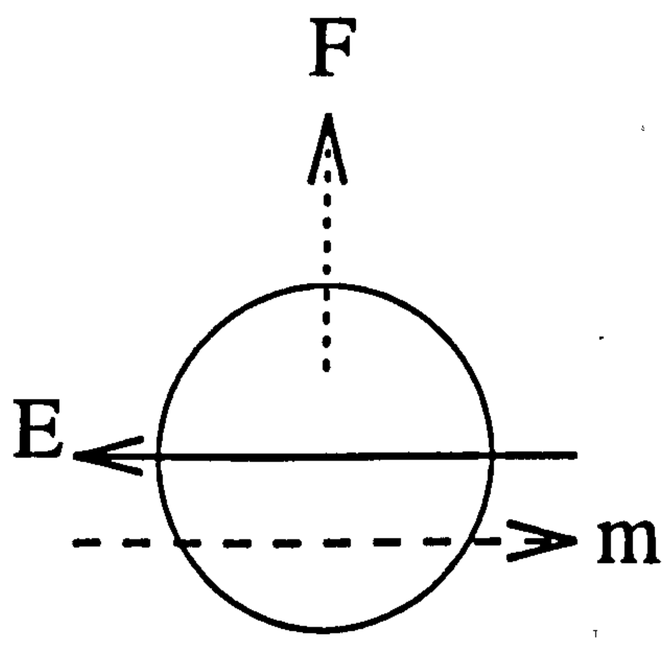		0°
90°			270°
0°			180°

1.3 When . sinusoidal potentials are applied to a continuous set of phase-shifted electrodes, a travelling electric field is generated. Particles within this field will attempt to orient along the field. Due to the relaxation time taken to form, the dipole will be displaced from the field, and the force generated by the dipole moving to align with the field causes the particle to undergo travelling-wave dielectrophoresis.

1.2 Aims of Work

The aim of this thesis is to examine these phenomena through the medium of computer simulation of these electric fields, and the forces experienced by particles suspended within such fields. Since the majority of electrodes used in AC electrokinetics produce non-analytical electric field morphologies (notable exceptions of which include polynomial electrodes, [23]), numerical methods of determining them must be employed. Two approaches are considered here for the calculation of electric fields. The first method, referred to as the Charge Density or Moment Method, derives the electric field by calculation of the charge distribution across the electrode surfaces, and subsequently by considering the contribution this charge makes to the electric field at a given point. This method requires that the charge distribution across the electrodes is divided into subareas, each of which is small enough to have effectively uniform charge across it. Based on the works of Maxwell, the method was originally advanced for the calculation of capacitance across a square [24], but has since been employed in determining charge distribution in parallel-plate capacitors [25] and electron beam trajectories through non-uniform electric fields [26]. More recently, a study by Huang *et al* [27] examined dielectrophoretic forces generated by castellated electrodes using this method, and it has also been employed by Schnelle *et al* to examine forces within electrode field cages [28].

Another method considered here is the Finite Element Method. This was originally developed for solving mechanical stresses in Civil Engineering, but was later adopted for calculating electric fields. This is achieved by dividing the space between fixed potentials into a number of elements, and solving Laplace's Equation locally across each element. These results are then solved as a series of simultaneous equations to determine the overall electric field. This method is generally used for electric field calculation [eg. 29], and has been applied recently in a limited study of travelling wave effects in focussing electrode arrays [30]. Both methods are explained in greater depth in Chapter 2, where a comparison is presented for simulations of a single problem, and the two methods are evaluated for various applications within this study.

1.3 References

[1] Grant EH, Sheppard RJ and South GP 1978 *Dielectric Behaviour of Biological Molecules in Solution* (Oxford: Clarendon Press)

[2] Pohl HA 1978 *Dielectrophoresis* (Cambridge: Cambridge University Press)

[3] Pethig R 1979 *Dielectric and Electronic Properties of Materials* (Chichester: Wiley)

[4] Hateschek E and Thorne PCL 1923 *Roy. Soc. Proc.* **103** 276-284

[5] Pohl HA 1951 *J Appl. Phys.* **22** 869-871

[6] Pohl, HA *Methods in Cell Separation,* ed. Catsimpoolas, N (London:Planum Press)

[7] Markx GH, Huang Y, Zhou X-F and Pethig R 1994 *Microbiology* **140** 585-591

[8] Pohl HA 1958 *J Appl. Phys.* **29** 1182-1189

[9] Sasaki A and Dunthorpe OM 1984 *Filtration and Separation* **Nov** 407-410

[10] Lin IJ and Benguigui 1982 *Proc. World Filtr. Conf.* **1** 177-185

[11] Pethig R, Huang Y, Wang X-B and Burt JPH 1992 *J. Phys. D: Appl. Phys.* **25** 881-888

[12] Gascoyne PRC, Huang Y, Pethig R, Vukoukal J and Becker FF 1992 *Meas. Sci. Tech.* **3** 1-7

[13] Rousselet J, Salome L, Ajdari A and Prost J 1994 *Nature* **370** 446-448

[14] Pohl HA and Crane JS 1971 *Biophys J.* **11** 711-727

[15] Holzapfel C, Vienken J and Zimmerman U 1982 *J. Membrane Biol.* **67** 13-26

[16] Arnold WM And Zimmerman U 1982 *Z. Naturforsch* **37c** 908-915

[17] Hölzel 1988 *Med. Biol. Eng. Comp.* **26** 102-105

[18] Zhou X-F, Markx GH, Pethig R and Eastwood IM 1995 *Biochim. Biophys. Acta* (in press)

[19] Masuda S, Washizu M and Iwadare M 1987 *IEEE Trans. Ind. App* **23** 474-480

[20] Masuda S, Washizu M and Kawabata I 1988 *IEEE Trans. Ind. App* **24** 217-222

[21] Fuhr G, Hagedorn R, Müller T, Benecke W, Wagner B and Gimsa J 1991 *Studia Biophysica* **140** 79-102

[22] Huang Y, Wang X-B, Tame J and Pethig R 1993 *J. Phys. D: Appl. Phys.* **26** 312-322

[23] Huang Y and Pethig R 1991 *J. Meas. Sci. Tech.* **2** 1142-1146

[24] Maxwell JC 1892 *A Treatise on Electricity and Magnetism 3rd ed, vol. 1* (Oxford: Oxford University Press)

[25] Reitan DK 1959 *J. Appl. Phys* **30** 172-176

[26] Birtles AB, Mayo BJ and Bennett AW 1973 *Proc. IEE* **120** 213-220

[27] Wang X-B, Huang Y, Burt JPH, Markx GH and Pethig R *1993 J. Phys. D: Appl. Phys* **26** 1278-1285

[28] Schnelle T, Hagedorn R, Fuhr G, Fiedler S and Müller T *1993 Biochim. Biophys. Acta* **1157** 127-140

[29] Simkin J and Trowbridge CW 1980 *IEE Proc* **127** 368-374

[30] Fuhr G, Fiedler S, Müller T, Schnelle T, Glasser H, Lisec T and Wagner B 1994 *Sensors & Actuators A* **41-42** 230-239

Chapter 2

Numerical Methods

2.1 Introduction

This section is intended to familiarise the reader with the mathematical models used in this thesis as a means of determining the electric field across the volume separating two or more electrodes with applied potentials. Analysis of electric fields generally begins with Poisson's equation:

$$\nabla E = -\frac{\rho}{\varepsilon} \tag{2.1}$$

where ρ is the charge density, ε is the permittivity, E is the electric field and ∇ is the del vector operator. There are a limited number of electrode geometries which we may wish to simulate where the potential distribution and hence the electric field may be determined directly from algebraic equations relating to Poisson's equation [eg 1,2]. However, there are many more configurations which are not calculable directly from algebra to provide an exact form of the electric field, and the solution set can only be determined by generating numerical answers at specific points based on an approximate mathematical model. We term these approaches *analytical* and *numerical* analysis respectively. The work presented here deals specifically with the latter case.

Numerical analysis covers a wide variety of mathematical models, some of which are more appropriate to specific problems than others. Presented here are the most prominent methods of numerical analysis in electric field problems, two of which are described in greater detail later.

2.1.1 The Finite Difference Method

Derived from the work of Gauss, Finite Difference models [3] are calculated using a regular mesh superimposed across the volume in which the potential is sought (the "solution space"). At each node of the mesh, Poisson's equation is aproximated to a difference equation relating the potential at the node to the potentials at all the immediately connected nodes. Weightings may be introduced into the difference equation to model the effects of permittivity. The boundary conditions of the model are the known potentials of electrode surfaces.

Originally, solutions were performed by hand using relaxation methods, where the residual of the sum of potentials acting on a given node is minimised from a series of estimated starting values. However, the advent of high-speed computing has brought about the replacement of this method by an iterative approach, where the solution is reached by repeatedly calculating the unknown potentials as a series of simultaneous equations until the answers converge.

The Finite Difference method was the primary means of numerical field analysis from the 1930s to the 1960s when it was largely superceded by Finite Element Analysis. However it is still used in contemporary studies. For example, the recent AC resistor-network model of potential calculation postulated by Hölzel [4] shares many of the principles of Finite Difference Analysis.

2.1.2 The Finite Element Method

Finite Difference models became unfavourable with electrical engineers, as these models required the application of rigid, regular meshes across the solution space. An alternative method, known as the Finite Element method, was soon adopted. This method was originally developed for solving mechanical stresses in Civil Engineering [eg 5], but was later adopted for calculating electric fields [see 6]. As in the Finite Difference method, the solution space is divided up into a series of nodes which define the corners of enclosed elements. However, unlike the Finite Difference method these elements need only loosely follow a general shape such a a cuboid or tetrahedron. As long as the element has the appropriate number of faces and corners it does not need to

be rigidly shaped. The element is transformed locally onto a rigidly defined master element, where Poisson's equation is approximated linearly across that element. The results are mapped onto a system matrix and solved as a series of simultaneous equations to determine the overall electric field. Boundary conditions are mapped as defined potentials at the appropriate nodes.

This method is widely used for electric field calculation [7]. It is available in a number of simulation software packages, forming the calculation engine of integrated CAD/calculation/post-processing software suites. It has many applications in the simulation of any field problems and is used in the calculation of mechanical stress [5], fluid flow [8] and waveguide studies [9]. It is used in chapter 3 as the basis of calculuation of dielectrophoretic ratchets, and is explained in greater depth in section 2.2.

2.1.3 Boundary Element Methods

The Boundary Element method [7] is effectively an extension to the Finite Element Method. The surfaces of the electrodes are discretised into elements, and the potential at enclosing boundaries surrounding the electrodes are coupled to these elements, where the potential is calculated. This method is accurate but highly computationally intensive, and is best applied to functions where far-field considerations are important, or where a core element is surrounded by many layers of material with different dielectric properties [10]. This method has also been combined with Finite Element modelling in some commercial software (eg. SI Eminence, Ansoft Inc) where a Finite Element model is used to determine the solution space, and a Boundary Element model is then used, taking the previous model as its core element, to determine far-field effects. It is also used in determining properties of an enclosed volume from data taken at the outer boundary, such as determining the properties of the human body by examining the electric signals transmitted to electrodes on one part of the skin due to an input potential applied at another part [11].

2.1.4 The Monte Carlo Method

As with the Finite Difference model, the Monte Carlo method [3] involves the superimposition of a mesh across the solution space, with a series of difference equations relating to the potential at the nodes. However, unlike the Finite Difference model, coefficients relating to the difference equations are interpreted as probabilities of a fictitious "particle" moving from one node to its neighbour. By evaluating the random walk of the particle from a given node to a known boundary it is possible to determine the most probable value of the potential at the original node. Permittivity, charge density and other factors may be included in the probability equations.

The method produces a slowly converging result, as the random nature of testing requires extensive recursion in order to "settle" with any degree of confidence. It is common for calculation times to be greater than those for Finite Difference by factors of 20 [3]. It is most commonly applied in circumstances where the methods described elsewhere are not applicable and which study a small solution space. For example, the Monte Carlo method has recently been employed in studies of particle motion in ratchet electrodes [12].

2.1.5 The Method of Moments

This method differs from the others presented here in that, whilst it imposes a mesh across the charge-bearing electrodes it does not impose a grid across the sample space. Referred to as the Charge Density or Moment Method, it differs from the other methods represented here in that the electric field is calculated based on Coulomb's law:

$$E = \sum_i \frac{Q_i}{4\pi\varepsilon r_i^2}\hat{\mathbf{r}}_i \tag{2.2}$$

where E is the electric field at a point due to i charges of magnitude Q_i a distance r_i away along vector $\hat{\mathbf{r}}_i$. This principle was used by Maxwell to calculate the charge across a square area by dividing it into smaller regions across which the charge was approximately uniform [13]. If the surfaces of the electrodes are divided into

sufficiently small subareas, the charge across these subareas can be assumed to be uniformly distributed. The charge on each subarea can be calculated by determining the contribution a unit charge on a given subarea makes to the potential at all other subareas, and by solving against the known potentials on the electrodes the charge distribution may be derived. A similar process is subsequently used to calculate the contributions of the charges on the electrodes to the potential at any arbitrary point.

The Method of Moments is generally applied to electric field problems where charge distribution is required, such as capacitance calculations [14]. The method also has been widely used in dielectrophoresis research, including studies of dielectrophoretic forces on interdigitated electrodes by Huang *et al* [15], and an examination of the forces within electrode field cages [16] by Schnelle *et al*. The method forms the basis of the simulations performed in chapters 4 and 5, and is discussed more thoroughly in section 2.3.

2.2 Finite Element Analysis.

As described in the previous section, most models introduced a numerical approximation by discretising the solution space into a series of evaluated "nodes". The Finite Element Method is similar, but divides the solution space into "elements" across which Poisson's equation is approximated. The element approach has many advantages over the imposition of meshes, as described in the previous section. Here, the procedures which underly construction of a Finite Element model are described.

2.2.1 Local Elements and the Shape Function

Consider the electrode geometry shown in figure 2.1(a). We may partition it into a number of partitioned elements, such as the triangular elements shown in figure 2.1(b); the nodes of the elements are the points where we wish to evaluate the potential. The elements may follow any mathematically-definable shape, and here we will consider both triangular and square elements. Taking triangular elements first and examining a single element (the "local element", such as the shaded area in figure 2.1(b)), it is possible to approximate Poisson's equation (equation (2.1)) linearly across it using an equation in potential variable u:

$$u \approx U = \alpha_1 + \alpha_2 x + \alpha_3 y \tag{2.3}$$

As we would wish to examine the potential at all three nodes, we may apply this equation to all three nodes (locally numbered 1 to 3);

$$\begin{aligned} U_1 &= \alpha_1 + \alpha_2 x_1 + \alpha_3 y_1 \\ U_2 &= \alpha_1 + \alpha_2 x_2 + \alpha_3 y_2 \\ U_3 &= \alpha_1 + \alpha_2 x_3 + \alpha_3 y_3 \end{aligned} \tag{2.4}$$

This may be written in matrix form, ie

$$\begin{pmatrix} U_1 \\ U_2 \\ U_3 \end{pmatrix} = \begin{pmatrix} 1 & x_1 & y_1 \\ 1 & x_2 & y_2 \\ 1 & x_3 & y_3 \end{pmatrix} \begin{pmatrix} \alpha_1 \\ \alpha_2 \\ \alpha_3 \end{pmatrix} \tag{2.5}$$

(a)

Electrode 1

Electrode 2

(b)

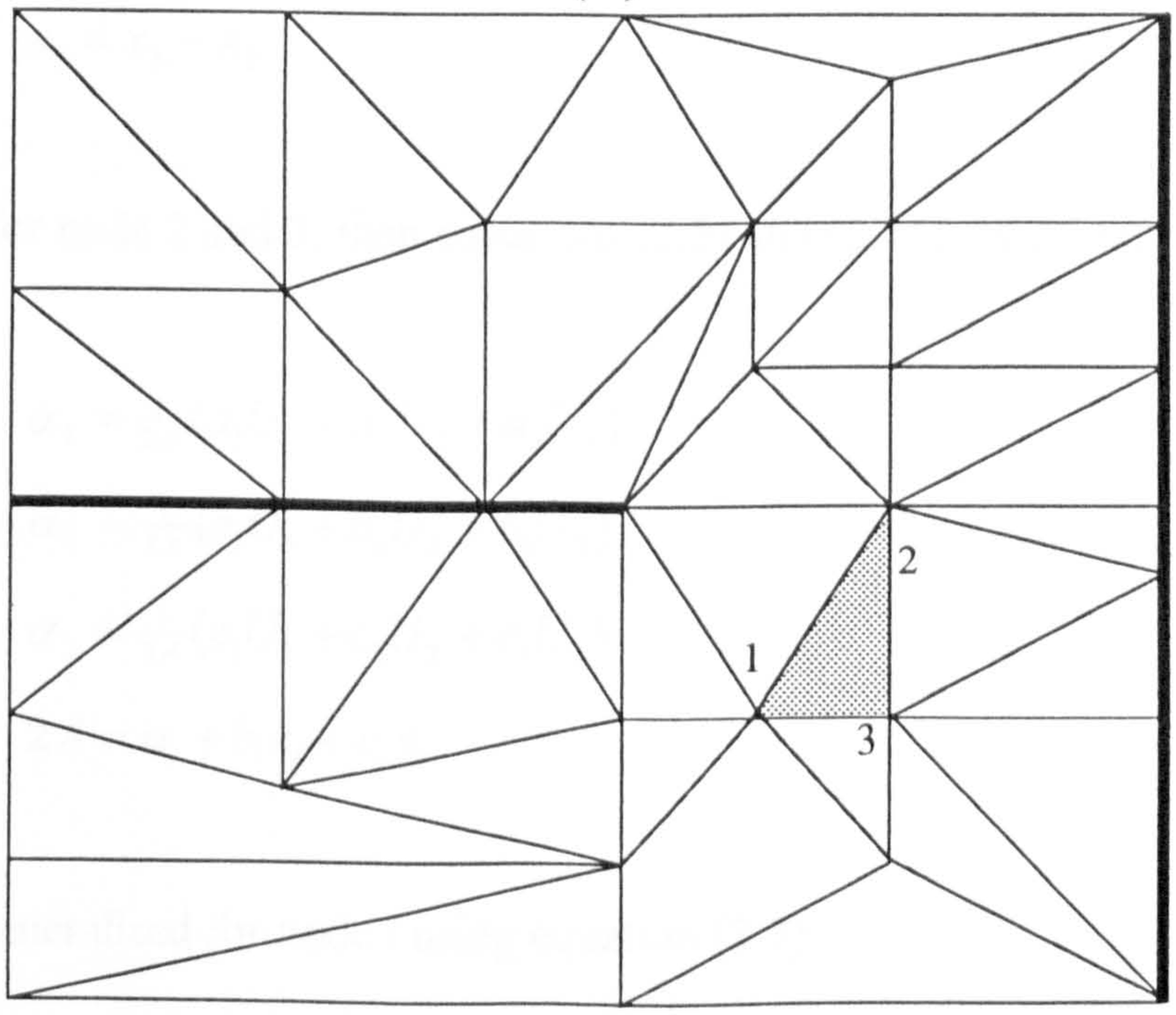

2.1 (a) A 2-electrode system, between which the electric field is unknown. (b) The solution space between the electrodes, discretised into a series of triangular elements. A single element is highlighed, with its nodes numbered.

Solving equation (2.5) in α we find

$$\alpha_1 = \frac{1}{2A}\begin{vmatrix} U_1 & x_1 & y_1 \\ U_2 & x_2 & y_2 \\ U_3 & x_3 & y_3 \end{vmatrix} \quad \alpha_2 = \frac{1}{2A}\begin{vmatrix} 1 & U_1 & y_1 \\ 1 & U_2 & y_2 \\ 1 & U_3 & y_3 \end{vmatrix} \quad \alpha_3 = \frac{1}{2A}\begin{vmatrix} 1 & x_1 & U_1 \\ 1 & x_2 & U_2 \\ 1 & x_3 & U_3 \end{vmatrix} \tag{2.6}$$

where A is the area of the triangle, and

$$2A = \begin{vmatrix} 1 & x_1 & y_1 \\ 1 & x_2 & y_2 \\ 1 & x_3 & y_3 \end{vmatrix} \tag{2.7}$$

If we define variables *a, b, c* such that for node 1

$$\begin{aligned} a_1 &= x_2 y_3 - y_2 x_3 \\ b_1 &= y_2 - y_3 \\ c_1 &= x_3 - x_2 \end{aligned} \tag{2.8}$$

and similarly for node 2 and 3, then equations (2.5) and (2.7) may be expessed as

$$\begin{aligned} \alpha_1 &= \tfrac{1}{2A}(a_1 U_1 + a_2 U_2 + a_3 U_3) \\ \alpha_2 &= \tfrac{1}{2A}(b_1 U_1 + b_2 U_2 + b_3 U_3) \\ \alpha_3 &= \tfrac{1}{2A}(c_1 U_1 + c_2 U_2 + c_3 U_3) \\ 2A &= a_i + b_i x_i + c_i y_i \end{aligned} \tag{2.9}$$

This may be generalised for node *i* using equation (2.3);

$$\begin{aligned} U &= \tfrac{1}{2A}\left[(a_1 + b_1 x + c_1 y)U_1 + (a_2 + b_2 x + c_2 y)U_{21} + (a_3 + b_3 x + c_3 y)U_3\right] \\ &= \sum N_i U_i \end{aligned} \tag{2.10}$$

where U_i is the potential at node i. N_i is the *shape function*, and for triangular elements, is written as:

$$N_i = \frac{a_i + b_i x_i + c_i}{2A} \tag{2.11}$$

which is a transformation into a coordinate system known as area coordinates [7], effectively normalising the dimensions of the element. This coordinate transformation is an important concept, and forms the basis for the examination of square elements, as discussed later.

2.3.2 The Galerkin Method

Let us suppose that across all the elements *i* the potential u is such that

$$\mathrm{u} = \sum_i N_i a_i \tag{2.12}$$

where a_i is a set of parameters, which will need to be determined. It is possible to insert this into equation 2.1, which may be expressed in the form:

$$\nabla . k \nabla u + Q = 0 \tag{2.13}$$

Substituting equation (2.12) into equation (2.13), we obtain the expression

$$R = \left(\nabla . k \nabla \sum_i N_i a_i + Q \right) = 0 \tag{2.14}$$

where R=0 for an exact solution of equation (2.12), and is otherwise an indication of the error introduced do to the linear approximation used in section 2.2.1. It is possible to force R to zero over the solution space Ω by satisfying the equation

$$\int_\Omega w_i \mathrm{R} d\Omega = 0 \tag{2.15}$$

where w is a set of *weighting functions*. In order to determine Poisson's equation over the solution space, we substitute equation (2.14) (Poisson's equation across a single element) into equation (2.15). Considering the effect of a the potential function across a single element U on a single node j, this result is given by

$$\int_{\Omega} w_j [\nabla . k \nabla U + Q] d\Omega = 0 \tag{2.16}$$

If we expand this to consider the effect for all nodes, we find

$$\int_{\Omega} w_j [\nabla . k \nabla U + Q] d\Omega = \sum_{e=1}^{n} \int_{\Omega_e} w_j [\nabla . k \nabla U + Q] d\Omega_e = 0 \tag{2.17}$$

Effectively, the integral across the solution space Ω has been replaced by the sum of the integrals across the elements Ω_i. If we integrate equation (2.17) by parts we obtain the following expression:

$$\int_{\Omega} w_j [\nabla . k \nabla U + Q] d\Omega = -\int_{\Omega} \nabla w_j k \nabla U d\Omega + \int_{\Omega} w_j Q d\Omega + \int_{\Gamma} w_j k \frac{\partial U}{\partial n} d\Gamma = 0 \tag{2.18}$$

where Γ is the surface surrounding the solution space Ω. The weighting functions w may take a wide range of values. In the Galerkin approach, we define the weighting functions as being the shape functions of the elements over which the integration is taking place; hence

$$\mathrm{R}_i^{(e)} = \left[\int \nabla N_i . k \nabla N_j d\Omega_e\right] U_j + \int_{\Omega} N_i Q d\Omega_e \tag{2.19}$$

where $\mathrm{R}_i^{(e)}$ is the residue at node i due to element e. This can be expressed in the form

$$\mathrm{R}_i^{(e)} = k_{ij}^{(e)} u_j + f_i^{(e)} \tag{2.20}$$

where

$$k_{ij}^{(e)} = \int_{\Omega_e} k\left(\frac{\partial N_i}{\partial x}\frac{\partial N_j}{\partial x} + \frac{\partial N_i}{\partial y}\frac{\partial N_j}{\partial y}\right) d\Omega_e$$
$$f_i^{(e)} = \int_{\Omega_e} N_i Q d\Omega_e \qquad (2.21)$$

These integrals are easily performed over the triangular shape functions described earlier:

$$\int_{\Omega_e} N_1^a N_2^b N_3^c d\Omega_e = 2A\frac{a!b!c!}{(a+b+c+2)!} \qquad (2.22)$$

where

$$k_{ij}^{(e)} = \int_{\Omega_e} \frac{k(b_i b_j + c_i c_j)}{4A^2} d\Omega_e = \frac{k(b_i b_j + c_i c_j)}{4A} \qquad (2.23)$$

$$f_i^{(e)} = \int_{\Omega_e} \frac{(a_i + b_i x + c_i y)}{2A} Q d\Omega_e = \frac{A}{3}Q$$

These results may be organised into the matrix form of equation (2.20); the local system matrices for a single element are:

$$\begin{bmatrix} R_1 \\ R_2 \\ R_3 \end{bmatrix} = \frac{k}{4A}\begin{bmatrix} b_1^2 + c_1^2 & b_1 b_2 + c_1 c_2 & b_1 b_3 + c_1 c_3 \\ & b_2^2 + c_2^2 & b_2 b_3 + c_2 c_3 \\ sym. & & b_3^2 + c_3^2 \end{bmatrix}\begin{bmatrix} u_1 \\ u_2 \\ u_3 \end{bmatrix} + \frac{A}{3}Q\begin{bmatrix} 1 \\ 1 \\ 1 \end{bmatrix} \qquad (2.24)$$

2.2.3 Quadrilateral Elements

The principles described above may be applied to elements of other shapes. If we consider quadrilateral elements rather than triangular elements, the linear approximation across the element is now an equation in four, rather than three, unknowns;

$$u \approx U = \alpha_1 + \alpha_2 x + \alpha_3 y + \alpha_4 xy \tag{2.25}$$

This can be shown [9] to transform to a shape function N_i where

$$N_i = \tfrac{1}{4}(1+\xi_i\xi_0)(1+\eta_i\eta_0) \tag{2.26}$$

where ξ_0 and η_0 may take the values ± 1 according to how the the shape function has been mapped onto the local element. By considering ξ and η as axes, this mapping process can be seen as a transformation of the element onto a master element, as shown in figure 2.2. The conformal mapping of one shape to another varies the lengths of the edges by a factor defined by the Jacobian of the transformation [17];

$$|J| = \begin{vmatrix} \frac{\partial x}{\partial \xi} & \frac{\partial x}{\partial \eta} \\ \frac{\partial y}{\partial \xi} & \frac{\partial y}{\partial \eta} \end{vmatrix} \tag{2.27}$$

From which we obtain the following relationships;

$$\frac{\partial \xi}{\partial x} = \frac{1}{|J|}\frac{\partial y}{\partial \eta} \qquad \frac{\partial \xi}{\partial y} = \frac{-1}{|J|}\frac{\partial x}{\partial \eta}$$

$$\frac{\partial \eta}{\partial x} = \frac{-1}{|J|}\frac{\partial y}{\partial \xi} \qquad \frac{\partial \eta}{\partial y} = \frac{1}{|J|}\frac{\partial x}{\partial \xi} \tag{2.28}$$

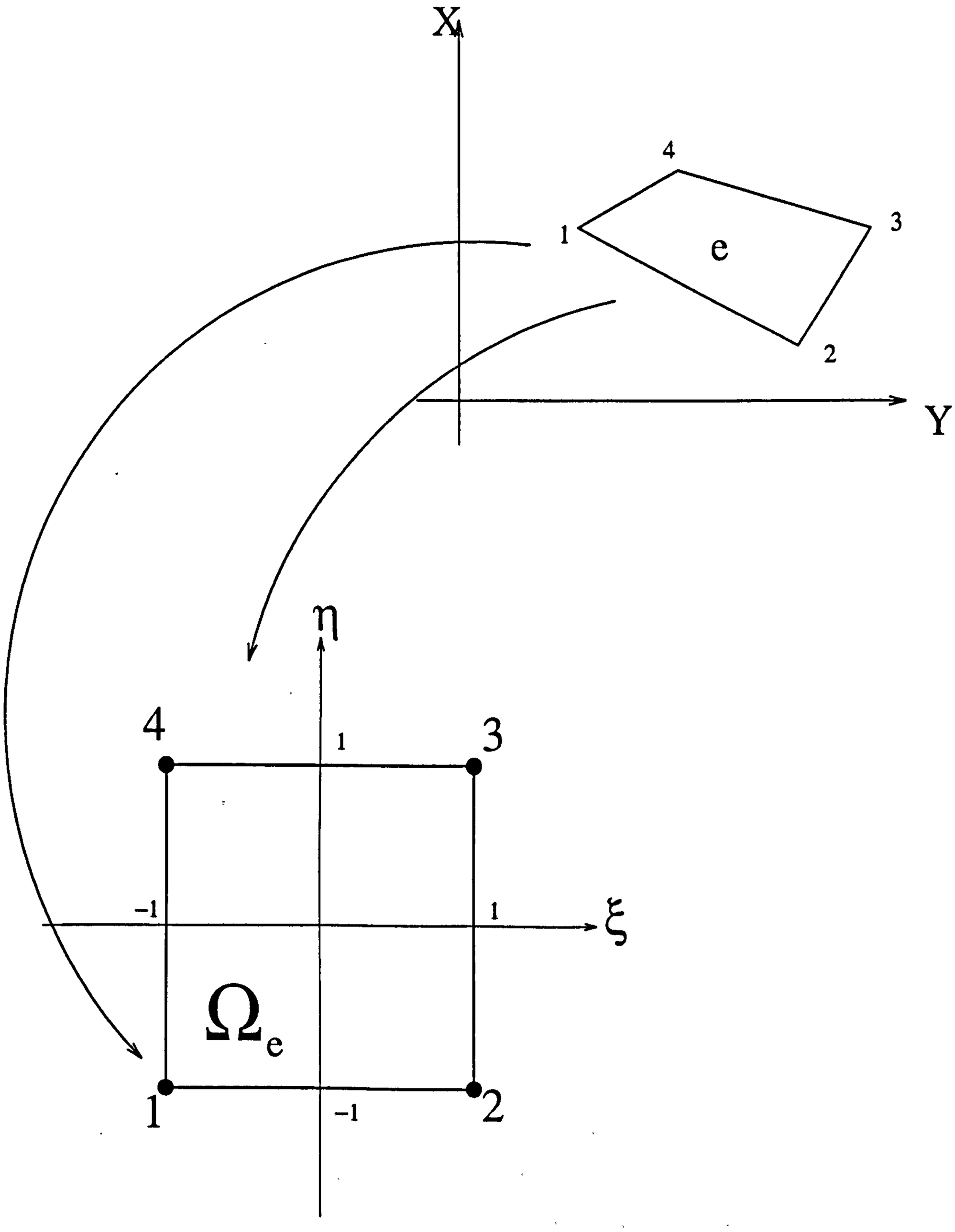

2.2 A quadrilateral element e is mapped onto a master element Ω_e

Here we define the master element, to which the element is transformed, as follows:

$$x = \sum x_i U_i(\xi,\eta) \qquad y = \sum y_i U_i(\xi,\eta) \tag{2.29}$$

We require these expressions to map out the potential U across the master element. This is expressed in terms of the potential function across the master element $U_i^{(e)}$;

$$U_i = U_i^{(e)}\big(\xi(x,y),\eta(x,y)\big) \tag{2.30}$$

from which we find, using the chain rule,

$$\frac{\partial U_i}{\partial x} = \frac{\partial U_i^{(e)}}{\partial \xi}\frac{\partial \xi}{\partial x} + \frac{\partial U_i^{(e)}}{\partial \eta}\frac{\partial \eta}{\partial x} \qquad \frac{\partial U_i}{\partial y} = \frac{\partial U_i^{(e)}}{\partial \xi}\frac{\partial \xi}{\partial y} + \frac{\partial U_i^{(e)}}{\partial \eta}\frac{\partial \eta}{\partial y} \tag{2.31}$$

Substituting equation (2.29) into equation (2.31) we obtain the following result:

$$\frac{\partial U_i}{\partial x} = \frac{1}{|J|}\left[\frac{\partial U_i^{(e)}}{\partial \xi}\sum_j y_j \frac{\partial U_j^{(e)}}{\partial \eta} - \frac{\partial U_i^{(e)}}{\partial \eta}\sum_j y_j \frac{\partial U_j^{(e)}}{\partial \xi}\right]$$

$$\frac{\partial U_i}{\partial y} = \frac{1}{|J|}\left[-\frac{\partial U_i^{(e)}}{\partial \xi}\sum_j x_j \frac{\partial U_j^{(e)}}{\partial \eta} + \frac{\partial U_i^{(e)}}{\partial \eta}\sum_j x_j \frac{\partial U_j^{(e)}}{\partial \xi}\right] \tag{2.32}$$

We now have an expression for the potential U across the original element expressed entirely in terms of the master element dimensions. We wish to determine the potential across the element according to Poisson's equation, so from equation (2.20) we need to solve for k and f. Since this is a highly complex integral, it is appropriate to approximate a solution using the Gaussian Quadrature principle [9], where the integral of a function g across a square area may be determined by summing the value of the function at four specific points. Across the master element, this is described by equation (2.33).

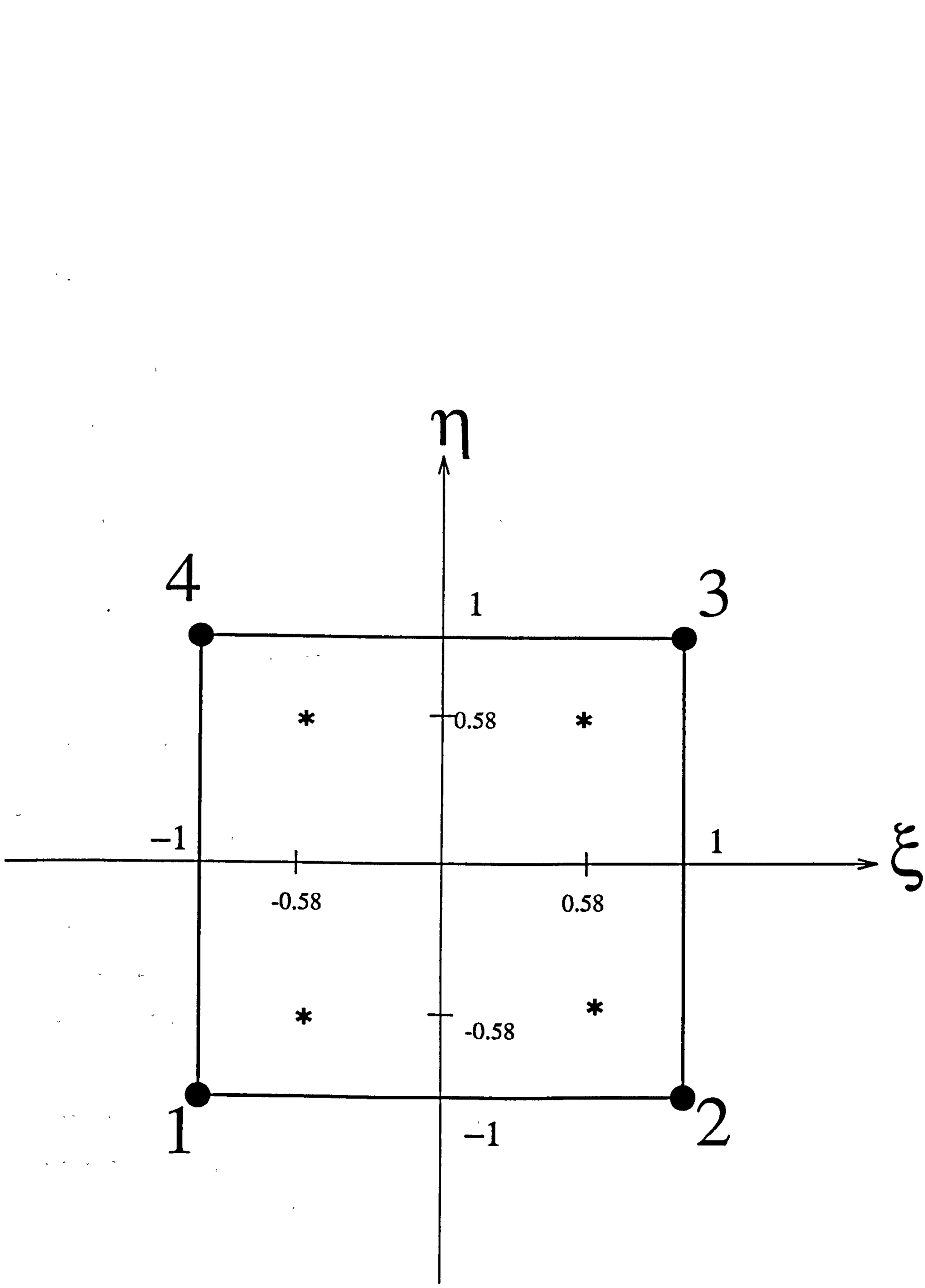

2.3 The location of Gaussian quadrature points across the quadrilateral master element.

$$\int g(\varsigma,\eta)d\xi d\eta = \sum_{1}^{n} g(\xi_l,\eta_l)w_l + E \tag{2.33}$$

where l is the set of co-ordinates shown in figure 2.3, E is the quadrature error (which equals zero if sufficient quadrature points are taken, as is the case here), n is the number of Gaussian quadrature points taken across the element and w is the set of weighting functions (equal to the shape function of the element, as expressed in equation (2.26). The values of k_{ij} and f_i are determined using this approximation on the integrals described in equations (2.21), and are assembled into a local matrix as described in equation (2.24).

This principle may be extended to general element shapes, such as cuboids or other three dimensional elements, with the mimimum of difficulty. An example of a Finite Element program using cuboid elements is presented in Appendix I.

2.2.4 Assembling the Elements

We have formulated a means of approximating the potential across an element by mapping it to a master element. We now examine the method of assembling the elements in such a way as to determine the overall potential distribution across the whole solution space. This is performed by assembling the local matrices, of the form expressed in equation (2.24), into system-wide equivalent matrices. For example, consider the 2-element solution space shown in figure 2.4. From equation (2.24), the local system matrices are defined in terms of the nodes of the element. For element 1, the system is represented as follows:

$$\begin{bmatrix} R_1 \\ R_2 \\ R_4 \end{bmatrix} = \begin{bmatrix} k_{11} & k_{12} & k_{14} \\ & k_{22} & k_{24} \\ sym & & k_{44} \end{bmatrix} \begin{bmatrix} u_1 \\ u_2 \\ u_4 \end{bmatrix} + \begin{bmatrix} f_1 \\ f_2 \\ f_4 \end{bmatrix} \tag{2.34}$$

Similarly, we can construct the system matrices for element 2:

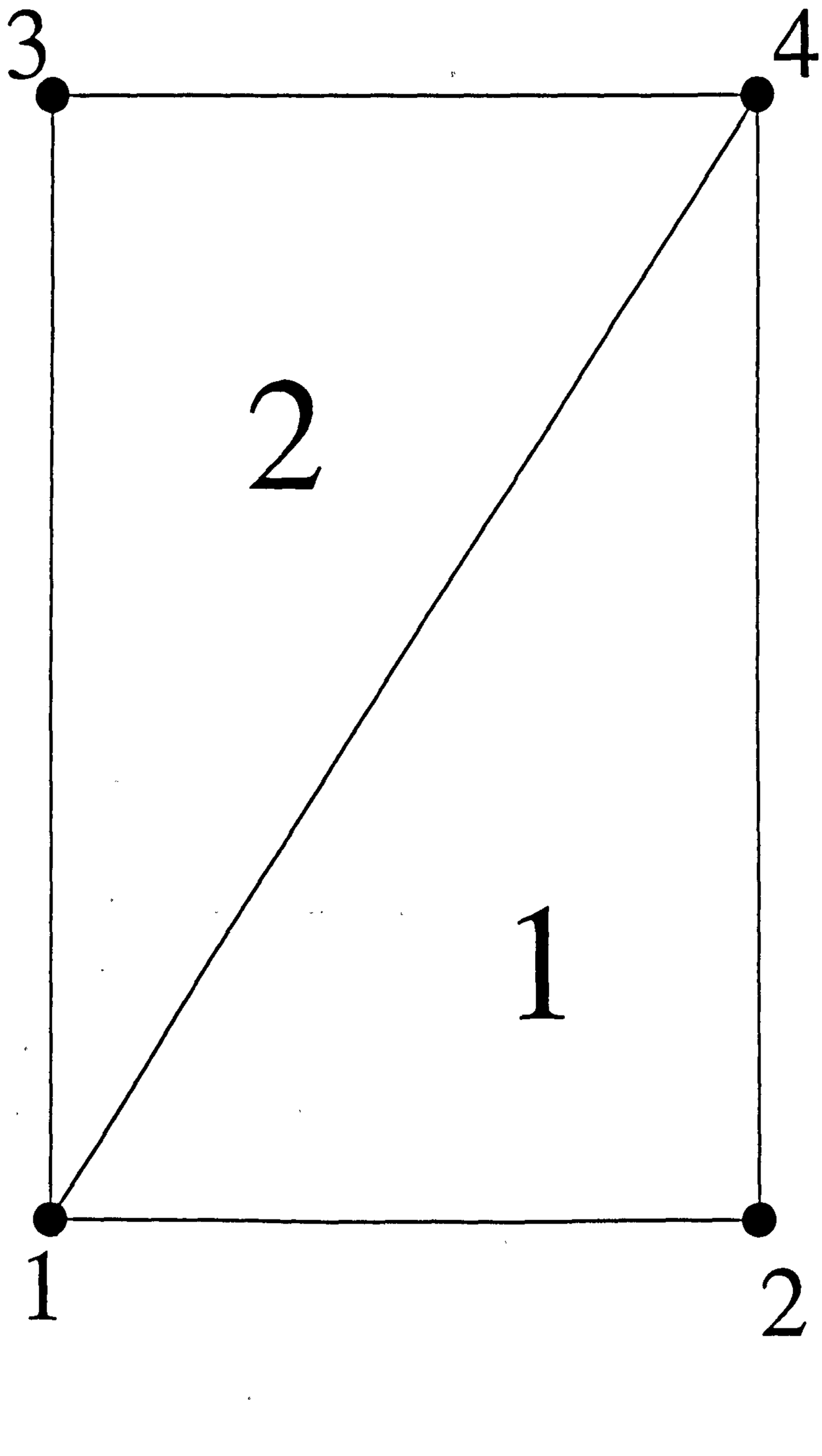

2.4 A rectangular solution space, discretised into 2 triangular elements

$$\begin{bmatrix} R_1 \\ R_4 \\ R_3 \end{bmatrix} = \begin{bmatrix} k_{11} & k_{14} & k_{13} \\ & k_{44} & k_{43} \\ sym & & k_{33} \end{bmatrix} \begin{bmatrix} u_1 \\ u_4 \\ u_3 \end{bmatrix} + \begin{bmatrix} f_1 \\ f_4 \\ f_3 \end{bmatrix} \tag{2.35}$$

The system matrices for the whole solution space is the result of merging both of the above according to nodal positions. The R term may be set to zero, as is the condition defined by the Galerkin method in equation (2.14). Hence:

$$\begin{bmatrix} k_{11}^{(1)} + k_{11}^{(2)} & k_{12}^{(1)} & k_{13}^{(2)} & k_{41}^{(1)} + k_{41}^{(2)} \\ k_{12}^{(1)} & k_{22}^{(1)} & 0 & k_{24}^{(1)} \\ k_{13}^{(2)} & 0 & k_{33}^{(2)} & k_{43}^{(2)} \\ k_{41}^{(1)} + k_{41}^{(2)} & k_{24}^{(1)} & k_{43}^{(2)} & k_{44}^{(1)} + k_{44}^{(2)} \end{bmatrix} \begin{bmatrix} u_1 \\ u_2 \\ u_3 \\ u_4 \end{bmatrix} = -\begin{bmatrix} f_1^{(1)} + f_1^{(2)} \\ f_2^{(1)} \\ f_3^{(2)} \\ f_4^{(1)} + f_4^{(2)} \end{bmatrix} \tag{2.36}$$

Note that $k_{23} = k_{32} = 0$. This is due to the arrangement of nodes such that no element contains both node 2 and node 3, and hence there is no interaction between these two nodes. Large numbers of nodes thus leads to potentially very sparse matrices, which may be exploited during the solution phase, as is described later.

2.2.5 Applying Boundary Conditions

Boundary conditions upon the system may take one of two forms: the Dirichlet Boundary condition where a potential at a given boundary (such as an electrode surface) and hence the potential at those nodes located on that surface, is defined; and the Neumann boundary condition which states that across the surface Γ that encloses solution space Ω, the following condition must apply:

$$\frac{\partial u}{\partial g} = \text{constant} \tag{2.37}$$

where g is an axis normal to the surface at the given point. This condition exists across the whole surface and need not be integrated into the procedure. Indeed, consideration of this condition is important, and such an imposition of symmetry of potential at the outer boundary may be exploited in simulating symmetrical systems.

Consideration must also be taken when simulating systems which involve changing phase relationships, as this symmetrical boundary will negate any phase relationships at the boundary.

However, it is necessary to define the known system potentials that comprise the Dirichlet boundaries. Having determined the system matrices, we now apply the initial conditions to the system. In the case of the solution of equation (2.1) these take the form of known node potentials. Consider the case of a 3-node system, as shown in equation (2.38).

$$\begin{bmatrix} k_{11} & k_{12} & k_{13} \\ k_{21} & k_{22} & k_{23} \\ k_{31} & k_{31} & k_{33} \end{bmatrix} \begin{bmatrix} u_1 \\ u_2 \\ u_3 \end{bmatrix} = \begin{bmatrix} f_1 \\ f_2 \\ f_3 \end{bmatrix} \tag{2.38}$$

If it is known that potential $u_3 = U_3$, then equation (2.38) may be rewritten as

$$\begin{bmatrix} k_{11} & k_{12} & 0 \\ k_{21} & k_{22} & 0 \\ 0 & 0 & 1 \end{bmatrix} \begin{bmatrix} u_1 \\ u_2 \\ u_3 \end{bmatrix} = \begin{bmatrix} f_1 - k_{13}U_3 \\ f_2 - k_{23}U_3 \\ U_3 \end{bmatrix} \tag{2.39}$$

In general, for the boundary condition of potential $u_i = U_i$ where U_i is known, the following procedure is followed:

1. Subract $k_{ij}U_i$ from f_j, where j is the list of all nodes, excluding i;
2. Assign $k_{ii} = 1$;
3. Set all other values in row and column i to 0;
4. Set $f_i = U_i$

Note that for a large number of boundary conditions, matrix $\boldsymbol{k}$ becomes increasingly sparse due to procedure number 3. As mentioned previously, sparsity may be

exploited during the solution phase in minimising the quantity of memory required for storing the matrix during the solving process.

2.2.6 The Solution Process

The solution of the potentials is thus performed by solving the calculation (2.20) across solution space Ω, with the residue set to zero;

$$\boldsymbol{u} = \boldsymbol{k}^{-1} \boldsymbol{f} \tag{2.40}$$

This calculation produces a vector u containing the values of the potential at all nodes. There are a wide variety of well-documented methods for implementation of this function. In the calculations performed in section 2.4.2 using the program shown in Appendix I, an intrinsic FORTRAN NAG function has been used. However, alternative methods such as Gaussian Elimination [17] or Incomplete Choleski-Conjugate Gradients [7] may be employed where solving routines are not available. The advantages of these methods are discussed elsewhere [7]. A consideration when performing such an implementation is that matrix $\boldsymbol{k}$ is largely sparse (ie contains a large quantity of zero-value elements) and is also symmetrical. It may be expedient to use a solution method such as ICCG which takes these features into account if computer storage space is at a premium.

Having determined the potentials across Ω, it is a relatively straightforward procedure to determine the electric field by calculating $\nabla \boldsymbol{u}$ across the nodes. This may be performed as a post-processing function, using mathematical tools such as MATLAB (The Math Works, Inc) or Mathematica (Wolfram Research) which are commercially available.

2.3 The Method of Moments

In contrast to the method described above, the Method of Moments (or Charge Density Method) does not discretise a finite solution space to derive the electric field across it. Instead the surfaces of the electrodes generating the electric fields are divided into a series of charges whose contributions to the electric field according to the principles of Coulomb described in equation 2.2. Thus the model derives its solution as an examination of unrelated points at which the potential is determined, rather than adopting the more abstact concept of a finite solution space. Consequently the model used is simpler to define.

2.4.1 Calculating Charge Density

Consider the system of n conducting electrodes shown in figure 2.5. Potentials V_n are applied, relative to 0V at infinity. Each electrode carries a surface charge q_n. It can be shown [19,20] that the charges and potentials are related by the equation:

$$\begin{aligned} V_1 &= p_{11}q_1 + p_{12}q_2 + \ldots\ldots\ldots + p_{1n}q_n \\ V_2 &= p_{21}q_1 + p_{22}q_2 + \ldots\ldots\ldots + p_{2n}q_n \\ V_3 &= p_{31}q_1 + p_{32}q_2 + \ldots\ldots\ldots + p_{3n}q_n \\ &\cdot \\ V_n &= p_{n1}q_1 + p_{n2}q_2 + \ldots\ldots\ldots + p_{nn}q_n \end{aligned} \tag{2.41}$$

where p_{ij} is a parameter which couples the potential on electrode i due to charge j. These expressions may be written in the form,

$$\begin{pmatrix} V_1 \\ V_2 \\ \\ V_n \end{pmatrix} = \begin{pmatrix} p_{11} & p_{12} & & p_{1n} \\ p_{21} & p_{22} & & p_{2n} \\ & & & \\ p_{n1} & p_{n2} & & p_{nn} \end{pmatrix} \begin{pmatrix} q_1 \\ q_2 \\ \\ q_n \end{pmatrix} \tag{2.42}$$

and hence:

$$\mathbf{V} = \mathbf{PQ} \tag{2.43}$$

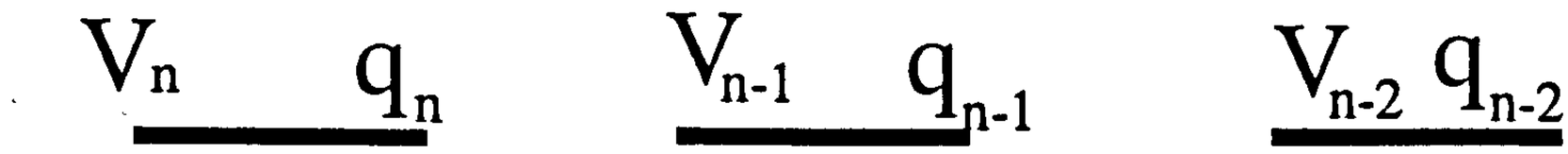

2.5 A sequence of *n* electrodes in space, each carrying a charge q and at potential V relative to 0V at infinity.

It is possible to simulate electrode systems by representing each electrode as a single point charge [16]. However, the more complex and detailed simulations presented here require that the physical dimensions of the electrodes be represented in the model, and that the charge density varies across the surface of the electrodes. In order to account for this charge distribution, an approximation is made here. By dividing the surfaces of the electrodes into subelectrode areas, the charge distribution across the subarea may be considered to be uniform. This approximation becomes more accurate as the number of subareas is increased [21]. Owing to the computer facilities available, the models used in this work were limited to a total of 2000 subareas.

Element p_{ij} of matrix **P** is the the potential on electrode *i* resulting from a unit charge on electrode *j* in the absence of any other charges. If subarea *j* is sufficiently small, then the potential at a point (chosen as the midpoint of subarea *i*) is determined by integrating over subarea dA_j a distance r_{ij} from such a unit charge thus:

$$p_{ij} = \frac{1}{4\pi\varepsilon_0\varepsilon_m}\int\frac{\sigma_j|dA_j|}{|r_{ij}|} \tag{2.44}$$

where ε_m is the relative permittivity of the medium surrounding the electrodes, which is assumed to be homogeneous. Since subarea *j* holds unit charge,

$$\sigma_j = \frac{1}{A_j} \tag{2.45}$$

From equations (2.44) and (2.45) we obtain an integration over electrode *j*:

$$A_j p_{ij} = \frac{1}{4\pi\varepsilon_0\varepsilon_m}\int\frac{|dA_j|}{|r_{ij}|} \tag{2.46}$$

If we assume that subarea *j* is rectangular and is in relation to the midpoint of electrode *I* in the axes imposed as shown in figure 2.6 then, provided the rectangle *j* does not cross the x or y axes the result of the above integration is given by [see appendix 6.1, 19]:

$$4\pi\varepsilon_0\varepsilon_m A_j p_{ij} = \left| I(x_2, y_2., z_1) - I(x_2, y_1, z_1) - I(x_1, y_2, z_1) + I(x_1, y_1, z_1) \right| \qquad (2.47)$$

where

$$I = x.\sinh^{-1}\left\{\frac{y}{\sqrt{(x^2+z^2)}}\right\} + y.\sinh^{-1}\left\{\frac{x}{\sqrt{(y^2+z^2)}}\right\} + z.\tan^{-1}\left\{\frac{z}{xy}\sqrt{(x^2+y^2+z^2)}\right\} \qquad (2.48)$$

This caneither be coded in this manner, or through the use of logarithmic identities [20,22]:

$$I = x\ln\left|\frac{y}{\sqrt{(x^2+z^2)}}\sqrt{1+\frac{y^2}{\sqrt{(x^2+z^2)}}}\right| + y\ln\left|\frac{x}{\sqrt{(y^2+z^2)}}\sqrt{1+\frac{x^2}{\sqrt{(y^2+z^2)}}}\right| + z.\tan^{-1}\left\{\frac{z}{xy}\sqrt{(x^2+y^2+z^2)}\right\} \qquad (2.49)$$

If the rectangle j lies across aither the x or y axes, it must be divided into two (or four) separate subareas partitioned by the axes, and calculated as before.

Having determined the values of matrix **P** it is possible to calculate the charges on each subarea by reorganising equation (2.43) and solving for charge **Q**:

$$\mathbf{Q} = \mathbf{P}^{-1}\mathbf{V} \qquad (2.50)$$

where V is the potential applied to the subareas. Alternatively, by considering the relationship described by equation (2.45), we may express equation (2.50) in terms of charge density, rather than charge:

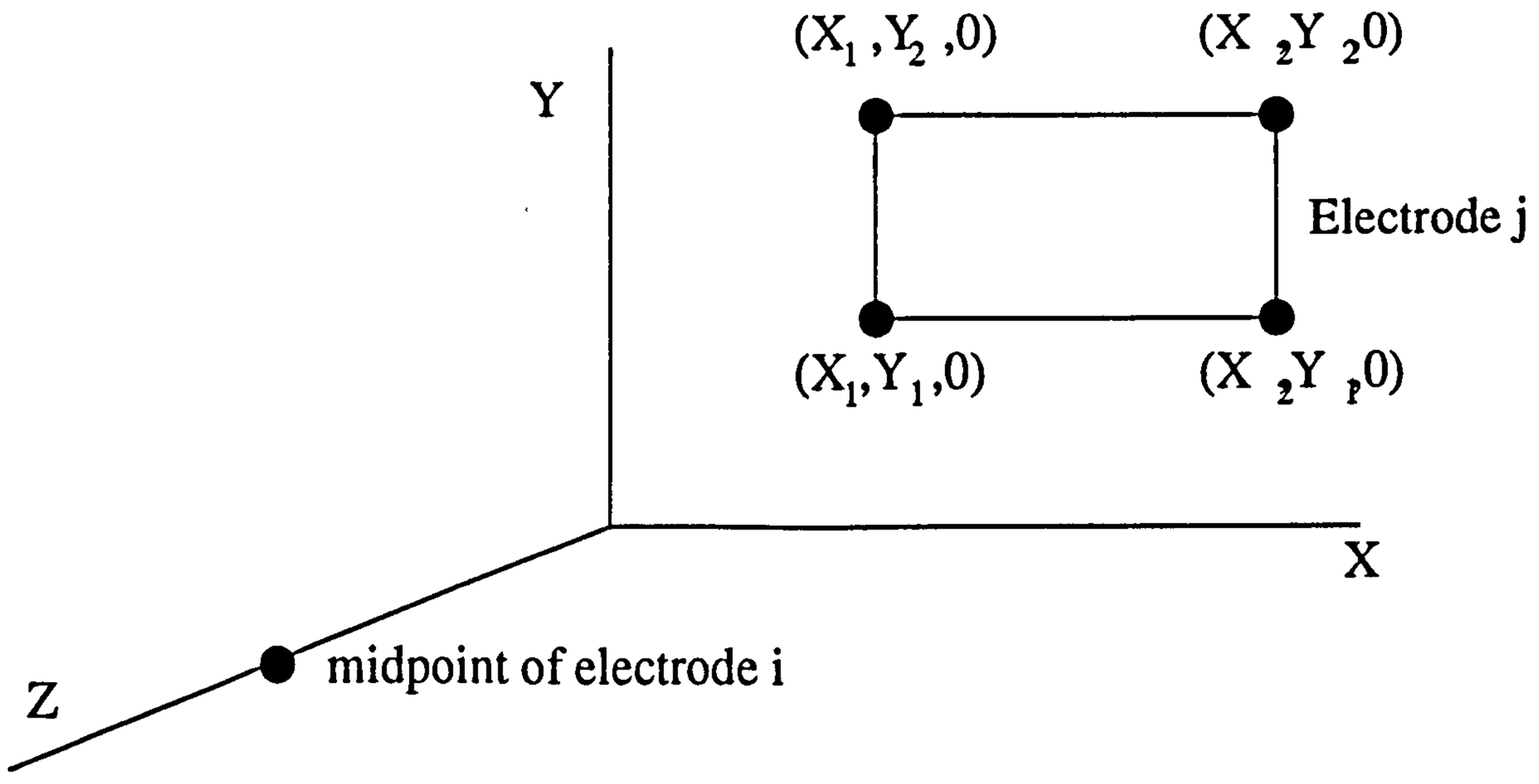

2.6 A coordinate system (X,Y,Z) imposed between the midpoint of electrode i(0,0,Z) and electrode j in the X-Y plane.

$$\sigma = \mathbf{P'}^{-1}\mathbf{V} \tag{2.51}$$

where σ is the charge density vector and $p'_{ij} = A_j p_{ij}$, as calculated using equations (2.47)-(2.49). The solution of equation (2.51) may performed using one of the methods described in section 2.2.5. In the sample program shown in Appendix II, used for the simulation example in section 2.3.2 and the studies in Chapters 4 and 5, the NAG library routine was employed.

Having derived the charge-density distribution across the electrode surfaces, it may be saved for future use. Any subsequent calculations involving a previously simulated electrode array may re-use an existing charge matrix for calculating the potential and electric field.

2.3.2 Calculating the Potential

If we consider an electrode array which has been subdivided into a system of charges across the electrode surfaces, there are a number of methods which may be employed for determining the potential due to these charges. One possible method is to apply Coulomb's law (equation (2.2)) and derive the electric field directly by calculation of the contributions of each charge to the electric field. However, this method may be inefficient to implement directly due to the requirement to consider vector computations.

An alternative approach is to consider the expression given in equation (2.51), which states that for a given set of points in space the potential ϕ is dependent on the charge density across the subareas of the electrode, and on a charge-potential relationship matrix:

$$\phi = \sigma \mathbf{P'} \tag{2.52}$$

If this is expressed in the form of equation (2.44), we can express the relationship of the potential at a point to charge n a distance s away at its centre in the following form

$$p_n' = \frac{1}{4\pi\varepsilon}\int \frac{|dA_n|}{|s_n|} \tag{2.53}$$

Substituting equation (2.53) into expression (2.52), we can derive an expression for the potential at a general point *k*:

$$\phi_k = \sum_{n=1}^{N} \sigma_n \int \frac{|dA_n|}{|s_n|} \tag{2.52}$$

where N is the total number of subareas and s_n is the distance from the centre of subarea n to the point k. The advantage of this implementation is that the code required to perform equation (2.51) is the same as that required for equation (2.46), allowing both to be performed by the same subroutine. This program is implemented in such a way as to provide the results in the form of 2D matrices at locations **K** which may then be loaded into a mathematical post processing system such as Matlab. Furthermore it is a straightforward task to adapt the calculation of the potential so as to calculate potentials at points displaced a small, regular distance from the points of study along the axes centred on the sample point. This allows calculation of the electric field at the series of points, by calculating field gradients based on differences between potentials at these extra points. Such a method increases computation time, but gives high levels of accuracy by minimising the distance from sample point to extra nodes. Having calculated the electric field in vector form in this manner, the data may be saved in the form of matrices $\mathbf{E}x_K$, $\mathbf{E}y_K$ and $\mathbf{E}z_K$.

Since the electrode model in the Method of Moments requires a fixed charge density, it is unable to perform true AC analysis. However, by discretising the AC cycle into a number of static "frames" it is possible to analyse phase effects across a cycle in great depth.

2.4 A Comparison of the Finite Element and Moment Methods

In the previous sections two numerical models have been discussed, having been determined to be most applicable to the numerical solution of electric fields in the studies discussed later in this thesis. Here the applicability of these methods for various applications of AC electrokinetic study are analysed.

2.4.1 Approximations and Limitations

It is the nature of all numerical models that the solution provided is an approximation to the actual field, rather than an exact solution. By introducting simplifying conditions, such as discretisation of otherwise continuous functions, errors are introduced into the solution, with which care must be taken to minimise. An understanding of the approximations made in a model, the limitations placed on the construction of that model, and the restrictions on determining the solution are useful in determining which method is appropriate for a given problem.

The Finite Element model divides the volume containing both the electrodes and the volume for which a solution is required into elements which are solved in a piecewise linear fashion. The inclusion of the solution points as part of the model restricts the number of locations that can be examined, in that the model must retain the regular order of elements throughout. Furthermore, without the aid of powerful graphical tools the constuction of the model itself (in terms of the positioning of nodes and the allocation of potential boundary conditions to these nodes) is a non-intuitive and laborious task when the number of elements is reasonably large. This makes modification of the model difficult and error-prone.

A further consideration is the Neumann boundary condition (see section 2.2.5) which effectively creates "ghost" electrodes in the mirror-image of the electrodes being simulated, reflected at the outer boundary of the solution space in all directions. This has the effect of raising the magnitude of the potential at the boundary and setting the electric field across it to zero, both of which create errors in the final solution. Further care must be taken where a phase direction is studied (such as the travelling-wave simulations of chapter 5), as the reflected electrodes at either end of the electrode array

will have applied travelling waves running counter to those on the actual electrode simulated. To avoid this, the electrodes and region of study should be isolated from the boundary by large, empty elements. These introduce a large "distance" between the real and ghost electrodes, but increase simulation time. Alternatively, it is sometimes possible to make use of symmetry in the electrode geometries by placing the Neumann boundary at the time of symmetry and only simulating half of the problem space.

The Method of Moments does not employ the concept of a defined solution space, and thus does not restrict the choice of sample points to be examined, or create "ghost" electrodes. However, the system of discretisation of the electrodes creates approximation errors of a different nature. The system of expressing the charge on a subarea as a single point from which the distance to the sampling point creates errors in close proximity to the electrode surfaces, where the difference between charge focussed at set points, rather than distributed equally across the subarea surfaces, becomes more apparent. Thus, within a distance from the electrodes approximately equal to the width of adjacent subareas, the potential will vary according to whether it is facing a point charge or a subarea boundary.

Another limitation to the Moments Method is that due to the nature of the model considering a direct-line relationship between the sample point and the point charges, the introduction of heterogeneous dielectric media between these points (or into the model generally) is a complex problem which potentially increases computation time to make the method unsuitable for any problems of this nature. Thus this method is most appropriate to the simulation of electrodes suspended in a medium such as the aqueous soultion of basic electrokinteic experiments.

2.4.2 Computational Intensity

In order to highlight the advantages and disadvantages of using the two simulation methods descibed above, a simulation of the electric field generated by a set of travelling-wave electrodes (see chapter 5) was simulated using both methods. The

programs used are shown in appendices I and II. Presented here are the results of that comparison.

Both simulation programs were written using FORTRAN 77 and implemented on a Cray Y-MP supercomputer. The Cray was chosen due to the large nature of the matrices involved in the calculation, which are beyond the resources of most medium-size mainframe computers. The Moments model consisted of nine opposing pairs of electrodes across a channel. The electrodes were each divided into 110 subareas, giving a total of approximately 2000 subareas. The output was in the form of four 2D matrices containing potential and electric field data. The Finite Element model contained only 7 electrodes, and made use of the Neumann boundary of symmetry across the centre of the channel. The simulation space was divided into approximately 5500 cuboid elements 2.5μm square across the X-Y face, and of varying thickness. Half-width electrodes were added at either end of the array to preserve charge neutrality.

Compared to the resources a modern computer can provide, the disk requirements of the two programs are small. Counting both the calculation programs and their respective data generators, neither set of programs exceeded 16kb. The input files differ more significantly, with the Moments datafile requiring only 157kb compared to the 886kb Finite Element datafile. At output the total memory required is once more similar, with the Moments data requiring 1.2Mb against the Finite Element data requiring 1.6Mb. It is important to consider that these data files do not represent data in the same manner, as is discussed below.

The quantity of memory required by both systems is effectively proportional to the largest matrix used in the calculations. In Finite Element Analysis, this is the System Matrix which is proportional to the square of the number of nodes. For the Method of Moments it is the Charge Relationship matrix, which is proportional to the square of the number of subareas. Since the Cray operates at 64-bit (single) precision, the quantity of swap space required for the Finite Element and Moment methods is 230Mb and 30Mb respectively. The Finite Element matrix is by its nature sparse (with sparsity

reaching 90% in some cases), and it is possible to reduce the swap space required by the system by performing the calculations using only the non-zero matrix elements. This increases the efficiency of the program, although there is a trade-off in the form of an extended total run-time.

Although the Moments method performs the better of the two when compared on the basis of maximum memory required, this situation is not reflected in the total CPU time required to run these programs. Using the Cray YMP, the Finite Element method took only 349.9 seconds to run compared with the Moment Method's 1881.3 seconds. When the time-memory integrals (a standard measure of the resources used by a program) are compared, the Finite Element program usage was approximately half that of the Moments program (10442.7Mword-seconds compared to 22370.7Mword-seconds). This is due to the the methods by which the main matrices are populated, and by the method of extracting the solution from that matrix. The Finite Element system matrix is assembled by calculating only those matrix elements which represent coupled nodes, an increasingly small quantity as the number of elements increases. Once constructed, the matrix is solved and the solution is derived directly. However, the smaller Moments matrix is fully populated, as every charge is effectively coupled to every other charge. Thus, the matrix takes considerably longer to construct. Furthermore, the solution is calculated by performing mathematical operations based on the value of every charge density to provide the solution for a single point in space. For large numbers of sample points, determining the solution can thus become a large part of the calculation process.

The efficiency of Finite Element Analysis simulations may be further enhanced if solution routines are used which take advantage of the unusual properties of the system matrix - those of sparsity and symmetry - which may drastically reduce the memory capacity required to perform the calculation. Another method of improving the performance of Finite Element models is to concentrate the elements in those locations where the electric field changes rapidly, such as near electrode edges. Adaptive meshing such as this reduces the number of elements required to gain an accurate solution. However, as the mesh generation is a pseudo-random process, it

may complicate the process of determining the electric field around the electrodes. Furthermore, if not accurately controlled such meshing can make the analysis of specific points in a defined plane a complex procedure. Several software suites are commercially available such as Maxwell (Ansoft Inc.) which provide an integrated meshing / solution / postprocessing environment.

2.4.3 Comparing Simulation Results

As a basis for comparison of the methods, the time-averaged magnitude and phase distributions of the electric field through a plane 3μm above the electrodes were studied using both methods. This point of comparison was chosen for its simplicity and the ease with which differences in the simulations may be identified, as well as its importance to the study of travelling-wave dielectrophoresis (see Chapter 5). The magnitudes (parts a, c, e) and phases (parts b, d, f) of the X, Y and Z components are illustrated in figures 2.7 and 2.8 for the Finite Element and Moments methods respectively.

The significance of the results themselves are discussed in chapter 5. Here we examine only the *forms* of the results. As the electric field is unknown, it is difficult to determine which simulation is more "correct" than the other in the event of discrepancies occuring. Rather, the reasons for these discrepances occurring may be postulated in considering the differences in the models. used. Since the plane studied is above the electrodes and extra electrodes (beyond the regions studied) have been included, approximation errors of the types discussed in section 2.4.1 have been largely avoided. Hence the results presented here allow for the examination of other differences which may occur.

It is apparent by inspection that the results of the two simulations correlate very well both in terms of absolute values and field conformations. The comparisons of phase distribution are also highly favourable. The fact that the two methods produce highly similar results via two completely different methods, both of which agree with experimental predictions (as discussed in chapter 5), indicate that it is highly probable that both results are, in general, accurate.

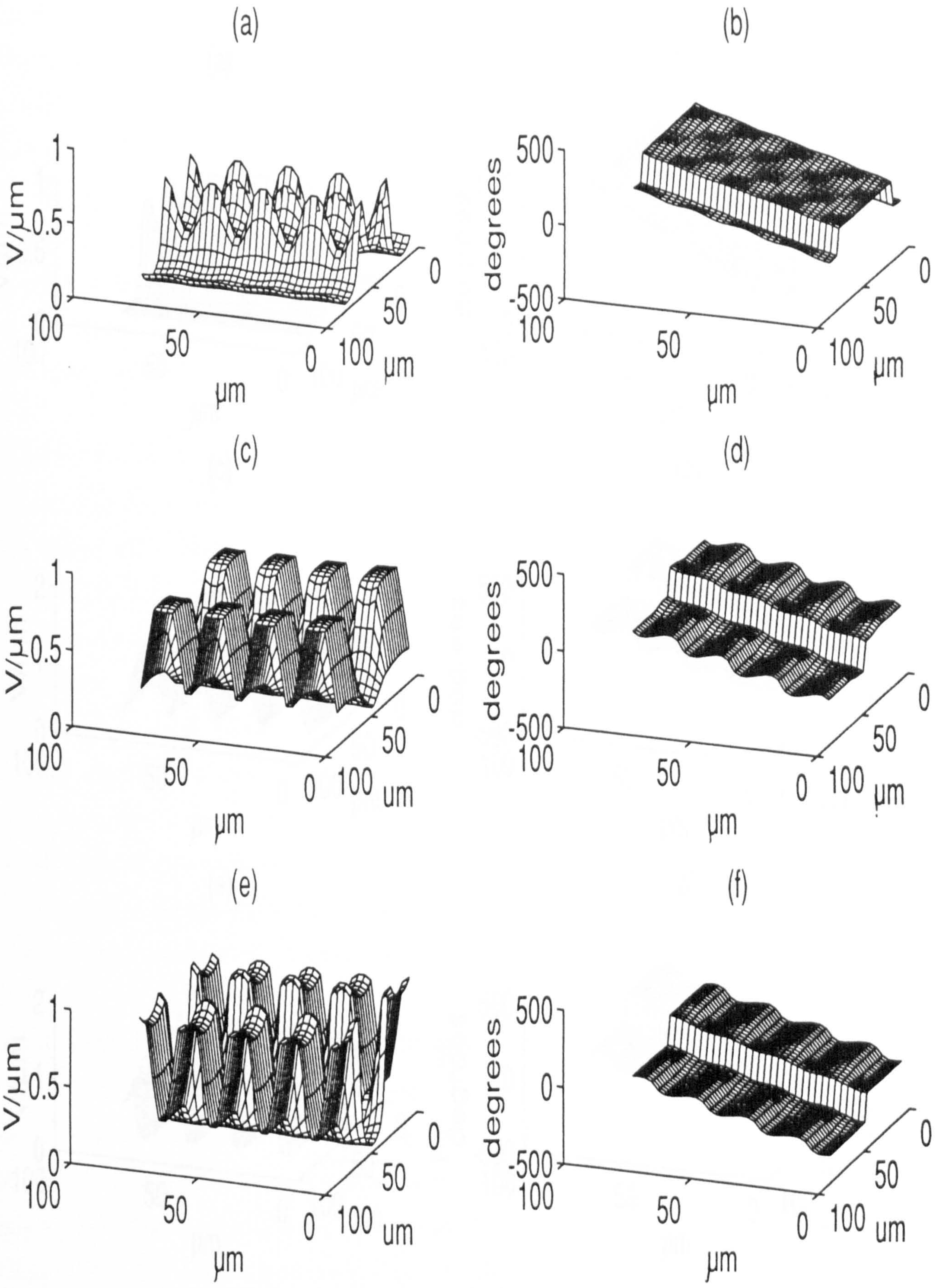

2.7 Time-averaged magnitudes (a, c, e) and phases (b, d, f) of the X, Y and Z components of the electric field components in a plane 3µm above a travelling-wave electrode array of the type described in chapter 5. The simulation was performed using the Moments method.

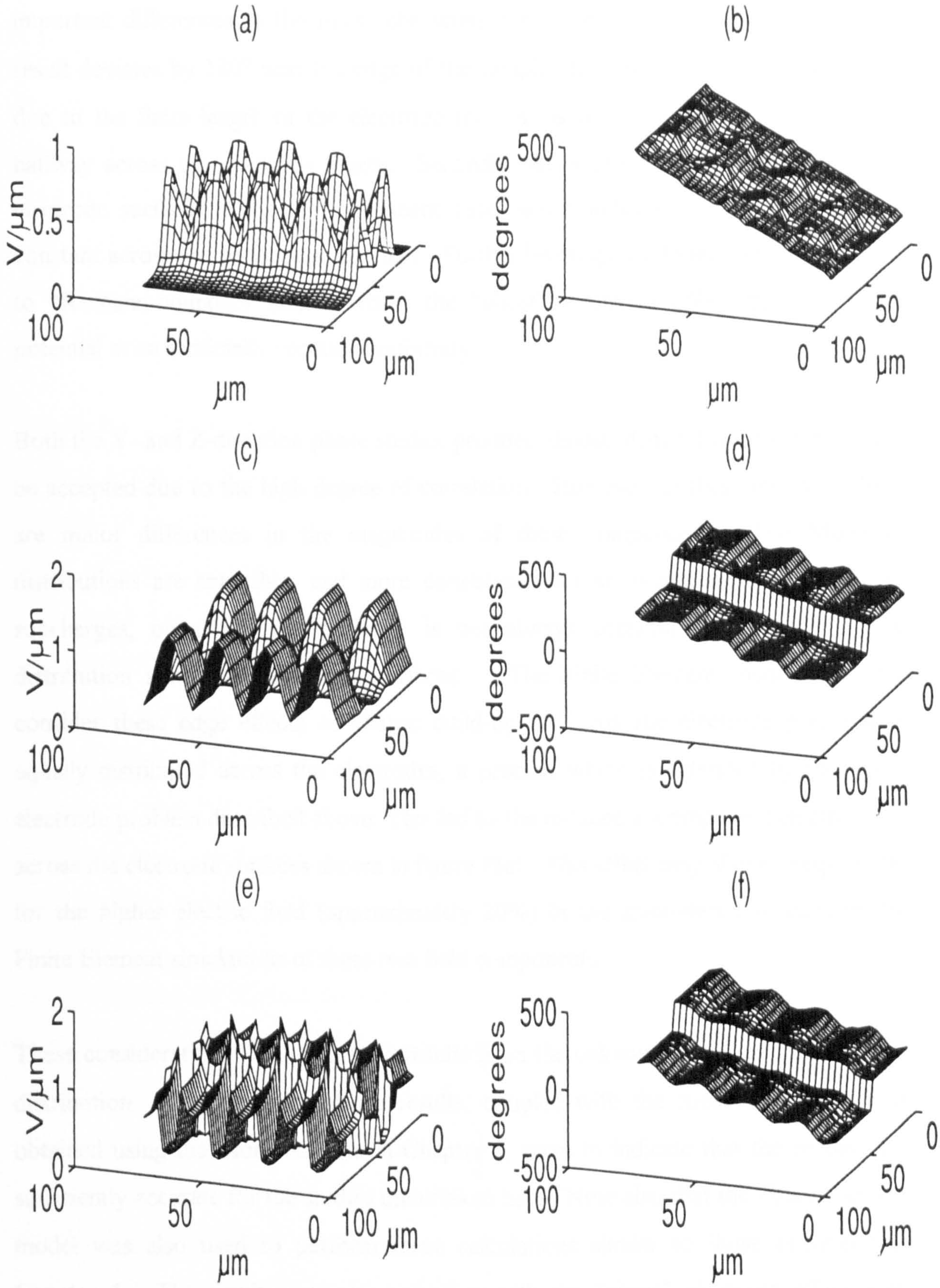

2.8 Time-averaged magnitudes (a, c, e) and phases (b, d, f) of the X, Y and Z components of the electric field components in a plane 3µm above a travelling-wave electrode array of the type described in chapter 5. The simulation was performed using the Finite Element method.

However, minor discrepancies do occur in the results. The correlation of X-direction magnitudes is excellent, with very little variation between them. However, two important differences in the phase characteristics are evident. Firstly the Moments result deviates by 180° near the edge of the sample area, over the electrodes. This is due to the finite length of the electrode models, as the changeover occurs exactly halfway across the electrode length. Secondly, the phase does not vary across the electrode surfaces in the Finite Element case, which indicates that the potential is constant across the surfaces at all times. Further investigation found this to be related to Neumann-boundary effects where the "ghost" electrode effect maintained the potential at an artificially constant uniformity.

Both the Y- and Z-direction phase studies produce almost identical results, which may be accepted due to the high degree of correlation. However, in these instances there are minor differences in the magnitudes of these components. The Moments distributions are smoother, and more consistent with an averaged-out field due to subcharges, on which the potential is not always constant due to the charge distribution across the electrode surfaces. The Finite Element model does not consider these edge effects of charge build-up and thus the electrode potential is equally distributed across the electrodes, a process which is extended by the ghost electrode problem described above. This led to the reduced Z-component electric field across the electrode surfaces shown in figure 8(e). This effect may also be responsible for the higher electric field (approximately 20%) in the inter-electrode gaps in the Finite Element simulations of these two field components.

These considerations thus distort the results from the unknown "correct" electric field distribution. The similarity of the results, coupled with the successful predictions obtained using the Moments data in Chapter 5, seem to indicate that the models are sufficiently accurate for the studies undertaken here. Note also that the Finite Element model was also used to perform force calculations similar to those presented in Chpater 5. The results were very similar, with the "ghost" electrode effect only

causing significant problems in studying Z-plane effects (see Chapter 5, particularly figure 5.5, for details).

2.5 Conclusions

In order to examine the effects of AC electrokinetics on particles, the electric field generated by manipulating electrodes must be analysed. For all but a few cases, the electric field must be simulated using an approximate numerical model. Five alternative schema for the numerical analysis of electric fields have been discussed, and the most appropriate methods for the simulation of electrodes for dielectrophoretic applications have been described in detail.

The Method of Moments divides the potential across the electrodes into subareas upon each of which the charge is determined. The contributions of each charge on the potential of an arbitrary point are subsequently determined. The method is slow and computationally intensive. The fact that the mesh of points is arbitrary, and has no dependence on the division of subelectrodes, is advantageous in the repeated simulation of a given geometry for a number of circumstances. Also, the grids may be collocated, allowing the points to be animated, for example. The simulation requires a large computing overhead, and is thus most suitably implemented on a mainframe system. Calculation of the electric field may be performed within the program by examining local potentials and deriving the gradients, which increases the processing time but offers accurate solutions.

The Finite Element Method partitions the solution space into elements across which the potential is calculated by approximation of Poisson's equation. It requires large computer resources unless specialised solving routines are employed. It is possible to reduce the total number of elements used in the calculation by generating a mesh which contains more elements (and thus resolves the potential in greater detail) in regions where the field gradients are high, and fewer elements where there is little change in electric field over a wide spatial area. Use of such routines allows more rapid simulation, and can be implemented on a well-specified PC. This generates a pseudo-

random set of nodes which may cause problems in matching the potential at an arbitrary point on two simulations, for example to examine the result of changing electrode phase. The method is thus best suited for non-phase related applications such as the study of dielectrophoresis.

2.6 References

[1] Pohl HA 1978 *Dielectrophoresis* (Cambridge: Cambridge University Press)

[2] Huang Y and Pethig R 1991 *J. Meas. Sci. Tech.* **2** 1142-1146

[3] Binns KJ and Laurenson PJ 1963 *Analysis and Computation of Electric and Magnetic Field Problems* (Oxford: Pergamon Press)

[4] Hölzel R 1988 *Med. & Biol. Eng. & Comp.* **26** 102-105

[5] Nath B 1974 *Fundamentals of Finite Elements for Engineers* (London: Athlone Press)

[6] Zienkiewicz OC and Taylor RL *The Finite Element Method, vol.1, 4th ed.* (London: McGraw-Hill)

[7] Binns KJ, Lawrenson PJ and Trowbridge CW 1992 *The Analytical and Numerical Solution of Electric and Magnetic Fields* (Chichester: Wiley)

[8] Gallagher RH, Zienkiewicz OC, Oden JT, Cecchi MM and Taylor C (eds)1978 *Finite Elements in Fluids* (Chichester: Wiley)

[9] Watkins LR 1985 *Electromagnetic Field Solutions via the Finite Element Method*, MSc dissertation, University of Cape Town

[10] Yu Q 1994 *Proc. 2nd int Conference on Computation in Electromagnetics*

[11] Dai W-W, Marsili PM, Martinez E and Morucci JP 1994 *Physiological Measurement* **15** 161-168

[12] Doering CR, Horsthemke W and Riordan J 1994 *Physical Review Letters* **72** 2984-2987

[13] Maxwell JC 1892 *A treatise on Electricity and Magnetism 3rd ed, vol. 1* (Oxford: Oxford University Press)

[14] Martinez G and Sancho M 1980 *IEE Proc.* **127** 531-534

[15] Pethig R, Huang Y, Wang X-B and Burt JPH 1992 *J. Phys. D: Appl. Phys.* **25** 881-888

[16] Schnelle T, Hagedorn R, Fuhr G, Fiedler S and Müller T 1993 *Biochim. Biophys. Acta* **1157** 127-140

[17] Kreyszig, E 1983 *Advanced Engineering Mathematics 5th ed.* (New York: Wiley)

[18] Prost J, Chauwin J-F, Peliti L and Ajdari A 1994 *Physical Review Letters* **72** 2652-2655

[19] Birtles AB, Mayo BJ and Bennett AW 1973 *Proc. IEE* **120** 213-220

[20] Wang X-B 1991 *Unpublished work*

[21] Reitan DK and Higgins TJ 1951 *J. Appl. Phys.* **33** 223-226

[22] Abramowitz M and Stegun IA 1965 *Handbook of Mathematical Functions* (New York: Dover Publications)

Chapter 3

"Motion Without Force": Analysis of Dielectrophoretic Ratchets

3.1 Introduction

Recent theoretical interest has developed in the study of induced motion in colloidal particles by harnessing thermally-induced motion via the application of assymetric periodic potentials [1-5]. Studies by Ajdari and Prost [1] considered the forces acting on a particle in suspension and subject to a Brownian motion. A sawtooth potential, when repeatedly applied and removed for finite periods of time, will theoretically show a biased overall motion in the direction along the direction in which potential increases for the longest physical distance, leading Chauwin *et al* to the assertion that this principle provided "mouvement sans force" [2]. Analysis by Magnasco [3] and subsequently by Astumian and Bier [4], illustrated that models of this nature could be devised to explain the motion of proteins along biopolymer using thermal noise to advance the smaller molecules though a series of potential "ratchets".

The application of this principle to larger particles, using dielectrophoresis to provide the necessary potential gradient, was first proposed by Ajdari and Prost [1] and subsequently demonstrated experimentally by Rousselet *et al* [5]. Rousselet and co-workers used latex spheres of varying diameters to attain particle motion of $0.2\mu m\,s^{-1}$, with diffusion rates of particles advancing from one ratchet to the next (at an "efficiency" of 40% per step) for significant times of zero applied field. However, the form of the boundary of attraction between two successive ratchet units was not determined, taking a shape somewhere between a straight line and a semicircle across the widest part of the structure. In the work presented here, the electrodes used by Rousselet *et al* are examined using computer modelling and the form of the crossover boundary is determined.

Ajdari and Prost [1] also proposed that this method has applications in the separation of particles according to their relative sizes. It is proposed here that, using the dielectrophoretic methods described here, it is possible to separate particles in a continuous manner according to their relative *dielectric* properties using principles establised in previous publications on the separation of viable and non-viable yeast cells [6]. It is shown that, under the correct conditions, it may be possible to drive particles of specific dielectric properties *backwards* through the ratchet system whilst other particles are simultaneously being driven *forwards* in the manner described previously.

This study also presents an analysis in the optimisation of the "Christmas-tree" electrode design [5] for the efficient transport of particles in manufactured ratchet systems. Since the efficiency of transportation depends on the percentage of particles stepping forward for each application of the field, a ratchet design will optimally have a negligible distance between potential peak and valley. A study in one dimension, along a line between the electrode tips, provides a means of making comparisons between electrode configurations and principles for optimisation. Furthermore, a system is proposed whereby the principle of ratcheting is retained, but the reliance of the system on Brownian motion to provide the local particle motion is eliminated. This greatly improves ratchet performance and efficiency.

3.2 Forced Thermal Ratchets

Consider a quantity of colloidal particles, of greater polarisability than the surrounding medium, suspended within the electrode geometry shown in figure 3.1, with successive electrode tips spaced a distance d apart. On application of a potential difference to the electrodes, the particles will undergo positive dielectrophoresis towards the region of highest electric field. For spherical particles of radius r, the dielectrophoretic force is calculated using the expression [7]:

$$F(\omega) = 2\pi\varepsilon_0\varepsilon_m r^3 \mathrm{Re}[f_{CM}]\nabla E^2 \tag{3.1}$$

where ε_0 is the permittivity of free space, ε_m is the relative permittivity of the medium, Re denotes that the real part of the function in brackets be taken, ∇ is the del vector operator, E is the RMS electric field, and f_{CM} is the Clausius-Mossotti factor defined by:

$$f_{CM} = \frac{\varepsilon_p^* - \varepsilon_m^*}{\varepsilon_p^* + 2\varepsilon_m^*} \tag{3.2}$$

where ε_p^* and ε_m^* are the complex permittivities of particle and medium respectively.

Due to the ∇E^2 term, dielectrophoretic motion will be directed along path of increasing local electric field gradient. Due to the assymetric design of the electrodes, the field gradient is biased such that a greater proportion of the space between successive electrode tips generates dielectrophoretic motion to the right of the diagram than to the left (figure 3.2). Hence the majority of particles will translate towards the right.

Following the collection of particles over a period τ_{ON}, the potential difference across the electrodes is removed. Under Brownian motion, the particles will then drift from the electrode tips over a period of time. After sufficient time, some particles will drift a distance d_1 which will place those translating to the right within the dielectrophoretic capture region of the next (right) electrode, after which point the electric field is

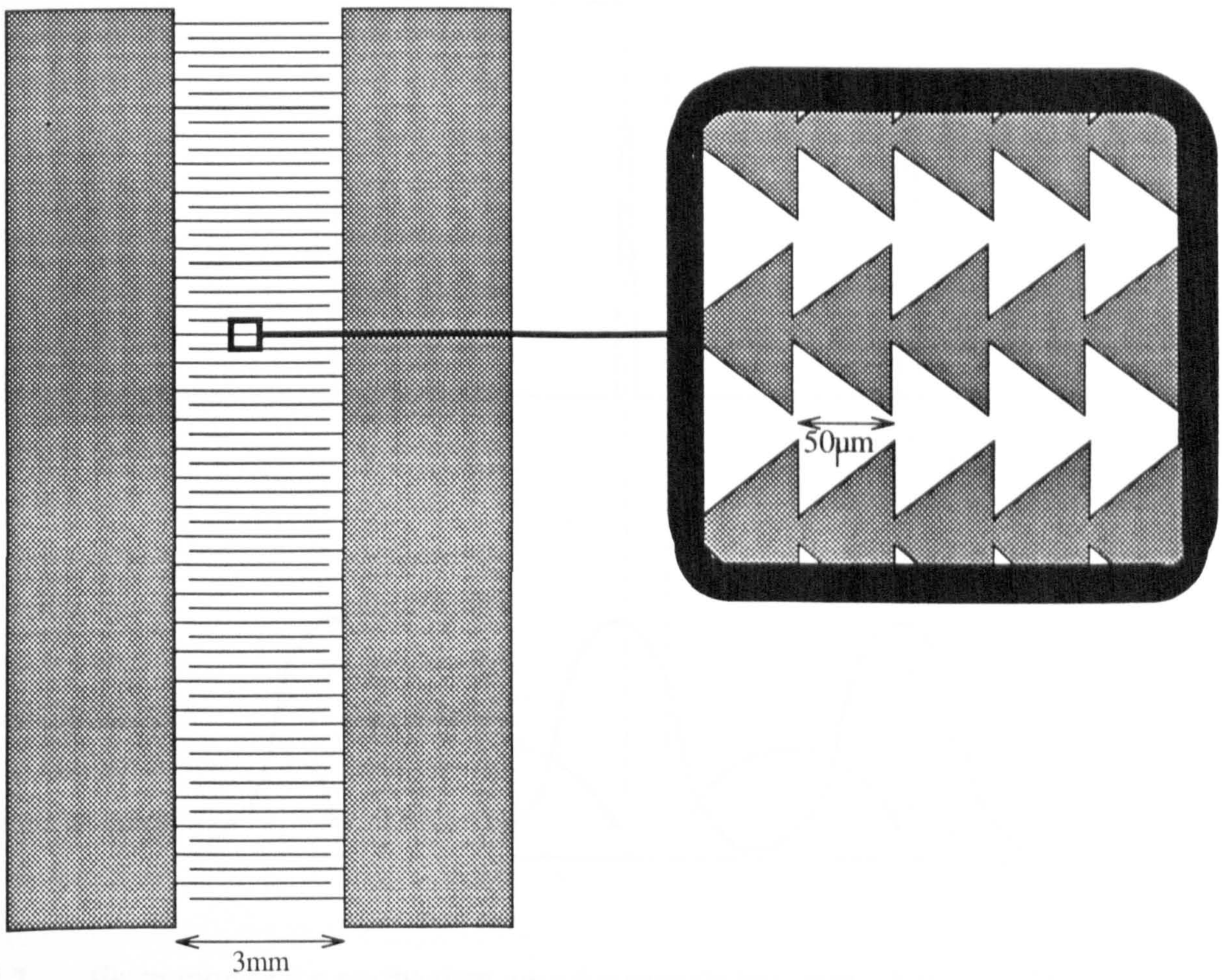

3.1 Schematic of the electrode geometry used by Rousselet *et al.* Two sets of electrodes consist of interdigitated combs, an enlargement of a portion of which is shown in the box. Along these combs, electrodes have triangular protrusions, which are symmetrical across a line between the electrode tips and thus form large triangular spaces.

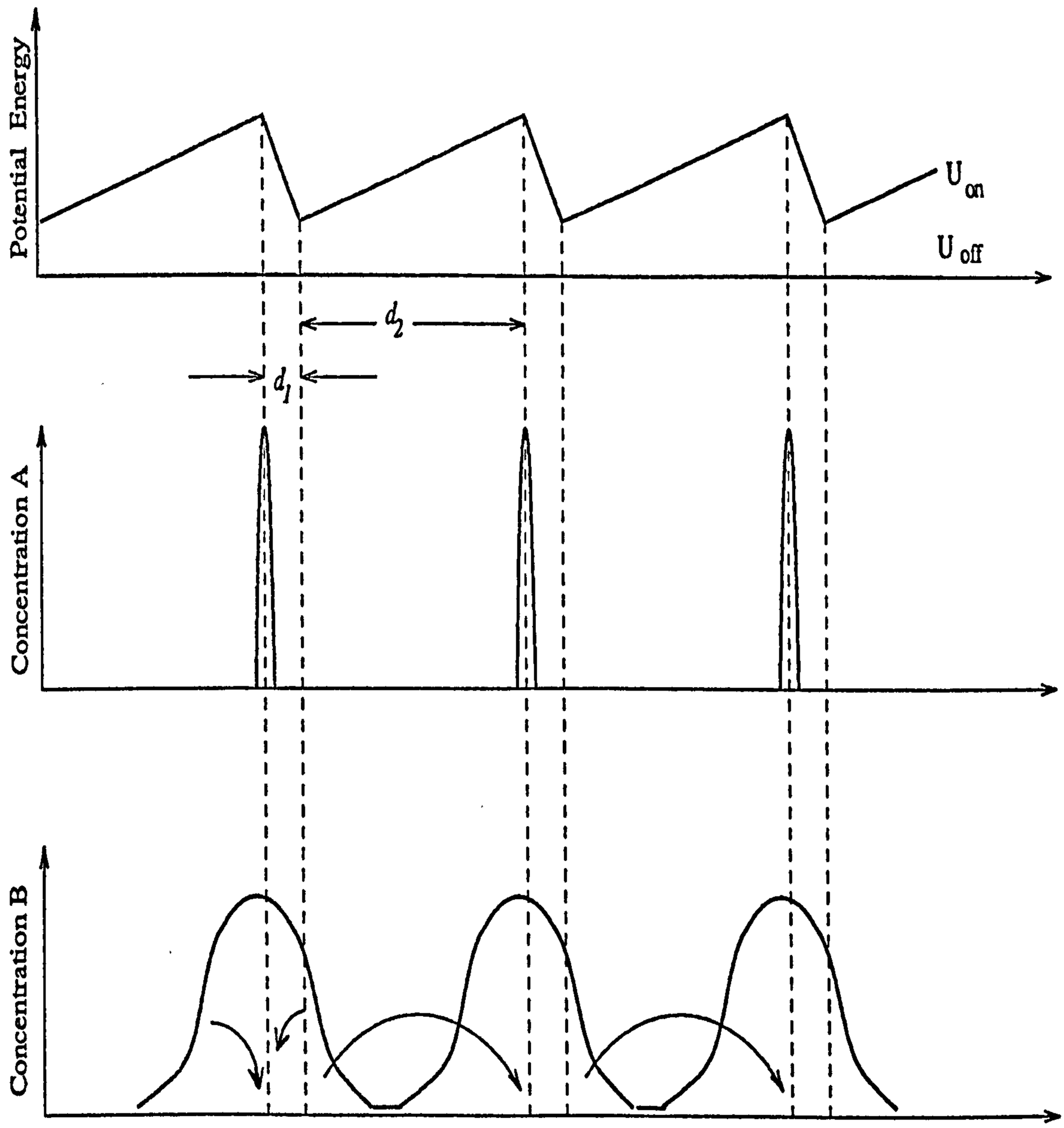

3.2 Illustration of the mechanism used for particle transport. A potential is applied to the electrode structures, resulting in potential energy profile U_{ON} at the line between adjacent electrodes. The potential energy maximum occurs at the electrode tips, with the minimum displaced from the nearest and next-nearest tips by distances d_1 and d_2 respectively. Particles undergoing positive dielectrophoresis collect at the potential maxima, as shown in concentration A. The potential is then removed, producing profile U_{OFF}. Diffusion takes place, and particle concentration takes a form such as that shown in concentration B. When the field is reapplied particles which have diffused beyond the local field minimum are attracted to the next electrode tip, as indicated by the arrows. Hence there is net particle movement to the right.

reapplied. Assuming particle dispersion has taken place at an approximately equal rate, all particles except those which have travelled a distance greater than d_1 will be attracted to the same electrode tip. However, those which have moved greater than d_1 to the right will be trapped by the next electrode on re-applying the field. Provided no particles have moved a distance d_2 to the left, thereby entering the capture area of the *previous* electrode, there is thus a net motion of particles to the right. This is further explained in figure 3.3.

Particle diffusion has been calculated previously using the one-dimensional probablilty distribution on the Fokker-Planck equations [8] along axis x:

$$\frac{\partial P}{\partial t}(x,t) = -\text{div } \mathbf{J}(x,t) \tag{3.3}$$

where

$$\mathbf{J}(x,t) = \frac{\mathrm{D}}{k\mathrm{T}} \mathrm{P}(x,t)\mathrm{F}(x,t) - \mathrm{D}\ \nabla \mathrm{P}(x,t) \tag{3.4}$$

with P indicating the probability density function of the particle location, D is the diffusion coefficient and F is the external force due to an imposed potential. It has been shown [1] that for optimum transport this diffusion will be bounded by the lower diffusion limiting case of the above expressions, where the diffusion rate is small enough to prevent particles passing beyond a single repeating electrode unit in a single time interval τ_{OFF}. This limiting case is given by the expression:

$$\tau_{\mathrm{OFF}} << \frac{(d_2 - d_1)^2}{\mathrm{D}} \tag{3.5}$$

If this condition is met, then for a 2-dimensional isotropic diffusion the probability of particles crossing a circular boundary of radius d_1 in time τ_{OFF}, and thus the fraction of particles having crossed that boundary at that time, is given by the expression [5]:

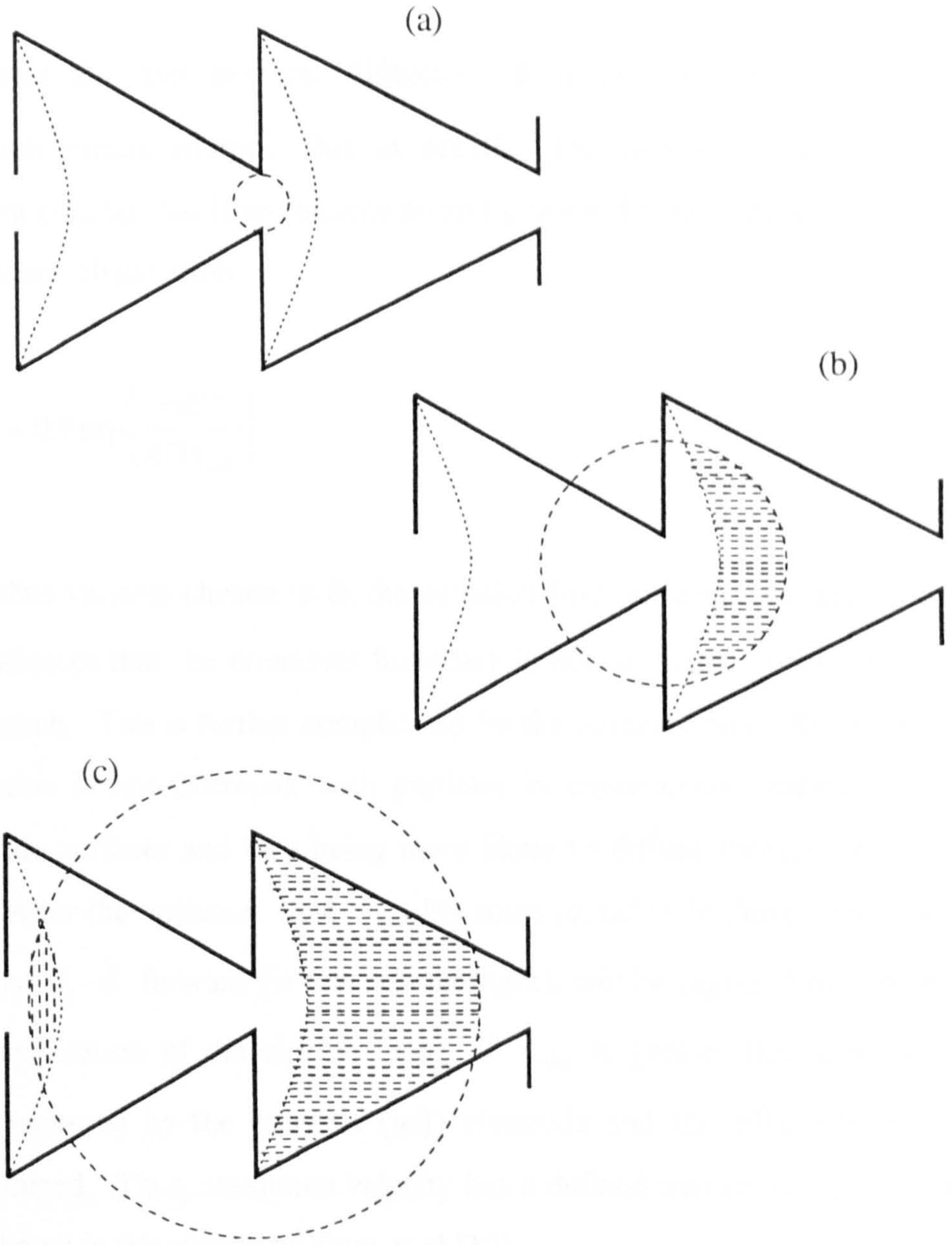

3.3 Consider the inter-electrode gap illustrated in figure 3.3(a). The potential is applied, and particles are trapped at the electrode tips in the region illustrated by the broken line. If the potential is removed, the particles diffuse from this point via Brownian motion. After a period of time, some particles will diffuse beyond the crossover boundary, illustrated by the dotted line. (b) On re-application of the field these particles (represented by the horizontal hatching) will be attracted to the electrode tips at right, resulting in net motion to the right. If the particles diffuse for a longer period then some (indicated by the vertical hatching) will be captured by the electrode tips on the left. This reduces the overall effectiveness of the transporting mechanism.

$$P = \tfrac{1}{2}\exp\left(\frac{-d_1^2}{4D\tau_{off}}\right) \tag{3.6}$$

where the $\frac{1}{2}$ factor indicates isotropic diffusion. Rousselet and co-workers [5] determined through experimentation that in practice the cross-over boundary is approximately semi-circular, but is not exactly so and proposed a more accurate model based on experimental observation:

$$P = 0.9\exp\left(\frac{-d_1'^2}{4D\tau_{off}}\right) \tag{3.7}$$

where d_1' is a radius variable chosen to fit the equation from experimental data. The coefficient 0.9 indicates that the crossover boundary is not semicircular, but may be approximated as such. This is further complicated by the observation by Rousselet *et al* that the diffusion is non-isotropic, with particles in experiments tending not to mount the electrode surfaces and thus being more likely to diffuse forward from the collection point. After the optimum time τ_{OFF} [9] some particles, ie those which have travelled a distance d_2-d_1 forward (ie towards the right), will be captured by the next electrode on re-application of the electric field. If τ_{OFF} is greater than this, some particles will be captured by the previous (left) electrode and the efficiency of the ratchet will be reduced. Thus, maximum velocity has a defined maximum period time ($\tau_{OFF}+\tau_{ON}$) as shown in the studies of Prost et al [10].

Rousselet et al [5] determined that the boundary between adjacent capture areas is neither circular nor straight, following a more complex pattern. It is thus difficult to evaluate the efficiency of the geometry in terms of the proportion of cells migrating forward within the time τ_{OFF}. Ajdari and Prost [1] proposed a dimensionless factor x as a ratio based on the distance d_1 as a proportion of the total distance d. A similar measure of this ratio Λ has been used here for the comparison of different electrode geometries. Λ is expressed as the ratio of the distance along the axis through the centre of the gaps between the electrodes along which particles are attracted to the

next electrode tip at time τ_{OFF}, as a proportion of the total distance between neighbouring electrode tips:

$$\Lambda = \frac{d_2 - d_1}{d_2 + d_1} \tag{3.8}$$

The value Λ may be interpreted as a measure of asymmetry, and may take values from 0 (a symmetrical electrode assembly) to 1 (complete asymmetry). In practice Λ=1 is unattainable, but by maximising Λ ratchet performance may be measured and improved.

In order to gain greater insight into the processes occuring in practical electrode structures, the electric fields and forces around such structures were simulated. A limited study has previously been performed by Rousselet [11] in two dimensions, using the Finite Difference model [12]. The results obtained by that method have been verified and extended by undertaking advanced three dimensional studies using the Finite Element model, as described in the previous chapter. Calculations were performed using an integrated meshing/calculation/postprocessing program (Maxwell: Ansoft Inc.) to calculate the electic fields, and also to calculate dielectrophoretic forces based on equation (3.1). Fields were simulated in three dimensions to provide highly accurate data, using tetrahedral elements to accurately model the triangular electrode shapes. Two-dimensional studies were also performed for relative performance optimisation, where obtaining an accurate result for a single line was considered to be of greater importance than obtaining wide-area results with the expense of large quantities of computing time. Two-dimensional results were also used to confirm 3-D results with larger error margins. Adaptive meshing was employed, with a maximum of approximately 10,000 nodes per simulation. In order to control meshing, the program attempts to iteratively minimise potential energy across the solution space by examining the discontinuity of the second differential of the potential at element interfaces [13]. This error, cumulative across the solution space, is used as a total local, rather than global residual, error measurement [14]. Overall local error limits of

2% (3D simulations) and 0.01% (2D simulations) were imposed. Calculations were performed on a Pentium-90 PC.

3.3 Results and Discussion

3.3.1 Electric Field Distributions

The electric field across the electrodes described in figure 3.1, in a plane 3μm above the upper surfaces of the electrodes, is shown in figure 3.4. Peak electric field at the electrode tips is 4V/μm, falling to 1.2V/μm in the 3μm plane above the tips. The crossover point between repeating triangular electrode units is visible as a 5μm-wide band at which the electric field is relatively stationary at a minimum value of approximately 0.4V/μm, extending in an elliptical arc from the corners of the triangular region, the centre of which passes through the point 17μm from the nearest electrode tips along the line between the electrode tips. In terms of the comparison factor (the transport factor Λ described in equation (3.8)), the measurement d_1 = 17μm produces a transport factor Λ=0.32. This elliptical boundary agrees well with the practical observations reported [5] where the boundary has been described as falling between a semicircle of radius d_1 and a straight boundary a distance d_1 from the previous electrode tip.

Previous 1-dimensional simulations of electric field conducted by Rousselet [11] using a Finite Difference model of the ratchet electrodes provided a transport factor Λ of 0.375, based on a geometry with a shallower slope angle of the leading electrode edge due to a narrower electrode base (this geometry has a maximum inter-electrode gap width of 40μm rather than 50μm). This value agrees well with the prediction here, given the difference in geometries and the simplicity of the earlier model. Furthermore, allowing for the difference in geometry as discussed in section 3.4.2, the value calculated here for the geometry described in [11] is indeed Λ=0.375.

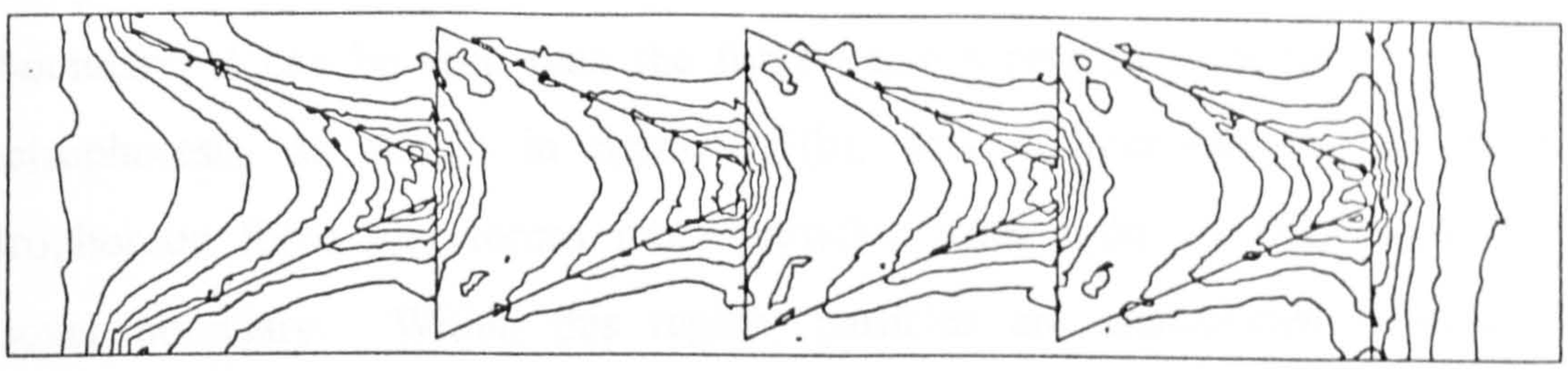

3.4 The electric field strength in a plane 3μm above the plane of the electrodes shown in figure 3.1. The crossover boundary is visible as a semi-ellipsoid band reaching from the inner corners of the central triangle through a point ⅓ of unit length d from the nearest electrode tips. The high-field region is visible at the electrode tips.

3.3.2 Dielectrophoresis

The positive and negative unit vectors of positive and negative dielectrophoretic force are shown in figure 3.5(a) and (b) respectively. The magnitude of these vectors, which are equal to one another and equivalent to the potential energy, vary according to figure 3.5(c).

Considering positive dielectrophoresis first, it is evident that, upon application of the field more particles will be attracted towards the right of the electrode assembly to the electrode tips than to the right by a ration of approximately 2:1. The crossover boundary is evident, with the force vectors being tangential to this boundary. Across the boundary, it can be seen than the force vectors reverse direction. Negative dielectrophoresis, as shown in figure 3.5(b), acts counterwise to the positive diectrophoretic force and forces most particles from right to left, *towards* the crossover boundary. Within this region, particles are transported towards the electrodes along the crossover boundary. This effect has been reported as an attractive force acting on latex beads in high frequency electric fields by Rousselet in experimentation [11]. However, the size of the force across the crossover region, where motion should take place towards the electrode corners, is several orders of magnitude smaller at the crossover boundary than at the electrode tips. Thus, larger particles pushed into the crossover region may remain in this region, forming a crescent shape. This formation is evident from a contour map of electric field, shown in figure 3.5(c).

An interesting and potentially useful phenomenon resulting from the negative dielectrophoretic force distribution is that particles are transported to the left of the diagram rather than to the right, as is the case in the right-to-left motion induced by positive dielectrophoresis, and the collection point is displaced from the previous location, at the electrode tips. Using the Brownian motion harnessing of thermal ratcheting principle, it is theoretically the case that over several cycles negatively dielectrophoretic particles should be propelled in a continuous right-to-left fashion, in contrary motion to the macroscopic force experienced by particles undergoing positive dielectrophoresis.

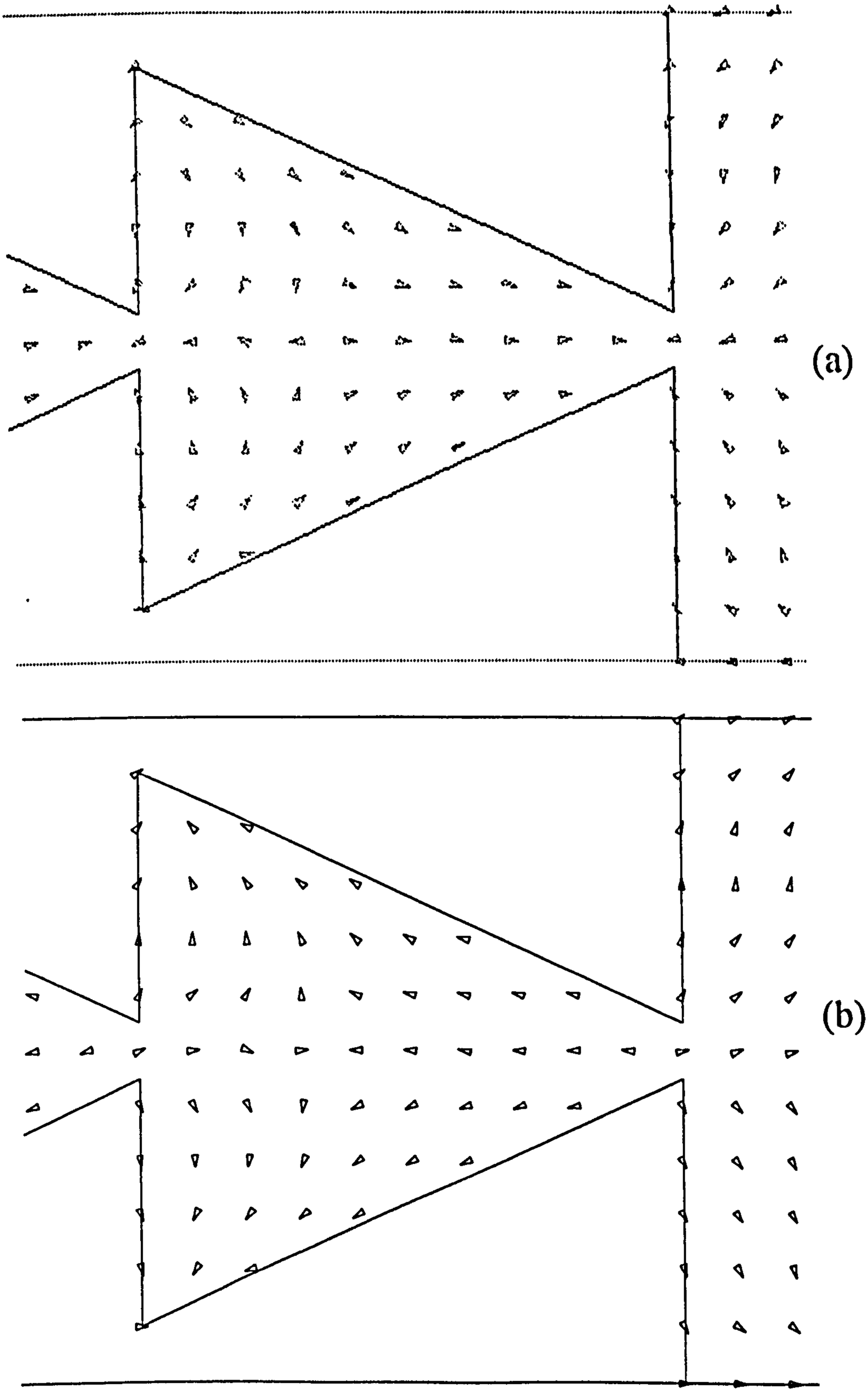

3.5 Unit direction vectors of (a) positive and (b) negative dielectrophoretic forces generated in a plane 3μm above the electrode geometry shown in figure 3.1. The magnitudes of these forces are shown in figure 3.5(c). Dielectrophoretic force is highest near the electrode tips, and lowest at the crossover boundary. At this point the force is so low that particles responding to negative dielectrophoretic force may collect at the crossover boundary rather than be transported to the electrode surfaces.

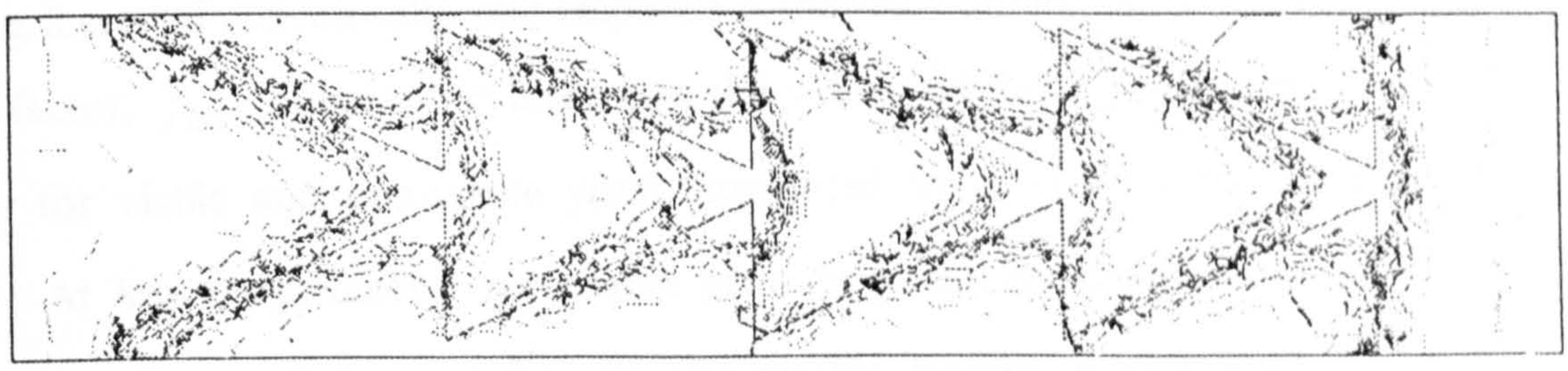

3.5(c) The magnitude distribution of dielectrophoretic force across plane 3μm above the upper electrode surfaces. The positive and negative collection areas are visible as pale regions at the electrode tips and crossover boundaries respectively. The force at the crescent-shaped crossover boundary is $1/100$ that at the high-field region, and so may be insufficient to move particles held within it.

3.3.3 Continuous Separation using Dielectrophoretic Ratchets

The mechanism presented here for the transport of colloidal particles may also be applied to the separation of particles from a heterogeneous population. As the dielectrophoretic force attracting the particles between electrode tips is related to the AC dielectric properties of the particles, particles with differing dielectric properties will respond differently when subjected to electric fields of a given frequency. Non-polar particles will not respond to dielectrophoretic forces and thus a suspension of polarised and non-polarised particles will respond within a ratchet assembly by the former being drawn out of the population whilst the latter remains in place.

The use of negative dielectrophoresis allows this concept to be extended further. The controlling factor of dielectrophoretic response is the real component of the Claussius-Mossotti factor, f_{CM}. Figure 3.6 illustrates the values of Re[f_{CM}] as a function of frequency for viable and non-viable yeast suspended in a medium of conductivity $40\,\mathrm{Sm}^{-1}$. At low frequencies, non-viable yeast is positively dielectrophoretic and would thus be attracted forward through the ratchet system, whilst viable yeast is negatively dielectrophoretic and is driven backwards through the system. At approximately 3kHz, the dielectrophoretic response of the viable yeast drops towards zero and the cells remain motionless whilst the non-viable cells continue to move forward. Beyond this frequency, the viable yeast becomes positively dielectrophoretic and travels forward with the non-viable yeast. This response is maintained up to 1MHz at which the non-viable yeast becomes less positively diectrophoretic until reaching its crossover point and remaining unaffected by the ratchet. Above this frequency the non-viable yeast is driven backwards through negative dielectrophoresis whilst the viable cells continue to be driven forward.

The dielectrophoretic response is a sensitive function of the conductivity of the medium conductivity. Thus by careful selection of medium, it is possible to perform ratchet-based continuous separation of particles using dielectrophoretic forces, based on a variety of separation methods as described above. This has potential applications similar to methods of continuous dielectrophoretic separation proposed elsewehere

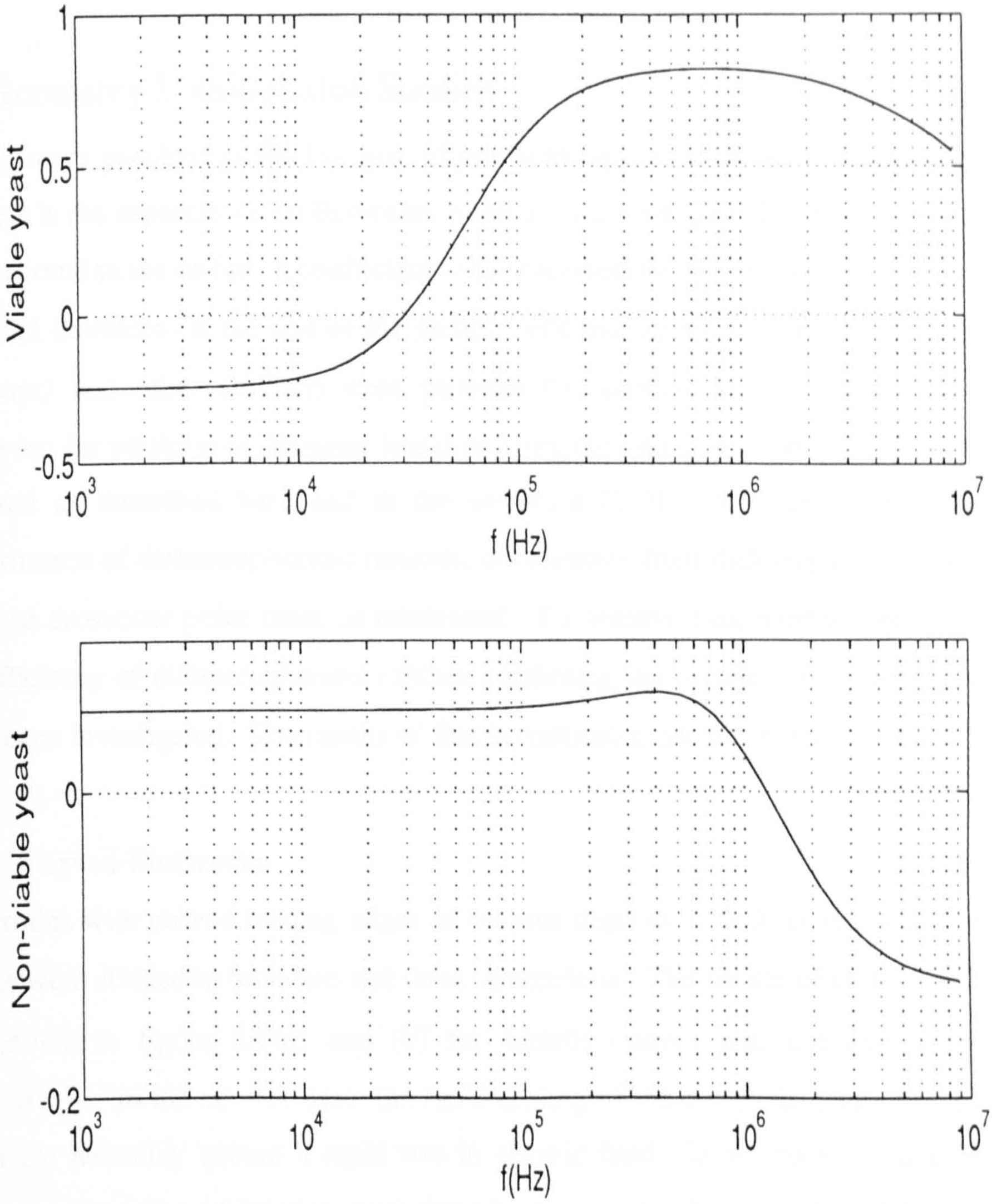

3.6 The real component of the Claussius-Mossotti factor, Re[f_{CM}], for viable and non-viable yeast cells, as a function of frequency.

[14], but appropriate to situations where it is impractical to provide a fluid flow through the particle chamber or where smaller numbers of particles need be separated.

3.4 Geometry Manipulation Studies

The primary problem in the building of practical separators based on forced thermal ratchets is the dependence on Brownian motion. The total particle velocity is inversely proportional to the diffusion coefficient D as described by the Einstein-Stokes equation [11] and therefore on the size of the particle. For biological cells (approximately 5μm diameter) and other similarly-sized particles the process is thus quite inefficient. However, for particles of diameter less than 1μm, the system is more effective and may be used as described here and in the literature [1-5]. In order to improve the performance of dielectrophoretic ratchets, the distance from dielctrophoretic collection point to crossover point must be minimised. To achieve this, methods of improving the efficiency of dielectrophoretic ratchets, including the response for larger particles, have been investigated. The results of that investigation are presented below.

3.4.1 Curved Electrodes

Electrodes with curved leading edges of various degrees in both convex and concave senses were studied in both two and three dimensions. The results of these simulations are shown in figure 3.7(a) and (b) for sample convex and concave geometries respectively. In the convex case, the rapid closing of the electrode neck over distance along the assembly causes a rapid rise in electric field. In practice this implies that collection is rapid, and the crossover point is close to the electrode tips of the previous electrode. However, at the tips the convex nature of the geometry draws the electrodes near each other for a short distance before the electrode tips. This results in an unfocussed high-field region rather than a distinct point, and thus the positive dielectrophoretic collection point covers a region some 5μm long. This gives a lower factor Λ, with values of 0.3 and 0.28 for increasing convexity of the electrodes.

In the case of concave electrodes such as those shown in figure 3.7(b), the increasing symmetry of the electrodes towards a series of opposing "needles" results in an

unfocussed low-field region and near-symmetrical field peak which results in a poor value of Λ. Calculated values decrease in a similar fashion to convex electrodes.

3.4.2 Dimension Manipulation

Consider the electrode geometry illustrated in figure 3.8. Based on the standard "Christmas Tree" electrode geometry [5], two parameters have been introduced which may be varied in order to test for features which may optimise the electrode transport efficiency. Parameter *a* is the distance which a previous electrode tip projects into the hollow area of the next electrode unit, and is measured relative to the standard geometry. Parameter *b* is the distance between the end of the previous unit and the base of the next unit, and is also measured relative to the standard case. Manipulation of these two characteristics allows for the approximate modelling of several other parameters, such as electrode distance. As described previously, simulation in terms of the angles of the leading and trailing electrode edges can accurately model geometries such as Rouselet's [11] narrower electrode geometry.

Simulations have been performed for a wide range of values of *a* and *b* using a 2-dimensional model. The results have been analysed using the Λ transport ratio parameter as a means of comparing transport efficiency. This method of comparison was chosen due to its ease of calculation, due to the increasingly complex geometry of the crossover boundary with increasing field non-uniformity, which makes an evaluation in terms of area or 2-dimensional probability distribution difficult to evaluate. Figure 3.9 provides a comparison of Λ factors for a wide range of values of variables *a* and *b*. As can be seen, the general trend is that factor Λ increases with increasing values of *a* and *b*. This is to be anticipated, as increasing both these factors increases the field non-uniformity along the centre of the electrode channel. For some values of *a* and *b* the increase in Λ is small, or a local decrease is evident. These are largely present for higher values of *b*, where successive electrode units are placed further apart and hence a low-field region tends to form at electrode roots. This causes a defocussing of the electric field minima at which the crossover of attraction is located and hence the location of the actual crossover is more highly influenced by small local field distortions caused by electrode shape. In practical situations,

(a)

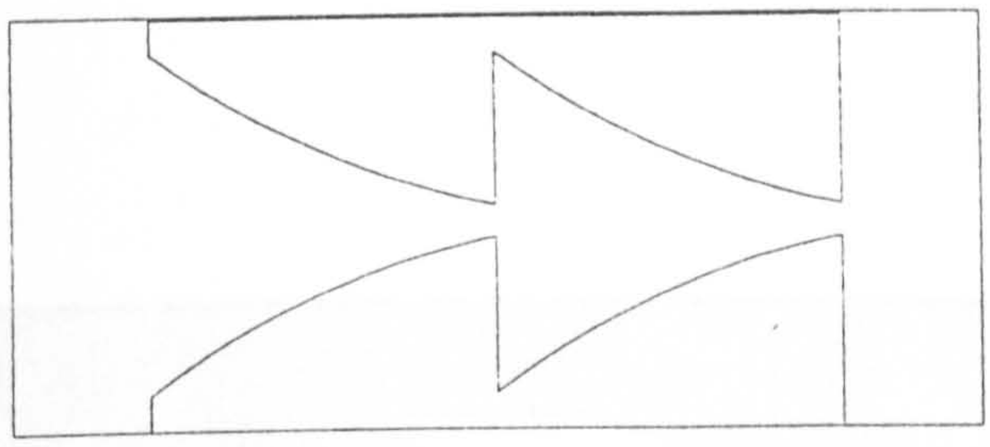

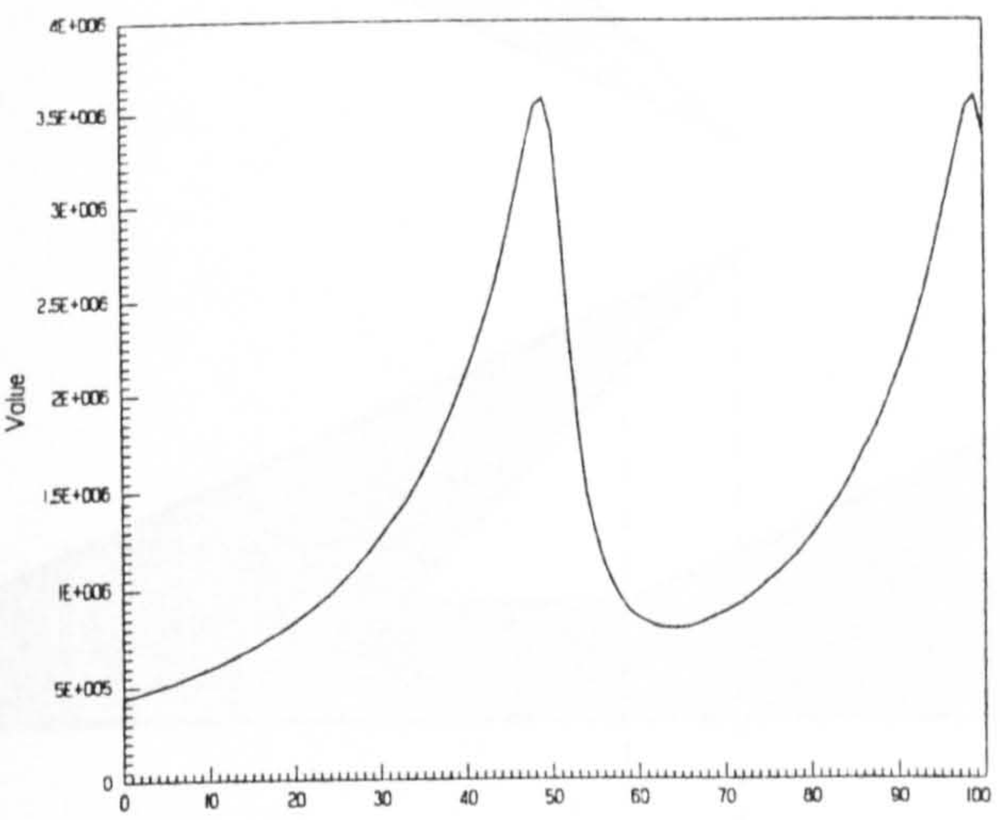

(b)

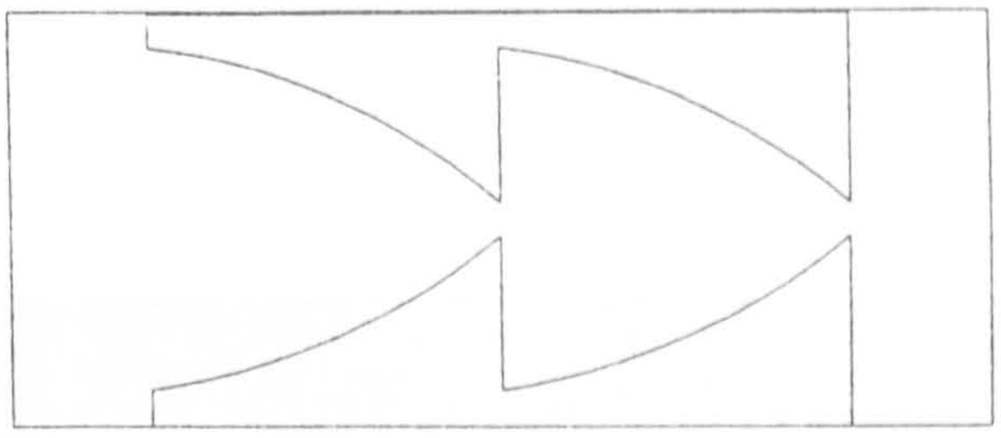

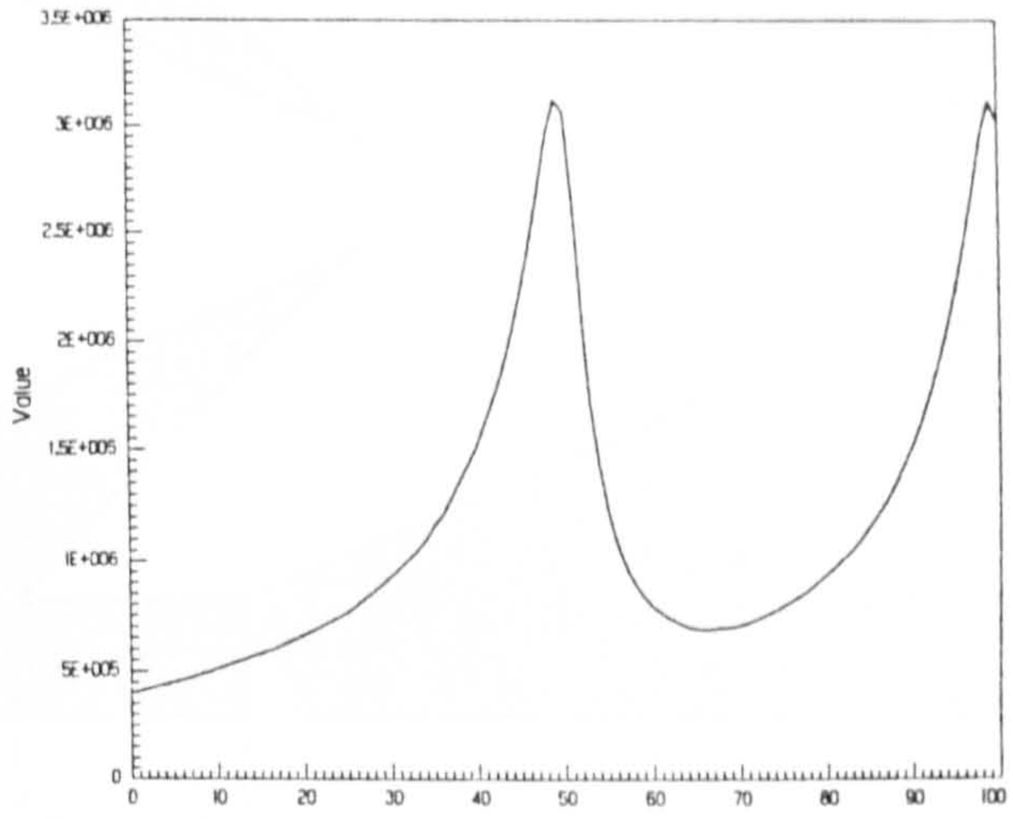

3.7 (a) Convex electrode geometry and associated electric field profile at a line through opposing electrode tips. (b) Concave electrode geometry and associated electric field profile.

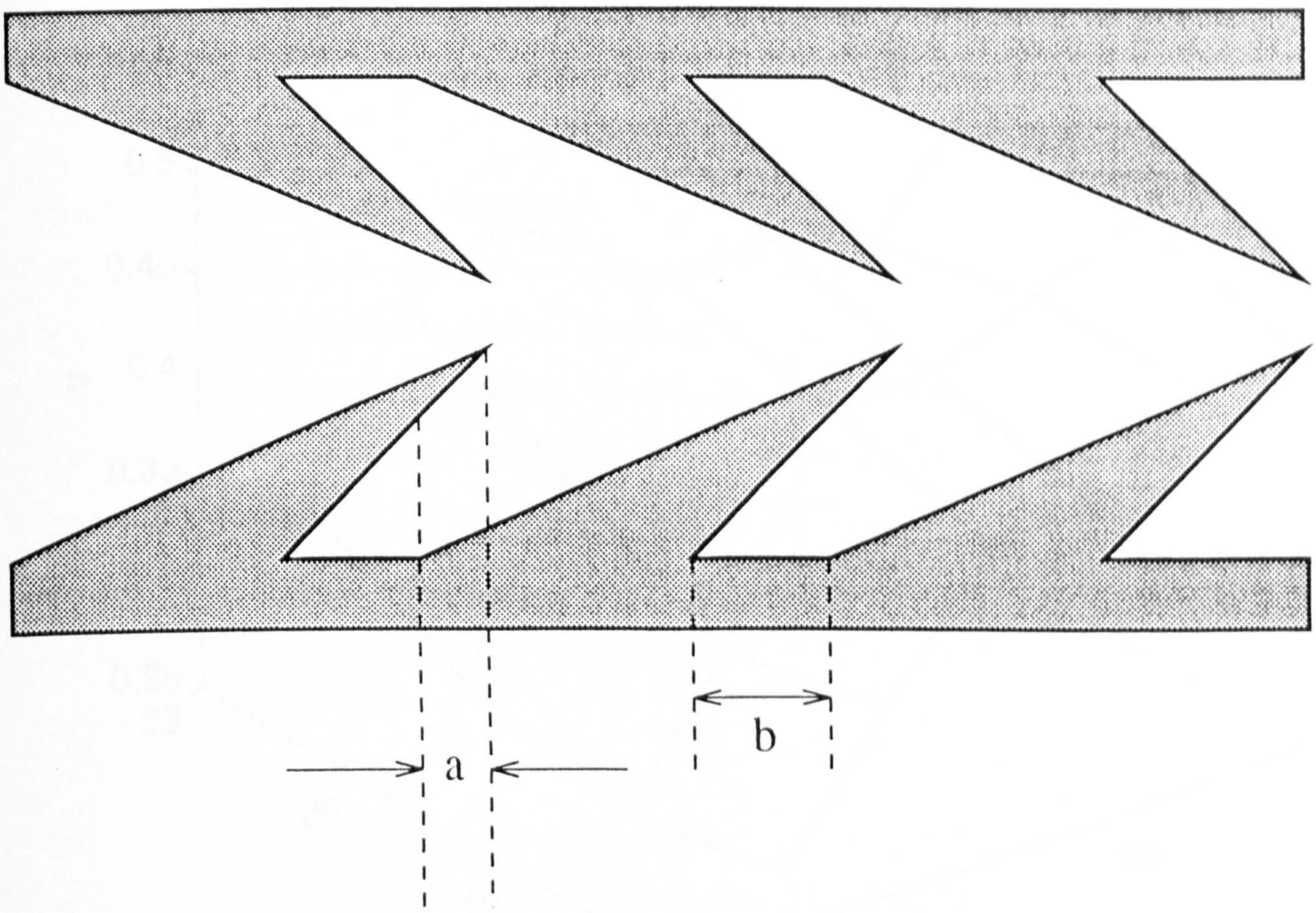

3.8 A generalised electrode geometry used for optimisation. Electrode tips are extended a distance *a* beyond the base of the mext electrode unit. The electrodes are "undercut" by a distance *b* by recessing the trailing electrode edges.

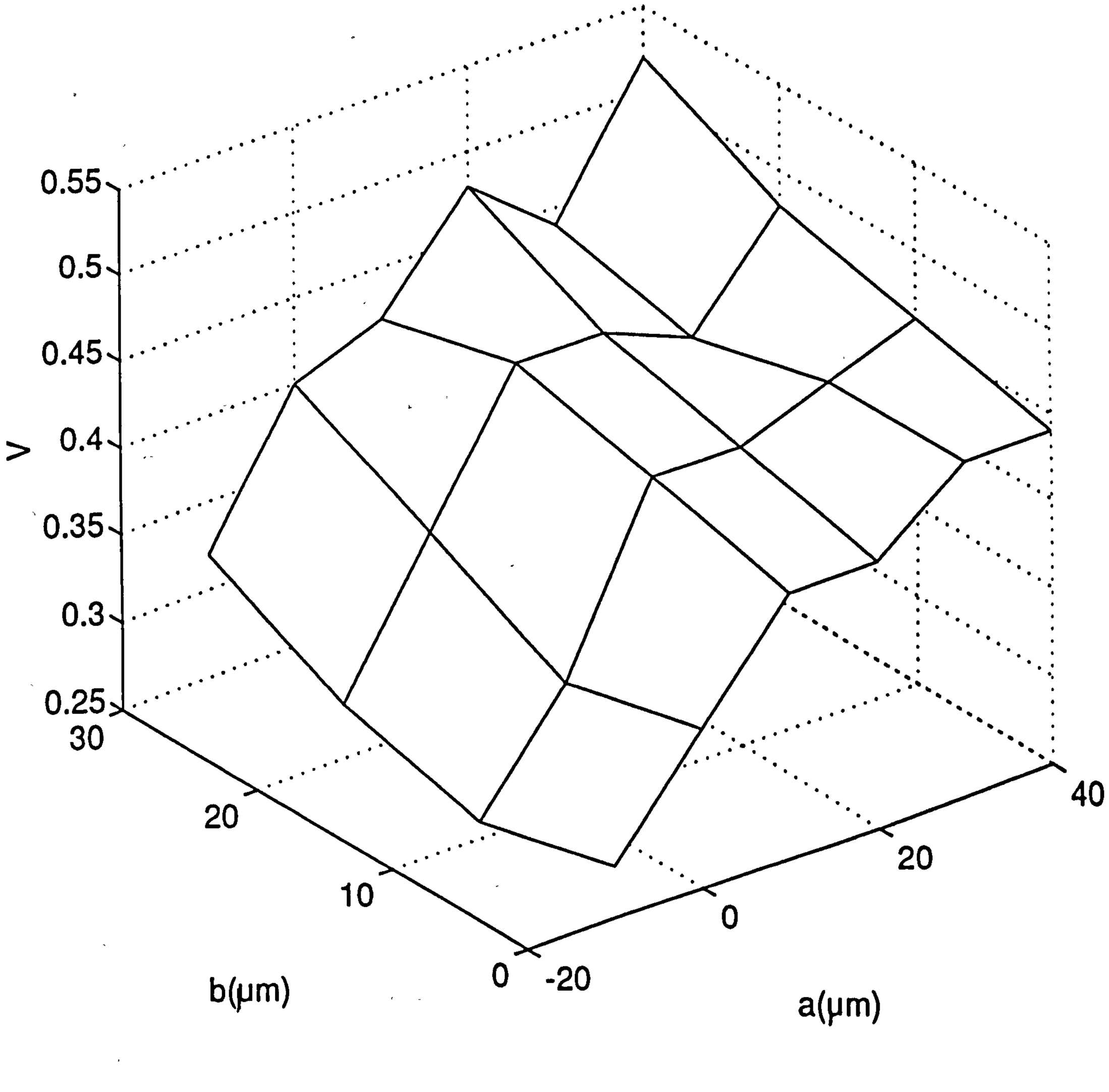

3.9 Graphical representation of the variation of transport factor Λ with variation of distances *a* and *b*. Whilst there is a general increase in Λ with increasing *a* and *b*, at higher values this increase becomes unstable due to variations in the size of field minima. It is proposed that the "safest" optimum geometry, from which the produced electrodes may vary slightly with low risk of performance degradation, occurs at a=10-20μm, b=20μm.

electrodes of the dimensions required to produce higher values of Λ presented here would be difficult to realise. For the case where a=40μm and b=30μm, the stalks of the electrode ratchets would be triangles no more than 5μm wide and over 90μm long. Thus, implementation of more extreme cases is difficult and does not guarantee improved performance due to the susceptibility to electrode conformations in these cases. From figure 3.9, the most stable geometry offering improved performance is the a=10-20μm, b=20μm case. Beyond these limits, the electrodes become too thin and Λ is no longer guaranteed to increase with increasing a and b. These characteristics provide a transport factor of Λ=0.44, and improvement of 40% over the standard design.

3.4.3 Stacked Ratcheting Mechanisms

The primary drawback with using forced thermal ratchets as a practical method of particle separation is the reliance on Brownian motion to provide a means of driving particles from the collection points. This restriction limits the use of such a separator to applications involving small particles with correspondingly large diffusion constants. Practical diffusion rates for micron-sized particles [5] are approximately 120 seconds for 40% of particles to pass one unit forward. This may be improved by optimising electrode design, but is unlikely to attain the rates required for practical continuous particle separation.

Proposed here is a mechanism whereby the design principles of thermal ratchets is retained, but the reliance on Brownian motion to provide the driving mechanism is eliminated. Consider the electrode assembly shown in figure 3.10. The assembly is composed of two pairs of ratchet electrodes, with one pair located 50μm above the other and displaced along the main axis by half of one unit length, ie 25μm. Potentials are applied to only one pair of electrodes at any given time.

If a mixture of particles is suspended between the electrodes and potentials are applied to the lower pair of electrodes, particles undergo dielectrophoresis and are attracted to, or repelled from, the electrode tips towards their respective collection points. After time τ_{ON} collection has taken place and the cells have aggregated. At this time the

(a)

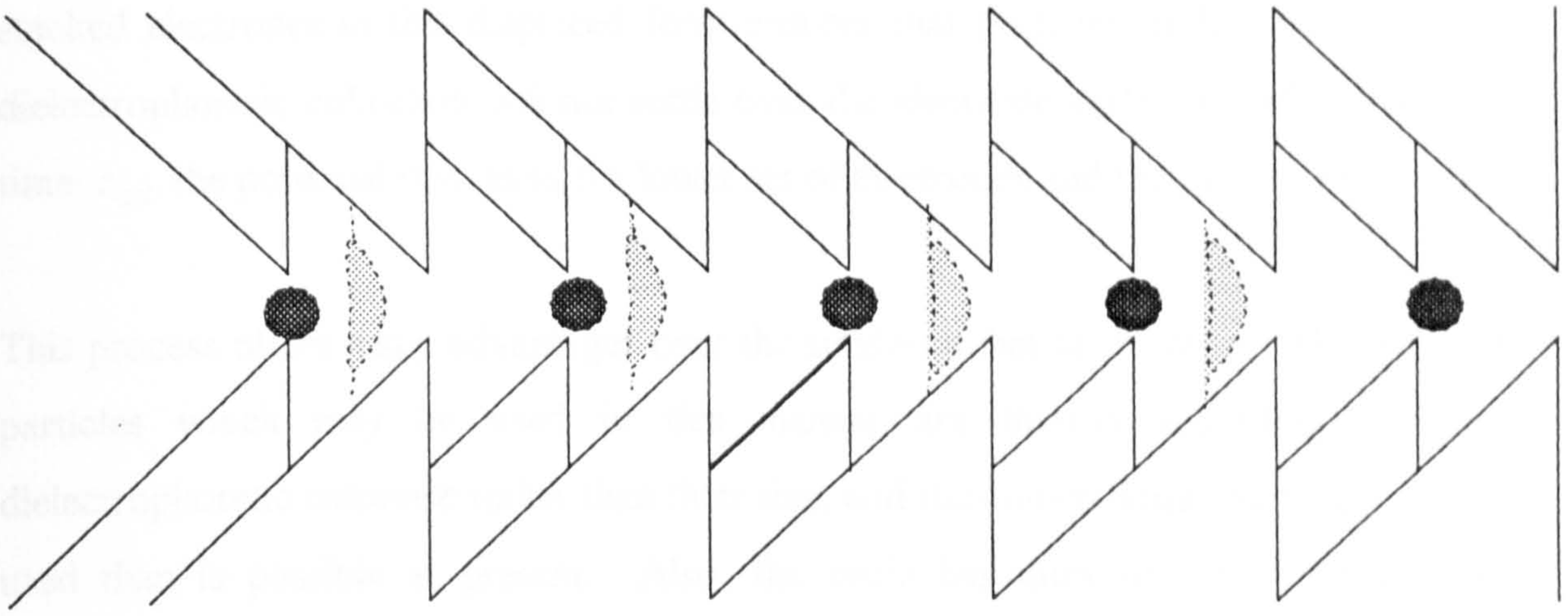

(b)

3.10 A proposal for a continuous separator based on two pairs of stacked ratchet electrodes, as shown in figure 3.10(a). When the bottom electrode pair is active, particles undergoing positive dielectrophoresis are attracted to the tips of these electrodes, whilst those undergoing negative dielectrophoresis collect at the crossover boundary. Once collection has taken place, potentials are removed from the lower electrodes and applied to the upper set. The particles at the electrode tips are all held beyond the crossover boundary for these electrodes and are attracted forward, whilst those at the previous crossover boundary are repelled backwards. After this collection has taken place the potentials are reversed to their original state. In this manner 100% of the suspended particles are continually transported through the electrodes.

potentials on the lower pair of electrodes are removed and the top pair of electrodes are activated. Those particles undergoing positive dielectrophoresis, located at the previous collection point 25μm from the new collection point, will be attracted forward to that point. Similarly, particles undergoing negative dielectrophoresis will be repelled to the collection point of the previous cell. The repulsion of the two stacked electrodes in this displaced form ensures that particles undergoing negative dielectrophoretic collection will not settle over the electrode surfaces. After a further time τ_{ON} the potential reverts to the lower set of electrodes and the cycle is repeated.

This process offers many advantages over the single-ratchet mechanism. The types of particles which may be used in this manner are limited according to their dielectrophoretic response rather than their size, and thus much larger particles may be used than is possible at present. Also, the cycle has duration $2\tau_{ON}$ rather than $\tau_{OFF}+\tau_{ON}$ in the single-pair case. Experiments [5] have shown that for particles of approximately 1μm diameter, τ_{ON} has value 30 seconds or less compared to τ_{OFF} of approximately 120 seconds. Thus the stacked-ratchet method offers approximately twice the efficiency of the first method, a value which increases with increasing particle size. This is further enhanced by the percentage of particles being drawn forward per cycle approaching 100%, an effect arising from the fact that at the time of the removal of potential from one electrode pair, the particles are located at the tips of these electrodes, at a point which is located beyond the crossover boundary of the other electrode pair (see figure 3.10).

3.5 Conclusion

Recent theoretical study has shown that potential "ratchets", in the form of non-symmetrical potentials, can possibly induce macroscopic motion in particles undergoing Brownian motion. Recent experimental work has confirmed this through the use of dielectrophoretic force generated in "Christmas-tree" shaped electrodes. Such ratchets have many potential applications, but the complex nature of the electric field surrounding the electrodes has made analytical study of the phenomenon difficult.

Presented here is a three-dimensional study of the electric field and dielectrophoretic force generated by the Christmas-tree electrode geometries. In studying the dielectrophoretic response of the particles, it is proposed that the possibility exists for particle separation according to the dielectric properties of the particles, in addition to particle size considerations. The use of dielectrophoresis allows not only the drawing of one type of particle from a heterogeneous population, but also the displacement of two types of particles in opposite directions. Thus, a particle of a given type may be driven forward through the ratcheting system in the manner proposed previously, whilst particles of another type may be driven backwards, against the flow of the first type.

The location and shape of the inter-unit crossover has been determined, the geometry of which fits with experimental data. Furthermore, by establishing a means of comparison the crossover points of several electrode geometries have been systematically studied and conclusions on the optimisation of ratchet electrode geometries have been presented. A proposed geometry also allows for the elimination of the Brownian motion requirement, which thus allows the use of the ratchet principle in the transportation and separation of larger particles, and in a more efficient manner, than is possible in the present geometry of Rousselet *et al.*

Finally, although the concept of forced thermal ratchets is interesting, it is potentially not as effective for particle transport as the travelling wave dielectrophoresis effect discussed in chapter 5 due to the reliance on Brownian motion to provide motive force. However the reliance of travelling wave electrode arrays on complex wiring systems to provide the multiphase potentials makes ratcheting more attractive for small separators of as part of a larger, embedded electrode system where external connectors are difficult to insert.

References

[1] Ajdari A and Prost J 1992 *C. R. Acad. Sci. Paris* **315** 1635-1639

[2] Chauwin J-F, Ajdari A and Prost J 1994 *SFP 4émes Journées de la Matire Condensèe* 2005

[3] Magnasco MO 1993 *Physical Review Letters* **71** 1477-1481

[4] Astumian RD and Bier M 1994 *Physical Review Letters* **72** 1766-1769

[5] Rousselet J, Salome L, Ajdari A and Prost J 1994 *Nature* **370** 446-448

[6] Pethig R, Huang Y, Wang X-B and Burt JPH 1992 *J. Phys. D: Appl. Phys.* **25** 881-888

[7] Wang X-B, Huang Y, Burt JPH, Markx GH and Pethig R 1993 *J. Phys. D: Appl. Phys.* **26** 1528-1535

[8] Risken H 1984 *The Fokker-Planck Equation: Methods of Solution and Applications* (Berlin: Springer-Verlag)

[9] Doering CR, Horsthemke W and Riordan J 1994 *Physical Review Letters* **72** 2984-2987

[10] Prost J, Chauwin J-F, Peliti L and Ajdari A 1994 *Physical Review Letters* **72** 2652-2655

[11] Rousselet J 1995 *Migration sans force macroscopique de particules browniennes: application à la séparation en taille* PhD thesis, L'Universite Bordeaux 1

[12] Binns KJ and Laurenson PJ 1963 *Analysis and Computation of Electric and Magnetic Field Problems* (Oxford: Pergamon Press)

[13] Zienkiewicz OC and Taylor RL *The Finite Element Method, vol.1, 4th ed.* (London: McGraw-Hill)

[14] Binns KJ, Lawrenson PJ and Trowbridge CW 1992 *The Analytical and Numerical Solution of Electric and Magnetic Fields* (Chichester: Wiley)

[15] Markx GH and Pethig R 1995 *Biotechnology & Bioengineering* **45** 337-343

Chapter 4

Analyses of Electric Fields Used in Electrorotation Studies

4.1 Introduction

Since the first demonstration by Arnold and Zimmermann [1] and Mischel *et al* [2] that rotating electric fields can be used to induce the controlled rotation of biological cells, there has been a steady increase of interest in exploiting this electrorotation technique as a non-invasive method for studying the electrical properties of cells as a function of their physiology [e.g. 3-5]. The method has also been used to investigate the physico-chemical properties of colloidal particles [6], and to assay the presence and viability of micro-organisms in water [7]. Considerable progress has been made in developing the theory of electrorotation for realistic cell models [e.g. 8-10], in unifying it with the theories of the dielectrophoretic and dielectric properties of cells [11,12], and in developing rotating field generators [13]. These studies show that the torque exerted on a particle is proportional to the square of the rotating field's magnitude. However, apart from the recent resistor-network-based analysis of Hölzel [14], no work appears to have been directed towards understanding to what extent the accuracy and reproducibility of electrorotation spectra are limited by the uniformity of this field. Hölzel's [14] insights into this problem are extended here by performing computer-aided simulations of the spatial variations of the magnitude and phase of the rotating field generated by ten electrode designs that can be fabricated using standard photolithography.

Rotating electric fields can be generated using an arrangement of the form shown in figure 4.1, where the four electrodes are addressed by four sinusoidal voltages, of equal magnitude, phased 90° apart. More generally n electrodes in number, phase

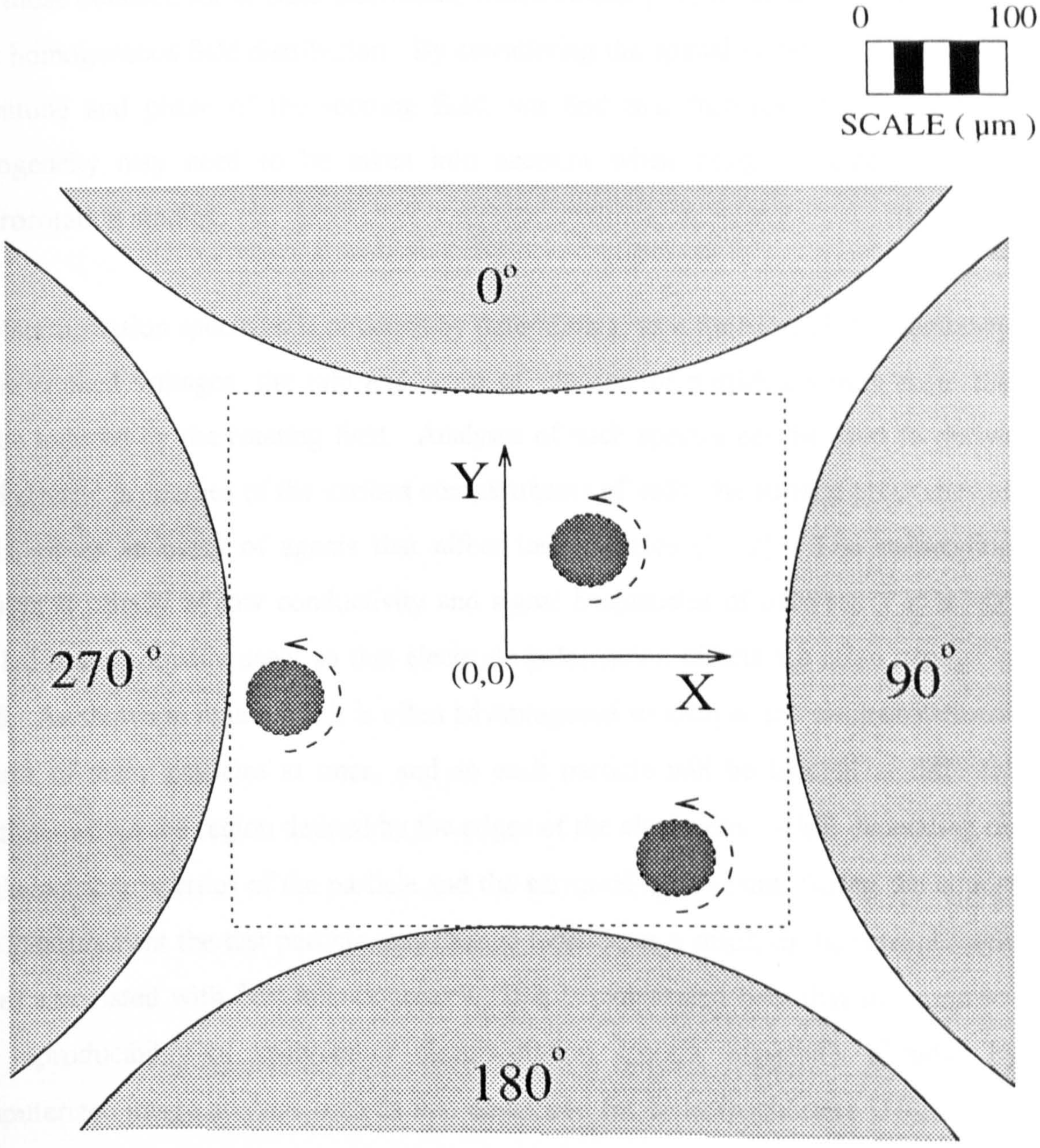

4.1 Particles (not drawn to scale) subjected to rotational torque using electrodes of polynomial geometry. The phases at time t=0 of the cosine voltages (10V pk) shown assigned to each electrode produces a field rotating in an anti-clockwise sense. The square between the electrode tips, in a plane 3μm above the 0.2μm thick electrodes, defines the region over which the rotating field is analysed.

shifted 360°/n apart, and of form ranging from flat plates to wire pins can be used. The focus of attention in this paper is the polynomial electrode design shown in figure 4.1, which has been used in combined dielectrophoresis and electrorotation studies [5,15]. The field characteristics produced by this electrode geometry are compared with those obtained for circular electrodes, which Hölzel [14] concluded generates the most homogeneous field distribution. By considering the spatial variations of both the magnitude and phase of the rotating field, we find that features other than field homogeneity may need to be taken into account when designing electrodes for electrorotation studies.

An electrorotation spectrum is obtained by determining, as a function of the frequency of the applied voltages, the rate and sense of rotation of particles arising from the torque induced by the rotating field. Analyses of such spectra can be used to derive the dielectric properties of the various compartments of cells, the surface properties of beads, or as an assay of agents that affect test particles [1-12]. The suspending medium is usually of low conductivity and signal frequencies of between 1 kHz and 100 MHz are normally used, so that electrode polarization effects are often negligibly small. As shown in figure 4.1, it is often advantageous to analyse the electrorotational spectra of many particles at once, and so each particle will be located at different positions within the region defined by the edges of the electrodes. Also, depending on the dielectric properties of the particle and the surrounding medium, during the course of a measurement the test particle may change location as a result of dielectrophoretic forces associated with field inhomogeneity. It is demonstrated here that the accuracy and reproducibility of analyses of electrorotation spectra, especially if aided by computerized image analysis such as that developed for dielectrophoresis [16], can be significantly improved if the spatial variations of the magnitude and phase of the rotating field vector are taken into account.

4.2 Simulations

4.2.1 Static Electric Field.

The simulation model was developed using the Method of Moments [17], described in Chapter 2. This method has previously been used for calculations of fields generated by interdigitated, castellated electrodes designed for dielectrophoretic manipulation, the results of which have been given elsewhere [18]. In the simulations presented here, the total surface area of all the electrodes is divided into approximately 600 subareas. Therefore approximately 150 subareas were used per electrode for a four-electrode system such as that illustrated in figure 4.1. The results were determined across a regular matrix of 40 x 40 points arranged in a square, which could be placed at any point within or above the plane of the electrodes. This was located within the area defined by the electrode tips (illustrated by the thin dotted line on figure 4.1).

As described elsewhere [15] the geometry of the polynomial electrodes in the x-y plane is defined according to:

$$\left| x^2 - y^2 \right| = k^2 \tag{4.1}$$

where $2k$ defines the distance between opposing electrode tips. These electrodes are fabricated using standard photolithography, and in the simulations they were defined as being 0.2 μm thick with the spacing between electrode tips chosen to be 400 μm. The subareas s_i were chosen to be squares of sides 20 μm, and were uniformly distributed over the electrode surface to a distance of 200 μm back from the electrode tips. Four sinusoidal voltages (10V pk) were assigned to the electrodes, with 90° phase difference between adjacent electrodes. To simulate the sinusoidal voltages, the electrodes along the x-axis (at time t=0) were assigned phase values φ of zero on one electrode and 180° on the other, and those along the y-axis were assigned phase values of 90° and 270° (see figure 4.1). Thus, in concept at least, the field $\vec{E}$ acting in the space between the electrodes results from the superposition at a given instant in time t of two orthogonal linear field vectors and is given by:

$$\vec{E} = E_o \cos(\omega t)\vec{a}_x + E_o \cos(\omega t - \frac{\pi}{2})\vec{a}_y \tag{4.2}$$

where $\vec{a}_x$ and $\vec{a}_y$ are unit vectors along the x- and y-axes, respectively, and ω is the radian frequency of the applied voltages. Thus, the magnitude and phase of the rotating field at any instant are given by:

$$|\vec{E}| = E_o \; ; \quad \Theta = \omega t \tag{4.3}$$

Our simulations show (e.g. figures 4.4 & 4.5) that the magnitudes of $\vec{E}$ and Θ in fact vary significantly with position, so that the rotating field in the x-y plane takes the more general form:

$$\vec{E} = \vec{E}_x \cos(\omega t + \varphi_x)\vec{a}_x + \vec{E}_y \cos(\omega t + \varphi_y)\vec{a}_y \tag{4.4}$$

Because of the inherent symmetry of the electrode design of figure 4.1, only one-quarter of the total field distribution required simulation and for this 400 sample points were arranged in an area of 400μm x 400 μm. Cells used in electrorotation studies are typically of the order 6μm in diameter, and so the field calculations have been performed for a plane taken at 3μm above the upper surface of the electrodes.

4.2.2 Temporal Effects

The rotating field was simulated for one complete cycle of the voltage signals applied to the electrodes. This was achieved by determining the *static* electric field distribution at 10° intervals for one-half of a cycle and reversing these results to determine the second half of the cycle. These 18 calculations were performed using FORTRAN 77 on a Cray YMP supercomputer, and the results were then processed using MATLAB (The Math Works, Inc) to produce plots of the electrical potential in the plane of the electrodes as well as of the magnitude (E_x, E_y, E_z) and phase (φ_x, φ_y, φ_z) of the rotating field.

4.2.3 Torque and Dielectrophoretic Force

The magnitude of the steady-state electrorotation Ω (rad.s^{-1}) is limited by the viscous frictional drag acting on the particle according to:

$$\Omega = \frac{\Gamma}{R} \tag{4.5}$$

where R is the friction coefficient whose value depends on the viscosity of the surrounding medium and on the geometry and surface frictional properties of the particle. For the low rotational rates normally encountered, the Reynolds numbers are low and the viscous drag for ellipsoidal geometries can be readily obtained [10]. For simplicity we shall consider spherical particles of radius r, in which case the torque is usually [8-12] given as:

$$\Gamma = -4\pi\varepsilon_m \, r^3 \, \mathrm{Im}(f_{CM}) E_o^2 \tag{4.6}$$

where ε_m is the absolute relative permittivity of the suspending medium. The symbol Im means that the imaginary component of the Clausius-Mossotti factor f_{CM} is to be taken, and this factor is a function of the complex permittivities of the particle and suspending medium and can be generalised for the case of a heterogeneous particle exhibiting multiple dielectric dispersions [19]. Equation (4.6) has been derived for the case of an ideal rotating electric field which, as shown in equation (4.2), is composed of two equal field components phased 90^{o} apart. For the practical case where the rotating field is of the general form of equation (4.4) the torque vector is given by:

$$\vec{\Gamma} = -4\pi\varepsilon_m \, r^3 \, \mathrm{Im}\,(f_{CM}) E_x E_y \sin(\varphi_x - \varphi_y) \vec{a}_x \times \vec{a}_y . \tag{4.7}$$

From equations (4.6) and (4.7) we can define a field factor E_{eff}^2 as a measure of the uniformity of the rotational torque exerted on the particle as a function of its location:

$$E_{eff}^2 = E_x E_y \sin(\varphi_x - \varphi_y). \tag{4.8}$$

The importance of equations (4.7) and (4.8) are that they indicate that the rotating torque is not in general, as hitherto commonly assumed, proportional to the square of the field strength. Equation (4.6) is the special case for an ideal rotating field, which as we shall show exists over only a limited region between the electrodes.

Dielectrophoretic forces acting on the particle can indirectly influence the rotational torque by causing the particle to change its position during an electrorotational measurement. In some cases such forces can also result in the particle becoming immobilised at an electrode edge. The time-dependent dielectrophoretic force acting on the particle is [8-12]:

$$\vec{F}(t) = (\vec{m}(t) \cdot \nabla)\vec{E}(t) \tag{4.9}$$

and, in terms of the 36 simulations obtained at each 10° phase angle of a complete cycle of the applied electrode voltages, the time-averaged DEP force components are given by (taking F_x as an example):

$$F_x = \frac{1}{36}\sum_i (m_x(i)\frac{\partial E_x(i)}{\partial x} + m_y(i)\frac{\partial E_x(i)}{\partial y} + m_z(i)\frac{\partial E_x(i)}{\partial z}) \tag{4.10}$$

where i corresponds to each of the 36 instants in time, and $\vec{m}(i)$ is the related dipole moment induced in the particle. The components of $\vec{m}(i)$ in equation (4.10) can be readily determined [5, 20] so that, for example, the x-component of the dipole is given by

$$m_{xi} = 4\pi\varepsilon_m r^3 E_x[\mathrm{Re}(f_{CM})\cos(\phi_i + \varphi_x) - \mathrm{Im}(f_{CM})\cos(\phi_i + \varphi_x - \frac{\pi}{2})] \tag{4.11}$$

where ϕ_i corresponds to each one of the 36 phases (and corresponding instants in time) used for calculating the field distribution over one complete cycle, and $\mathrm{Re}(f_{CM})$ indicates that the real component of the Clausius-Mossotti factor f_{CM} is to be taken.

4.3 Results and Discussion

The potential distribution across the inter-electrode space is shown in figure 4.2 as a series of equipotentials spaced 1 volt apart (for 10V pk applied signals). The corresponding field vectors are normal to these equipotentials and of magnitude determined by the potential gradients. As the applied voltages progress through the first quarter of a cycle (in 30° steps) the field vectors shown in figure 4.3 progress in an anti-clockwise sense. However, only those field vectors located in the central region, corresponding to a circle of diameter around one-quarter of the inter-electrode gap, rotate in phase according to equation (4.4). The magnitudes of the rotating field vectors also vary according to their spatial coordinates, but of particular importance is the fact that the field vectors change their magnitudes as the potential cycle progresses. These effects are particularly noticeable in the regions near and between adjacent electrodes, where some of the field vectors vibrate and change polarity rather than rotate. Close inspection of figure 4.2 also reveals the fact that there are regions of field maxima near the electrodes which travel counter to the main rotating field. We consider that this effect is of relevance to understanding the so-called 'FUN' regime observed [20] in travelling field studies where particles close to electrodes appear to behave anomalously.

As indicated by equation (4.8), in order to determine the time-averaged torque across the inter-electrode space both the magnitude and phase of each field component have to be considered. These are summarized in figures 4.4-4.6, in which the spatial variations of the magnitudes and phases of each field component are plotted. To obtain the results for each individual location in space (represented by each elemental area in figs 4.4-4.6) the three principal (x-, y- and z-) components of the field were determined for each of the 36 simulations per applied voltage cycle. These were found, as expected, to be sinusoidal functions of time and from these functions the magnitude and phase of each field component could be calculated.

Inspection of figures 4.4-4.6, reveals the extent of the non-uniformity of the rotating field. For example, the x-component of the field (see figure 4.4(a)) has its largest values near the (x-axis) electrode edges, and minima at the y-axis electrode edges. As

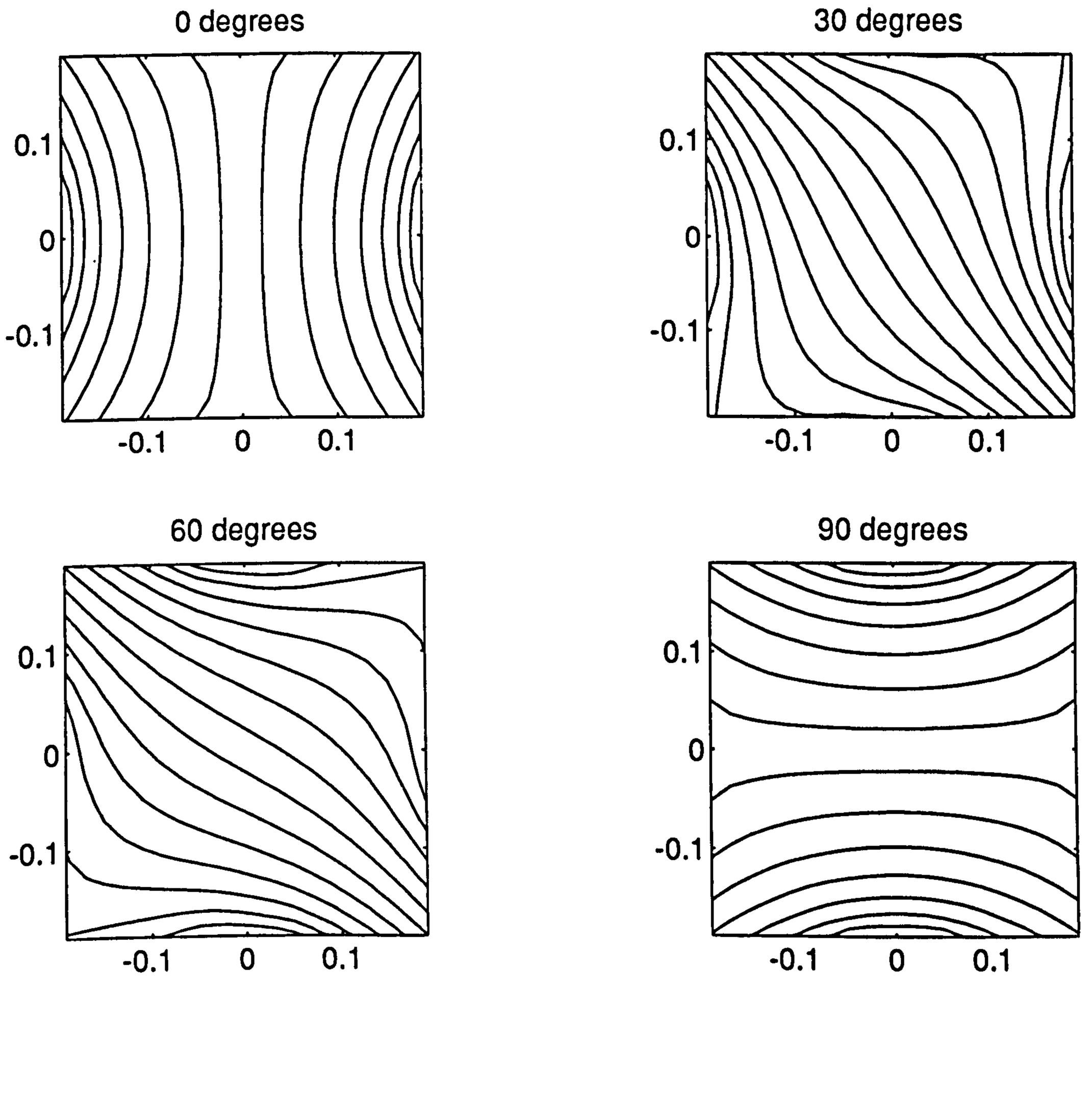

4.2 The equipotentials (spaced 1V apart) in the x-y plane of the inter-electrode space defined in figure 1 as the applied voltages progress through the first quarter of a cycle in 30^{o} degree steps. (i.e. ϕ_i of eqn. 4.11 = 0; $\pi/6$; $\pi/3$; $\pi/2$).

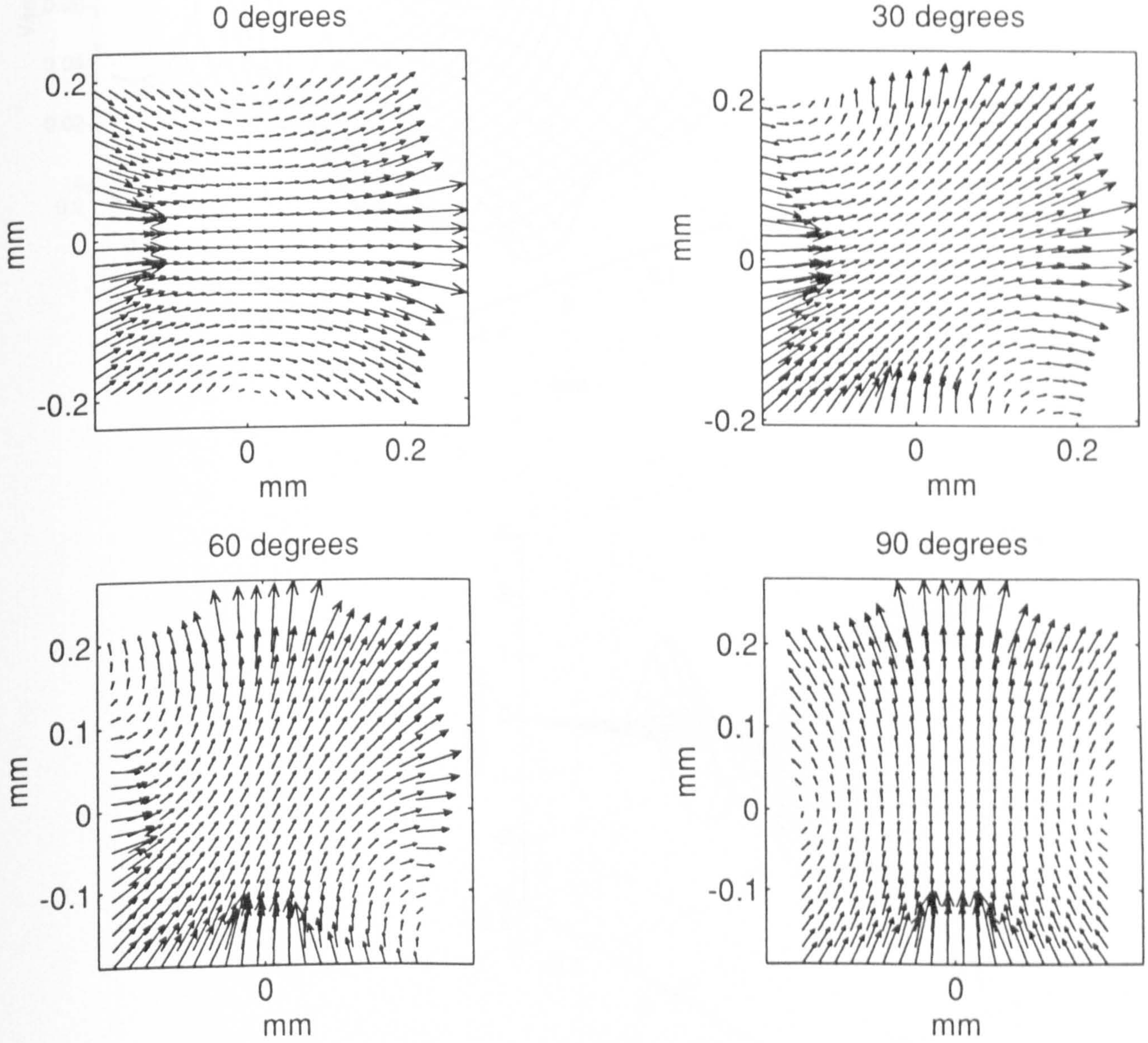

4.3 The electric field vectors (represented by an arrow whose base and length, respectively, define the vector location and magnitude, respectively) corresponding to the potential profiles shown in figure 4.2. The field vector $\vec{E}$ in the central region rotates in an anti-clockwise sense in synchrony with the voltage phases of figure 4.1.

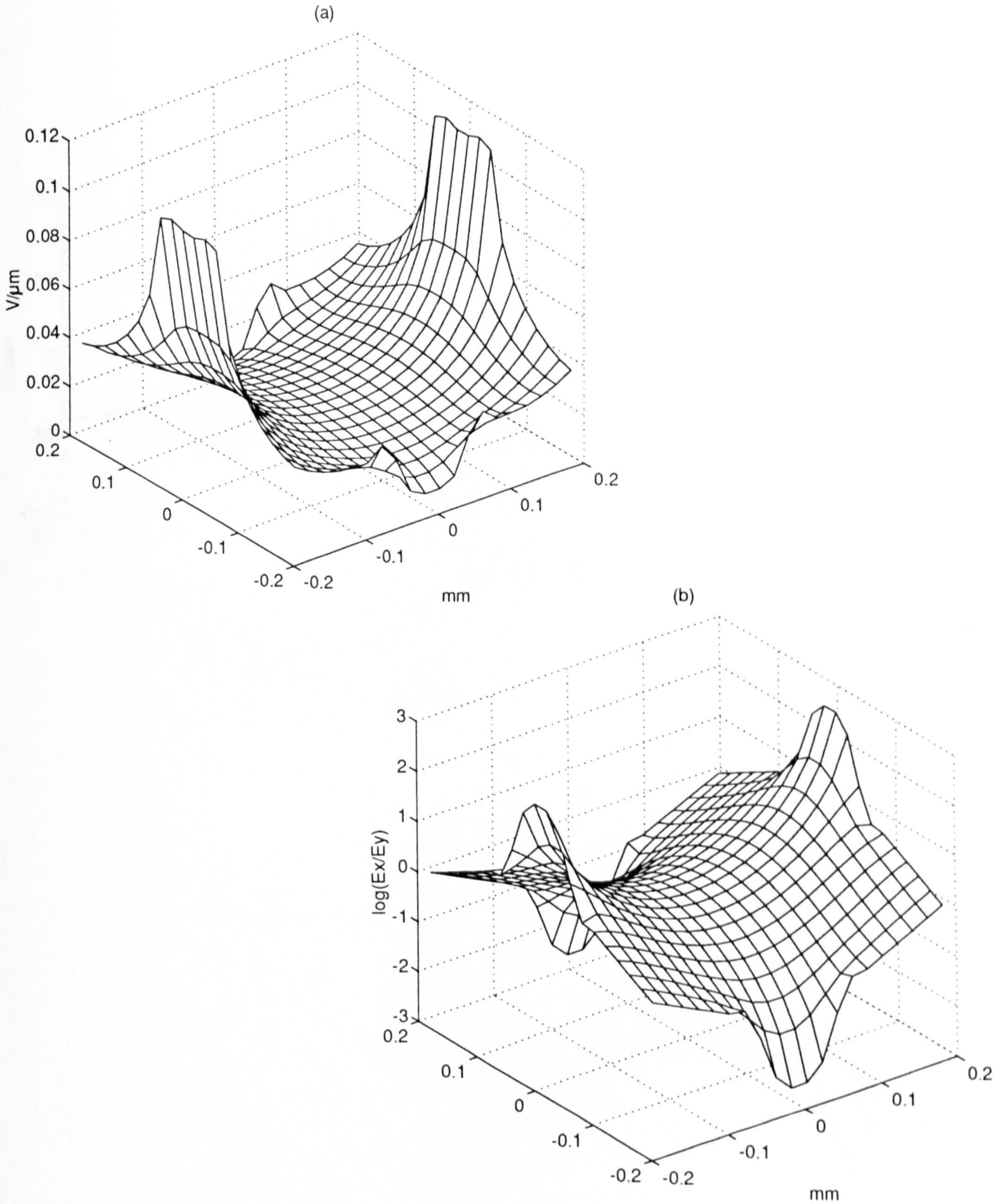

4.4 The spatial variation of (a) the x-component E_x ($V.\mu m^{-1}$), and (b) the logarithmic ratio of E_x and E_y, across the x-y plane defined in figure 4.1.

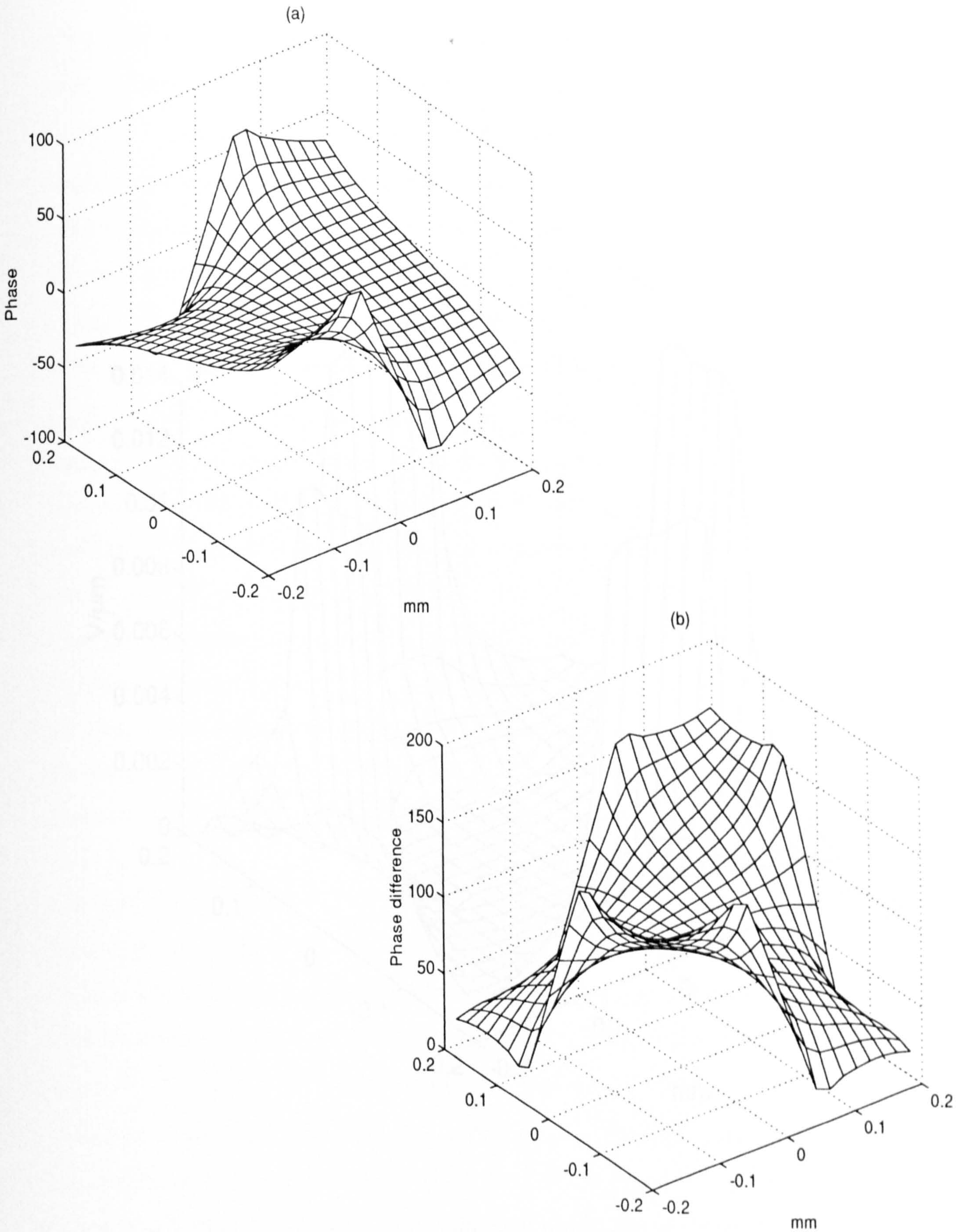

4.5 The spatial variation of (a) the phase φ_x of E_X, and (b) of the absolute difference between φ_x and φ_y (degrees).

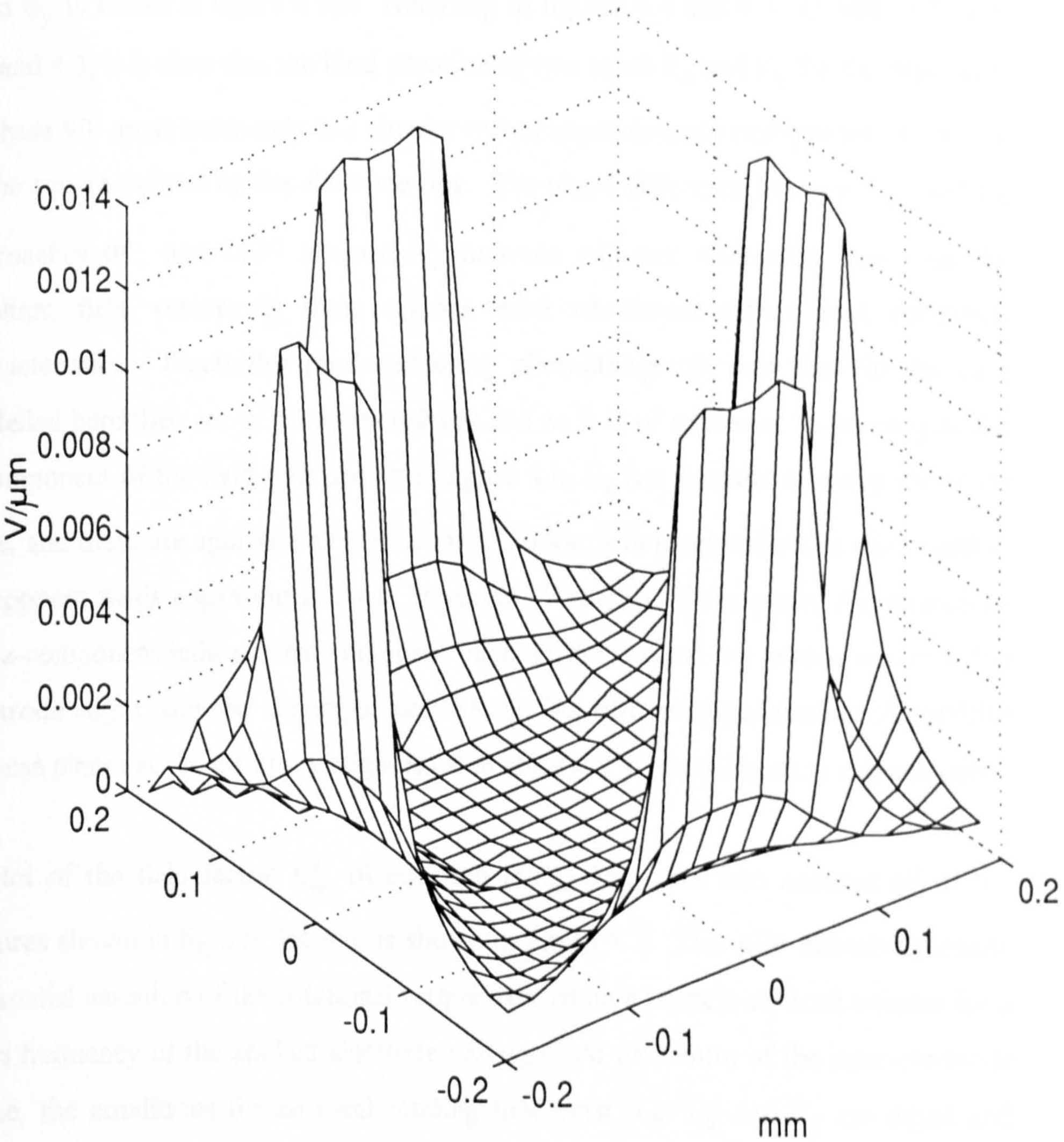

4.6 The spatial variation of the z-component E_z ($V.\mu m^{-1}$) of the electric field across the inter-electrode region defined in figure 4.1.

to be expected from the symmetry shown in figure 4.2, a corresponding behaviour exists for the y-component of the field. The extent to which E_y and E_x deviate from being equal is shown in figure 4.4(b) as a plot (log base 10) of the ratio of E_y to E_x. Also, as shown in figure 4.5(a), φ_x of equation (4.4) deviates from its ideal value of zero (and correspondingly φ_y deviates from 90^0) increasingly with distance from the central region between the electrodes. The spatial variation of the difference between φ $_x$ and φ_y is shown in figure 4.5(b). Referring to figures 4.4 and 4.5, as well to figures 4.2 and 4.3, it is clear that the ideal situation of two equal E_x and E_y field components of phase 90^0 apart holds only in a circular region approximately one quarter of the size of the square defined by the electrode tips. The phase difference between E_x and E_y approaches 0^o and 180^o alternatively between adjacent electrodes, and thus the resultant field vectors in these regions have vibrational rather than rotational characteristics. Electrodes produced using photolithography are thin (in the case modelled here they are of thickness 0.2μm) and so it is of relevance to investigate the z-component of the field. As shown in figure 4.6, E_z has maxima at every electrode edge, and these are approximately a factor of 10 lower in magnitude than the x- and y-component fields appearing at these locations. Analyses of the phase distribution of the z-component indicate that rotational fields in the z-x and z-y planes occur at the electrode edges, and this is compatible with the fact that rotational motion of particles in these planes at the electrode edges is often observed in electrorotation experiments.

A plot of the field factor E_{eff}^2 of equation (4.8), that takes into account all of the features shown in figures 4.4-4.6, is shown in figure 4.7. This plot effectively charts the spatial variation of the rotational torque exerted on a particle of fixed volume for a fixed frequency of the applied electrode voltages. At the centre of the inter-electrode space, the conditions for an ideal rotating field exist (i.e. E_x and E_y are equal and phased 90^o apart) and with increasing radial distance from the centre this ideal situation becomes progressively degraded. Thus, if a test particle changes location during measurement, or if two or more particles of non-equivalent locations are to be examined, then corrections should be made to their measured rotation rates if

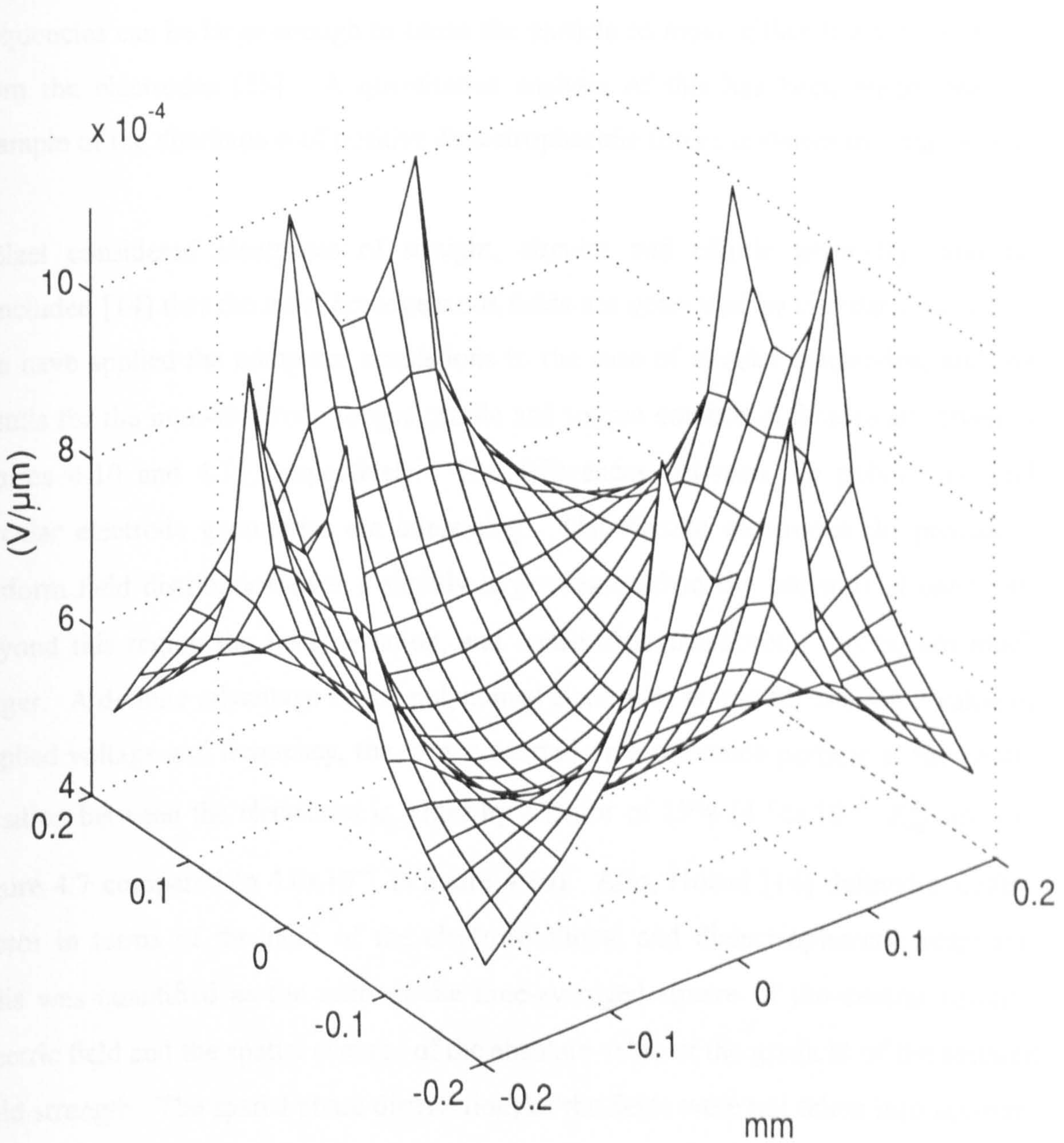

4.7 The spatial variation of the field factor E_{eff}^2 ($V^2.\mu m^{-2}$) of equation (4.8), and hence of the relative torque, for the polynomial electrodes of figure 4.1.

quantitative and reproducible analyses are to be made of their electrorotational behaviour. Figure 4.8 provides the correction factors that should be applied as a function of radial distance from the centre, either along the axes or along the diagonals of the square region defined in figure 4.2. Also, for measurements made within the central region, defined by a circle of radius equal to 0.6 of the distance between opposing electrode tips, the dielectrophoretic forces acting on the particle will be relatively small. Outside of this region, however, and depending on the dielectric properties of the particle and suspending medium, the dielectrophoretic force at some frequencies can be large enough to cause the particle to move either towards or away from the electrodes [15]. A quantitative analysis of this has been made, and an example of the distribution of positive dielectrophoretic forces is shown in figure 4.9.

Hölzel considered electrodes of straight, circular and elliptic geometry, and he concluded [14] that the most homogeneous fields are generated by circular electrodes. We have applied the computer simulations to the case of circular electrodes, and the results for the inter-electrode torque profile and torque correction factors are given in figures 4.10 and 4.11, respectively. The differences between the polynomial and circular electrode geometries are interesting. The circular electrodes do provide a uniform field distribution over a slightly larger region than the polynomial ones, but beyond this region the field deviation, and hence dielectrophoretic forces, are much larger. A definite advantage of the polynomial electrodes is that for the same value of applied voltage and frequency, the torque exerted on a reference particle at the centre position between the electrodes is larger by a factor of 19% (4.56×10^{-4} E_{eff}^2 units in figure 4.7 compared to 4.0×10^{-4} in figure 4.10). Also, Hölzel [14] defined a quality factor in terms of the ratio of the electrorotational and dielectrophoretic response. This was quantified as the ratio of the time-averaged square of the central rotating electric field and the spatial average of the absolute value of the gradient of the squared field strength. The spatial phase distributions of the fields were not taken into account, so that the form of the rotating field was assumed to be the ideal case described by equations (4.2) and (4.3), instead of the more general from of equation (4.4). Fortunately, the main objective of Hölzel's approach [14] as a method to optimize electrode geometries for electrorotation studies is not seriously affected, and in fact the

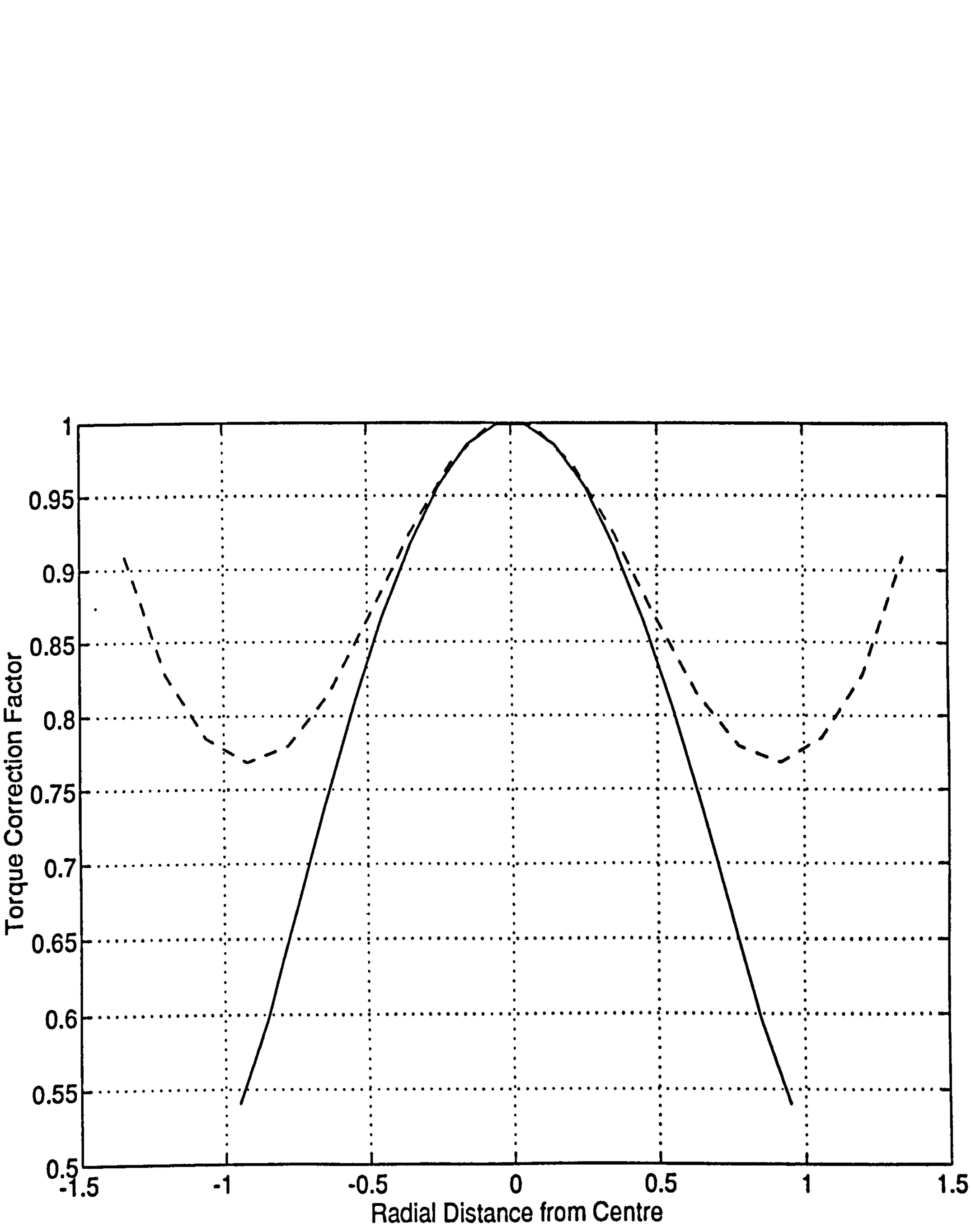

4.8 The normalised correction factor to be applied to the electrorotation rate for polynomial electrodes, as a function of the particle's normalised radial distance from the centre of the inter-electrode region defined in figure 4.1. — : along the x- and y-axes ; ---- : along the diagonals of the square region defined in fig. 4.1.

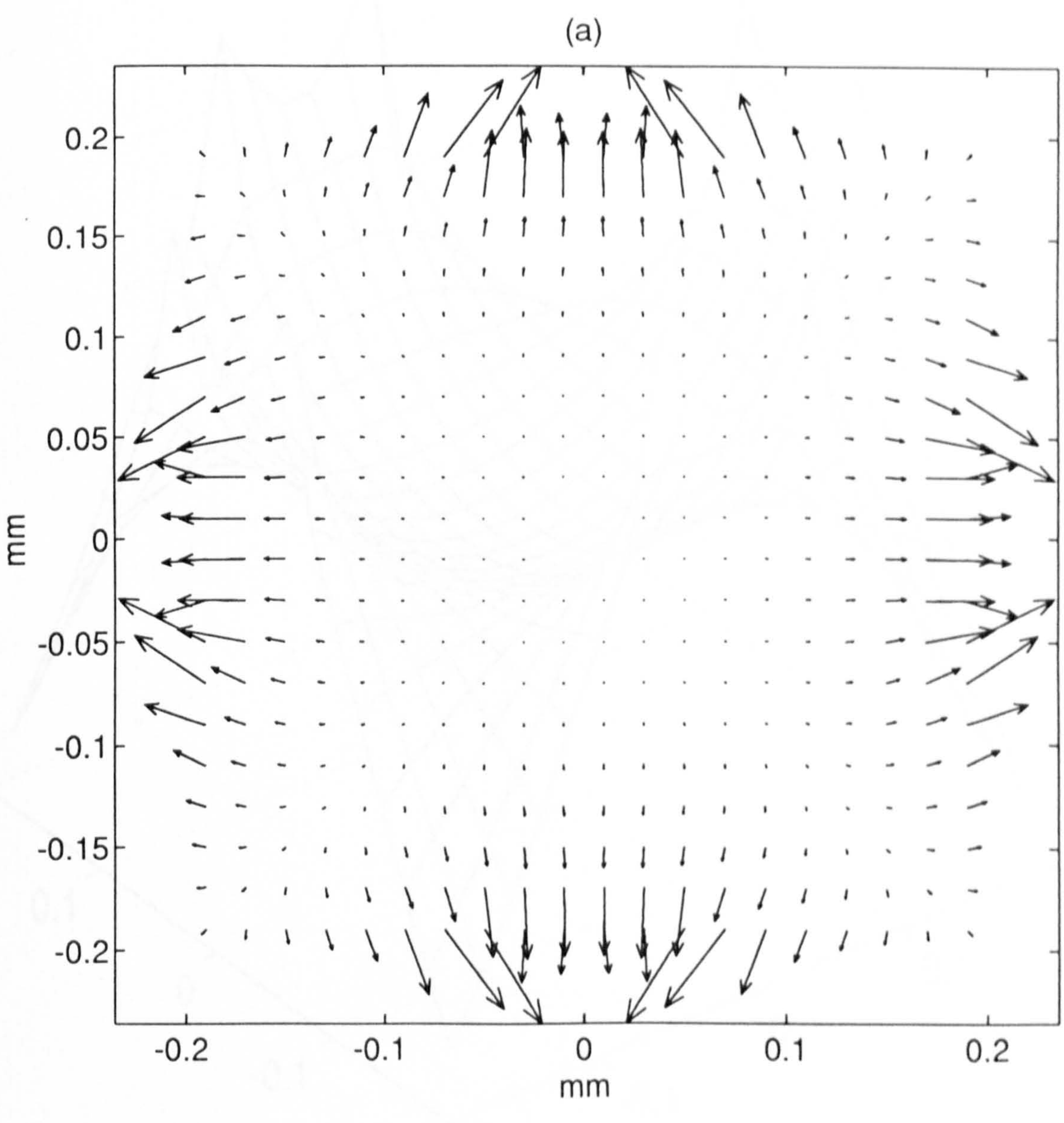

4.9 The distribution of positive dielectrophoretic forces, for polynomial electrodes of 200μm separation with 10V pk, applied voltages and simulated for viable yeast cells (of radius 3μm) at 1 MHz, where in equation (4.11) the factors Re(f_{CM}) and Im (f_{CM}) have values of 0.84 and 0.04, respectively [5].
force.

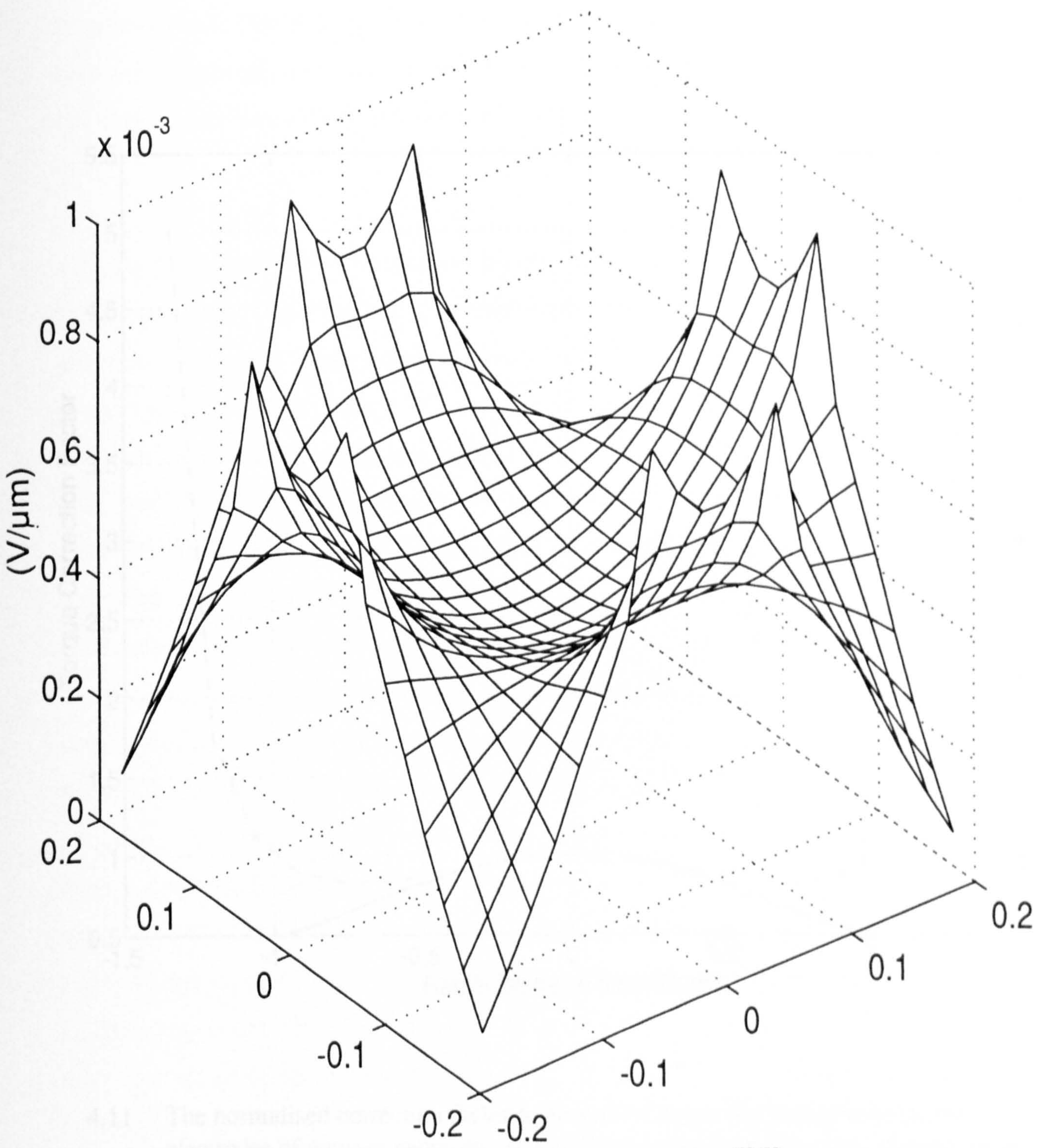

4.10 The spatial variation of the field factor E_{eff}^2 ($V^2.\mu m^{-2}$) of equation (4.8), and hence of the relative torque, for electrodes of circular geometry.

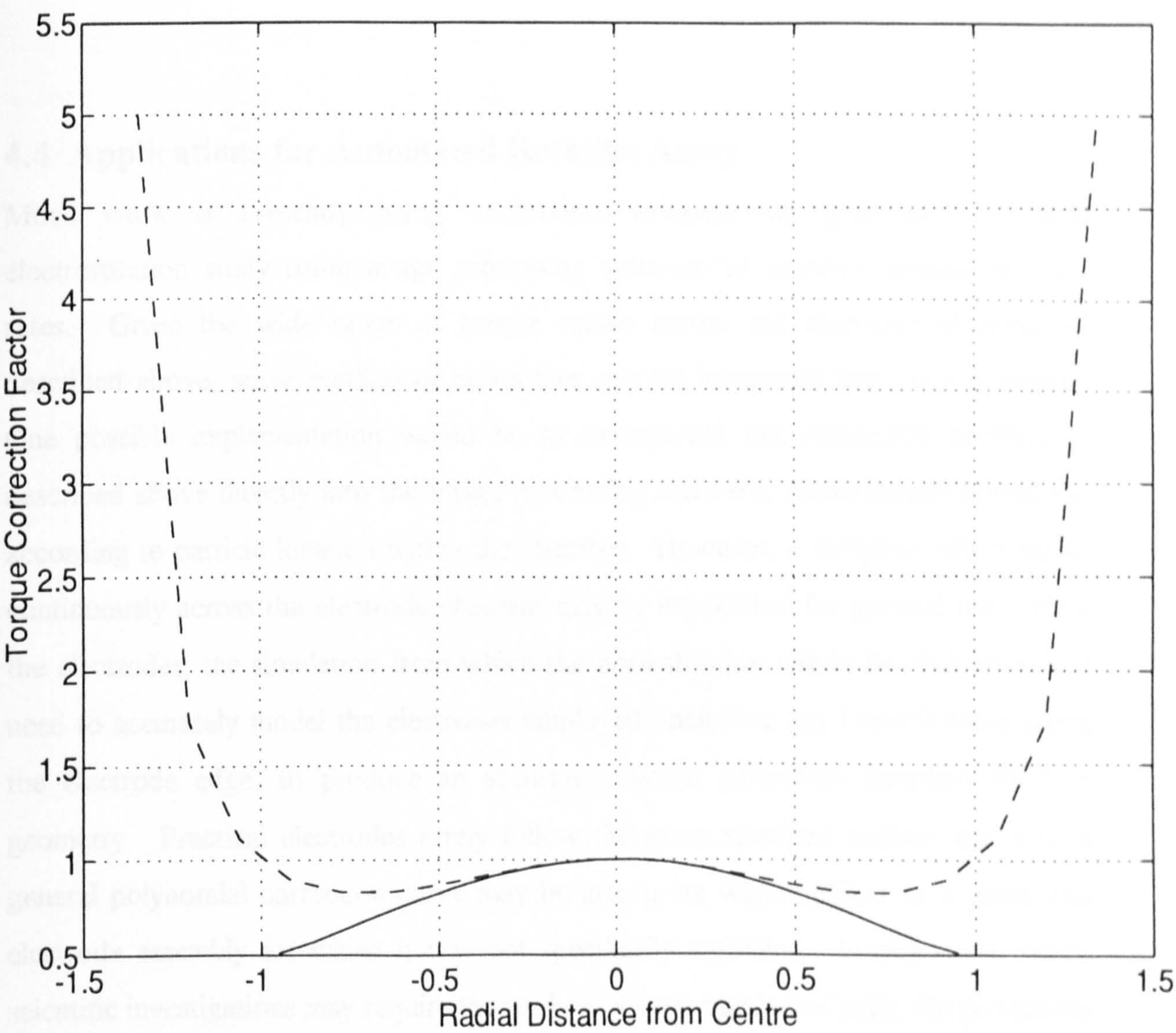

4.11 The normalised correction factor to be applied to the electrorotation rate for electrodes of circular geometry, as a function of the particle's radial distance from the centre of the inter-electrode region. — : along the x- and y-axes; ---- : along the diagonals of the square that fits between the electrode tips.

simplicity of his resistor network method has much to be recommended in this respect. However, as demonstrated in this present paper, to obtain torque correction factors as a function of the location of the test particle the spatial variations of *both* the magnitudes and phases of the field-components must be taken into account. This becomes increasingly important for particles which do not lie within the central inter-electrode region where the field is relatively homogeneous.

4.4 Applications for Automated Rotation Assay

Much work is presently being undertaken towards the goal of automated electrorotation study using image processing software to monitor particle rotation rates. Given the wide range of torque values across the electrode chamber as described above, some method of correction may be integrated into such a system. One possible implementation would be to incorporate the correction coefficients described above directly into the image processing software, automatically correcting according to particle location within the chamber. However, a template which varies continuously across the electrode chamber may be impractical for general use. Near the electrodes, the simulation from which the normalisation would be derived would need to accurately model the electrodes employed, including any imperfections along the electrode edge, to produce an accurate rotation correction template for that geometry. Practical electrodes rarely follow the exact specified outline, and thus a general polynomial correction curve may be inaccurate when applied to a given real electrode assembly for which it was not specifically modelled. Furthermore, whilst scientific investigations may require the study of a large number of cells, the processing facilities required to monitor and correct the rotation thoughout the chamber may be more than would be required for a simple assay system where only a few particles need be observed.

In place of a gradated system, a more viable alternative is to employ a masking system. A section of the rotation chamber, where the torque is known not to vary from within an arbitary percentage from the value at the centre of the chamber, could be studied whilst the remainder of the electrode chamber is "masked off" and not studied. As a

consequence a smaller section of the chamber is studied and less computing power is required. Such a mask would be more readily applicable to general use with real electrode structures, as the variation of torque near the centre of the electrode is less susceptible to small changes in electrode shape resulting from the manufacturing process.

Furthermore, the introduction of a mask system for a given electrode geometry allows a simple comparison of a variety of electrode geometries to be made in terms of the uniformity of torque across the central regions of the chamber. Previous studies of this nature [21] have considered only the instantaneous electric field, whereas the studies presented here also consider phase effects on torque distribution. The ideal geometry for electrorotation measurements would require a uniform torque across a large percentage of the electrode chamber, as well as consistently large torque values across this region to provide an easily-measured rotation rate. Using these criteria, a quality factor Q for the evaluation and comparison of different geometries may be defined as

$$Q=A\Gamma_c \tag{4.12}$$

where Γ_c is the torque at the centre of the electrode chamber, and A is the percentage continuous area of the electrode chamber where the torque is within an arbitrary limit of Γ_c. There are cases where the torque remains within the limit specified, but exceeds the limit in all other areas except for isolated areas near the corners of the electrode chamber. These areas are not included here in the calculation of area A, as they are unlikely to be used in austomated rotation; as they are near the electrode edges the values of torque are less likely to correspond with predicted values (as discussed above), and the irregular shape of these regions would be difficult to incorporate into a mask.

Ten different electrode geometries have been simulated using models similar to those described previously to investigate their suitability for rotation assay, as shown in figure 4.12. Many of these geometries have been employed practically by other workers [eg 1,14,15,21,22,23], whilst others are arbitrary shapes which were tested in

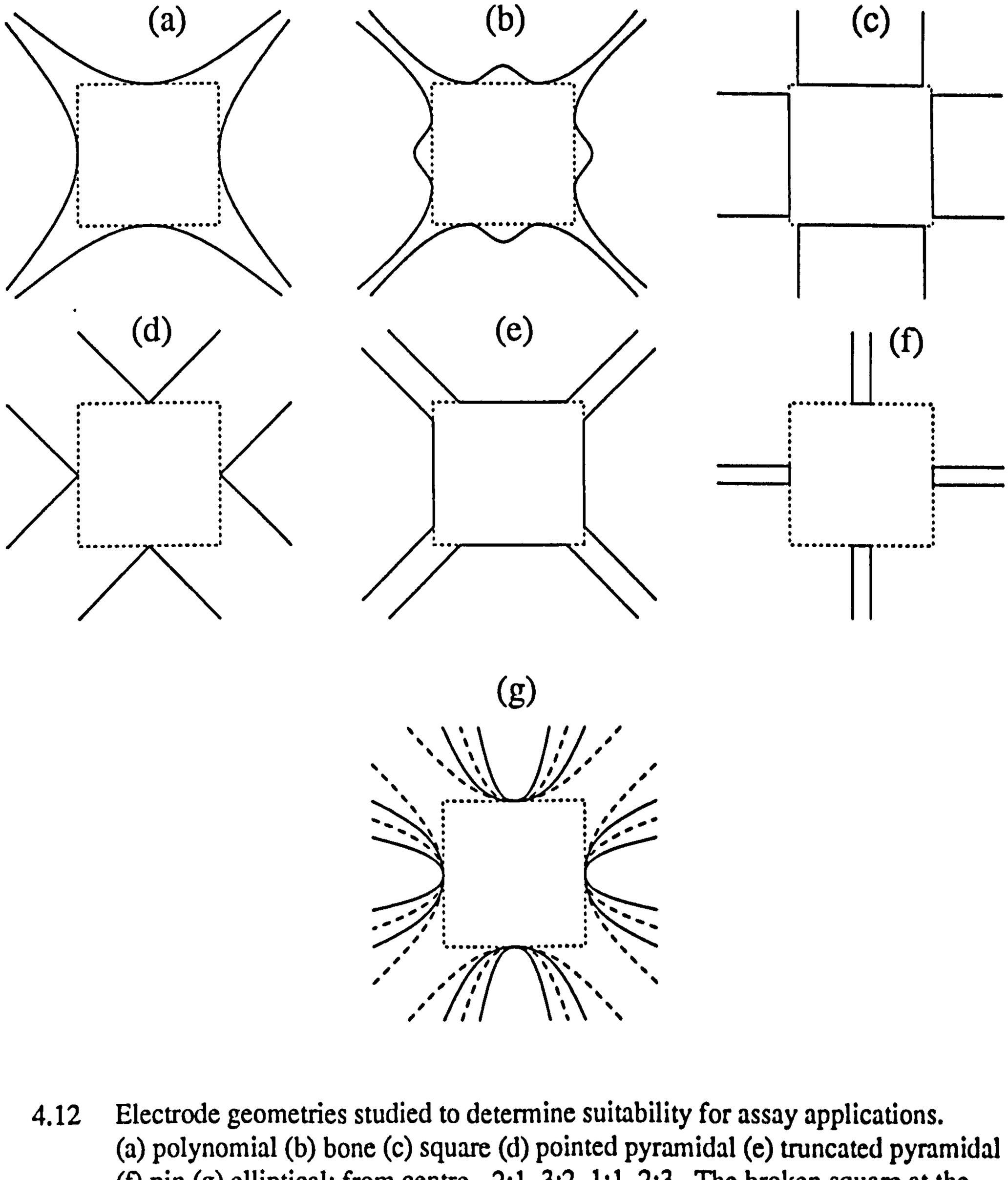

4.12 Electrode geometries studied to determine suitability for assay applications. (a) polynomial (b) bone (c) square (d) pointed pyramidal (e) truncated pyramidal (f) pin (g) elliptical: from centre - 2:1, 3:2, 1:1, 2:3. The broken square at the centre of the electrodes in each case is equivalent to the central area defined in Figure 4.1.

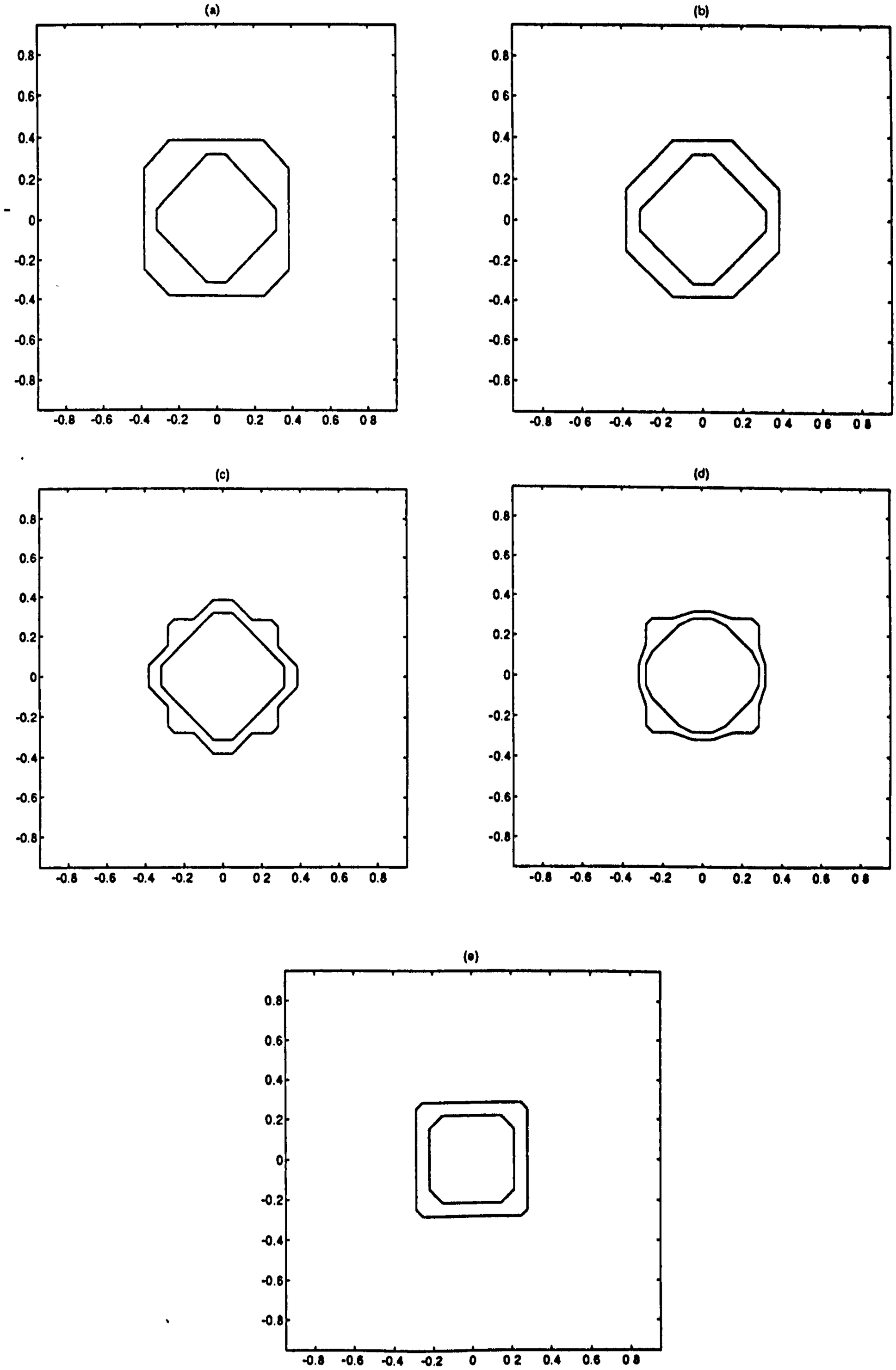

4.13 5% (inner boundary) and 10% (outer boundary) templates for the electrode configurations shown in Figure 4.12. (a) pointed pyramidal (b) polynomial, bone (c) truncated pyramidal, square, 1:1 (circular) and 2:3 ellipses (d) 2:1 and 3:2 ellipses (e) pin geometry.

Shape	Effective Torque at Chamber Centre Γ_c (E^2_{eff} units)	5% Torque Deviation		10% Torque Vatiation	
		A(%)	Q	A(%)	Q
Polynomial	4.56×10^{-4}	6	2.74×10^{-3}	13	5.93×10^{-3}
Bone	4.49×10^{-4}	6	2.69×10^{-3}	13	5.84×10^{-3}
Square	5.28×10^{-4}	6	3.7×10^{-3}	11	5.81×10^{-3}
Pointed pyramidal	2.69×10^{-4}	6	1.61×10^{-3}	15	4.04×10^{-3}
Truncated pyramidal	4.79×10^{-4}	6	2.87×10^{-3}	11	5.27×10^{-3}
Pin	5.30×10^{-5}	4	2.12×10^{-4}	8	4.24×10^{-4}
Ellipses					
2:1	1.97×10^{-4}	6	1.18×10^{-3}	9	1.77×10^{-3}
3:2	2.38×10^{-4}	6	1.43×10^{-3}	9	2.14×10^{-3}
1:1	4.00×10^{-4}	6	2.40×10^{-3}	11	4.4×10^{-3}
2:3	4.91×10^{-4}	6	2.95×10^{-3}	11	5.4×10^{-3}

Table 4.1 The results of a comparison of the suitability of the electrode geometries shown in figure 4.12 for electrode assay applications.

comparison with existing designs. The results of the simulation are presented in table 4.1, where values of Q are calculated for both 5% and 10% limits of deviation of torque from Γ_c. The areas within which the torque remains within these limits, from which masks may be developed for use in automated rotation assay, and are shown in figure 4.13.

As can be seen, for the 5% bound all electrode geometries save the pin geometry have similar values of A. For a 10% boundary, there is greater variation across the geometries. There is also a wide variation in values of Γ_c, with an order of magnitude separating the largest and smallest. Generally, the configurations with the higher electric fields and thus, the greater values of Γ_c, also generate widely non-uniform fields and thus the lower values of A. Hence the geometries with the greatest values of Q are those with values of A and Γ_c which are both above average, but not markedly so.

These results show that the electrode geometries which produce the greatest values of Q are the polynomial [15] and bone [21,22] geometries, both of which are employed in practical experimentation. Geometries where the sides of neighbouring electrodes were approximately parallel, such as the polynomial and bone type, plus the pointed and truncated pyramid geometries which were designed for this simulation, generate more uniform electric fields. Electrode structures where neighbouring electrodes are close to one another, such as the plate [23] and ploynomial geometries, generate higher electric fields and thus greater values of torque. It is the combination of both these factors, where electrodes are approximately parallel but approach each other at a relatively large distance from the electrorotation chamber itself, that gives geometries such as the bone and polynomial types their relatively superior performance. In contrast to these the pin geometry [1], often employed in experimentation due to its ease of construction, has a particularly poor value of Q owing to its small, non-uniform electic field, and it is thus impractical for rotation experimentation in comparison with all the other geometries presented here.

4.5 Conclusion

By computing the magnitude and phase of the electric field across the inter-electrode space and for 36 time-intervals in one A.C. cycle, it has been possible to simulate the time-average rotational torque and dielectrophoretic force effects produced by electrodes used in electrorotation studies. This provides, probably for the first time, a method for correcting the measured electrorotation rate of a test particle to take into account its position, and possible changes in position, relative to the optimum one at the centre of the inter-electrode space. This removes one of the dominant uncertainties present in electrorotation studies (the others being precise determinations of particle size, shape and viscous drag) and, as shown by the results of figures 4.7 and 4.10, the correction to be applied can be considerable if the particle lies outside or moves away from a region bounded by a circle of radius equal to 0.4 the distance between opposing electrodes. If computer-aided image analysis is used in the electrorotation measurements, then these results may be integrated into such a system. Implementation of such a system could either be by the application of torque correction factors, such as those presented in figures 4.8 and 4.11, or masking techniques where only small areas of uniform torque such as those shown in figure 4.13 are incorporated automatically into the protocol.

References

[1] Arnold W M and Zimmermann U 1982 *Z. Naturforsch.* **37c** 908-915

[2] Mischel M, Voss A and Pohl H A 1982 *J. Biol. Phys.* **10** 223-226

[3] Hu X, Arnold W M and Zimmermann U 1990 *Biochim. Biophys. Acta* **1021** 191-200

[4] Hölzel R, Lamprecht I and Mischel M 1991 *Physical Characterization of Biological Cells* ed W Schütt, H Klinkmann, I Lamprecht and T Wilson (Berlin: Verlag Gesundheit Gmbh) pp 273-294

[5] Huang Y, Hölzel R, Pethig, R and Wang X-B 1992 *Phys. Med. Biol.* **37** 1499-1517

[6] Arnold W M, Schwan H P and Zimmermann U 1987 *J. Phys. Chem.* **91** 5093-5098

[7] Beardsley T 1993 (July) *Scientific American* **269** 87

[8] Sauer F A and Schlögl R W 1985 *Interactions between Electromagnetic Fields and Cells* ed A Chiabrera *et al* (New York: Plenum) pp 203-251

[9] Fuhr G and Kuzmin P I 1986 *Biophys. J.* **50** 789-795

[10] Kakutani T, Shibatani S and Sugai M 1993 *Bioelectrochem. Bioenerg.* **31** 131-145

[11] Pastushenko V Ph, Kuzmin P I and Chizmadzhev Yu A 1985 *Stud. Biophys.* **110** 51-57

[12] Wang X-B, Huang Y, Hölzel R, Burt P H and Pethig, R 1993 *J. Phys. D: Appl. Phys* **26** 312-322

[13] Hölzel R 1993 *IEEE Trans. Instrum. Meas.* **42** 758-760

[14] Hölzel R 1993 *J. Phys. D: Appl. Phys* **26** 2112-2116

[15] Huang Y and Pethig R 1991 *Meas. Sci. Technol.* **2** 1142-1146

[16] Gascoyne P R C, Huang Y, Pethig R, Vykoukal J and F F Becker 1992 *Meas. Sci. Technol.* **3** 439-445

[17] Birtles A B, Mayo B J and Bennett A W 1973 *Proc. IEE* **120** 213-220

[18] Wang X-B, Huang Y, Burt J P H, Markx G H and Pethig R 1993 *J. Phys. D: Appl. Phys* **26** 1278-1285

[19] Wang X-B, Pethig R and Jones T B 1992 *J. Phys. D: Appl. Phys* **25** 905-912

[20] Huang Y, Wang X-B, Tame J A and Pethig R 1993 *J. Phys. D: Appl. Phys* **26** 1528-1535

[21] Gimsa J, Glaser R and Fuhr G 1988 *Studia Biophysica* **125** 71-76

[22] Burt JPH, Pethig R, Hughes MP, Kerslake JP, Parton A and Dawson D 1995 *Proc. 9th Int Conference on Electrostatics*

[23] Fuhr G, Hagedorn R, Göring H 1984 *Studia Biophysica* **102** 221-227

Chapter 5

Dielectrophoretic Forces on Particles in Travelling Electric Fields

5.1 Introduction

Masuda *et al* [1, 2] were the first to demonstrate that travelling electric fields could be used to induce controlled translational motion of bioparticles (red blood cells and lycopodium particles). The travelling fields were generated by applying three-phase voltages, of frequency ranging from 0.1 Hz to 100 Hz, to a series of bar-shaped electrodes. At these low frequencies the dominant translational forces acting on the bioparticles were electrophoretic in origin, and Masuda *et al* [1, 2] proposed that such travelling fields could eventually find application in the separation of particles according to their size or electrical charge. Travelling fields of frequency between 10 kHz and 30 MHz were later shown by Fuhr and co-workers [3, 4] to be capable of imparting linear motion on pollen and cellulose particles, and Huang *et al* [5] have shown that travelling fields of frequency between 1 kHz and 10 MHz can be used to manipulate yeast cells and to selectively separate them when they are mixed with bacteria. For frequencies above 1kHz the dielectric, rather than surface charge properties of the particles, determine their responses to imposed A.C. fields, and particle separation according to differences in either their dielectric properties or their size is in principle possible through careful choice of the electrode dimensions and design [5].

The electrode geometry employed [3-5] for producing travelling electric fields took the form of the design shown in figure 5.1, and from theoretical considerations a travelling field was *assumed* to be established over the electrodes and in the channel between them by applying sinusoidal voltages having phase sequences as shown in this figure. Depending on the frequency of the applied voltages and on the conductivity of the

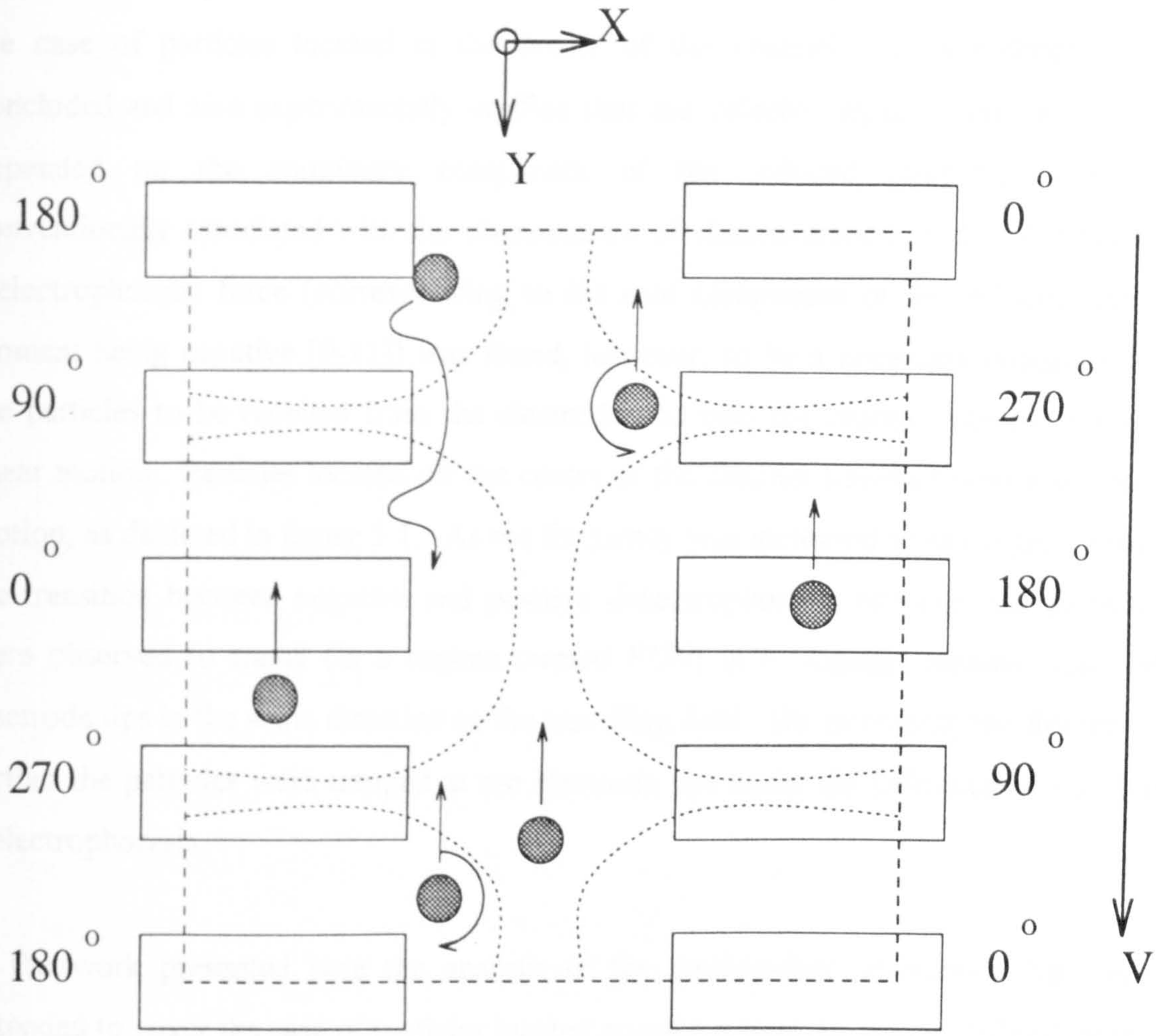

5.1 The basic electrode geometry, which when addressed with voltages of phase sequences shown, establishes a travelling electric wave of propagation direction indicated by the arrow V. The square area indicates the region over which the simulations were performed, and the dotted equipotentials are included to aid comparison with figure 5.2. When experiencing travelling field motion, particles move over the electrodes or along the channel in the direction opposing that of the travelling wave. In the *FUN* regime, particles travel in a "zigzag" manner in the same direction as the travelling wave.

suspending medium, particles were observed [5] to move along the centre of the channel in the direction *opposing* that of the travelling potential wave (see figure 5.1). The theoretical analysis [5] of this effect, in terms of the interaction of the travelling wave with the dipole moment induced in the particle, was simplified by restricting it to the case of particles located in the centre of the channel. It was theoretically concluded and also experimentally verified that the velocity imparted on the particle depended on the *imaginary* component of the induced moment, which is conventionally associated with the phenomenon of electrorotation [6-8]. A negative dielectrophoretic force (corresponding to the *real* component of the induced dipole moment being negative [9-11]) was found, however, to be a necessary condition for the particles to be repelled from the electrode tips into the channel and to undergo linear motion. Particles located off the centre of the channel travelled with a spinning motion, as depicted in figure 5.1. As the frequency was increased to the region where the transition between negative and positive dielectrophoresis occured, the particles were observed to travel (in a regime termed *FUN*) in a "zigzag" manner near the electrode tips in the same direction as the travelling field. On increasing the frequency further the particles were trapped at the electrode tips under the influence of positive dielectrophoresis.

In the work presented here the analysis of the particle-field interaction has been extended to cover the case of particles located anywhere over the region defined by the electrodes and channel, and not just to the case for those located in the centre of the channel. The results obtained reveal new phenomena associated with travelling electric field effects, and provide insights into possible practical applications for particle characterisation and selective separation.

5.2 Simulations

5.2.1 Procedure

The computer simulations of the travelling fields were obtained using the Method of Moments [12] described in Chapter 2. The model used is similar to the one described in Chapter 4, used to determine the fields used to manipulate particles by electrorotation. Thus, the surface charge density distribution on the electrodes, approximated by charge density values on a number of small subareas, were derived from the known applied electrode potentials and the charge-potential relationship matrix [13, 14]. This enabled the potentials and electric field vectors at any location in the electrode system to be determined.

The principal electrode geometry (figure 5.1) was chosen to be the same as in the previous work [5], in which nine pairs of electrodes (each of length 30μm, width 10μm, and spaced 10μm apart) are located on either side of a channel of width 30μm. The electrode thickness was assumed to be 0.2 μm, typical of the electrodes fabricated using standard photolithography. To avoid complications of the field distribution arising from fringing effects at the ends of the channel and at the outer electrode boundaries, detailed analyses were confined to a square area 80μm x 80μm (see figure 5.1) encompassing the five central electrodes. Each electrode surface in this region was divided into 110 subareas, with the elemental areas on the upper surfaces being square of side 2μm, whilst vertical electrode edges were divided into rectangular elements of sides 2μm x 0.1μm. Sinusoidal signals of peak magnitude 10 volts and of phase sequences shown in figure 1 were applied to the electrodes. Sample X-Y planes, 3μm and 10μm above the electrode surface, were chosen to cover the situations where yeast cells (average radius 3μm) reside on the electrodes or are slightly levitated above them [5]. A total of 1024 potential sampling points (in the form of a 32 x 32 matrix) were arranged to be 2.5μm apart. A vertical plane (Y-Z) through the electrodes was also analysed to a higher resolution corresponding to the potential sample points being spaced 1.0μm apart. The electrode and channel widths in figure 5.1 were also altered to ascertain their controlling influence on the overall travelling field distributions.

5.2.2 Dynamic Field Simulation

The instantaneous electric field distribution generated by the electrode array was simulated for one complete cycle of a travelling wave. This was accomplished by advancing the signal phases at 10^{o} intervals and determining the electric potential profiles at each instant. These 36 simulations were then arranged, using MATLAB (The Math Works, Inc), into a matrix whose three dimensions were the two spatial coordinates over the square plane studied plus that of time. Arranged in this form, the data could be analysed either in terms of temporal variations of the electric potential and field at any coordinate, or in the form of extended 2D or 3D animations that could be stored on video and viewed in real time.

It was found that all three field components at any point of the electrode system follow sinusoidal temporal varations and the field $\vec{E}$ took the form,

$$\begin{aligned}\vec{E}(t) &= E_x(t)\vec{a}_x + E_y(t)\vec{a}_y + E_z(t)\vec{a}_z \\ &= \sum_{\alpha=x;y;z} E_{\alpha 0}(x,y,z)\cos\{\omega t + \varphi_\alpha(x,y,z)\}\vec{a}_\alpha\end{aligned} \tag{5.1}$$

where $\vec{a}_x$, $\vec{a}_y$ and $\vec{a}_z$ are unit vectors along the x-, y- and z-axes, respectively and ω is the angular frequency of the voltages applied to the electrodes. $E_{\alpha 0}$ and φ_α (α=x;y;z) are the magnitude and the phase of each field component, respectively, which were determined using an error minimisation procedure from the field temporal variations.

5.2.3 Force Calculations

The induced dipole moment $\vec{m}(t)$ for a particle subjected to the field with three spatial components is given by,

$$\vec{m}(t) = m_x(t)\vec{a}_x + m_y(t)\vec{a}_y + m_z(t)\vec{a}_z. \tag{5.2}$$

Following Huang *et al* [5] and taking $m_x(t)$ as an example, the components of the dipole moment take the form,

$$m_x(t) = 4\pi\ \varepsilon_m\ r^3 \left\{\cos(\omega t + \varphi_x)\ \mathrm{Re}[f_{CM}] - \sin(\omega t + \varphi_x)\ \mathrm{Im}[f_{CM}]\right\} E_{x0} \qquad (5.3)$$

where r is the radius of the particle and ε_m is the absolute permittivity of the suspending medium. The terms Re and Im in equation (5.3) refer to the real and imaginary components, respectively, of the Clausius-Mossotti factor f_{CM} defined by:

$$f_{CM} = \frac{\varepsilon_p^* - \varepsilon_m^*}{\varepsilon_p^* + 2\varepsilon_m^*} \qquad (5.4)$$

in which ε_p^* and ε_m^* are the particle and suspending medium complex permittivities, respectively, defined by $\varepsilon^* = \varepsilon - j(\sigma/\omega)$ with ε the permittivity, σ the conductivity and $j=\sqrt{-1}$. The time-dependent dielectrophoretic force acting on the particle is given [5, 8, 10] by:

$$\begin{aligned}\vec{F}(t) &= (\vec{m}(t)\cdot\nabla)\vec{E}(t) \\ &= F_x(t)\vec{a}_x + F_y(t)\vec{a}_y + F_z(t)\vec{a}_z\end{aligned} \qquad (5.5)$$

where the force components (taking $F_x(t)$ as an example) are given by:

$$F_x(t) = m_x(t)\frac{\partial E_x(t)}{\partial x} + m_y(t)\frac{\partial E_x(t)}{\partial y} + m_z(t)\frac{\partial E_x(t)}{\partial z}. \qquad (5.6)$$

In our simulation the DEP force was time-averaged for the 36 simulations obtained at each 10^o phase angle of a complete cycle of the applied electrode voltages, given by (α=x; y; z):

$$F_\alpha = \frac{1}{36}\sum_i \left(m_x(i)\frac{\partial E_\alpha(i)}{\partial x} + m_y(i)\frac{\partial E_\alpha(i)}{\partial y} + m_z(i)\frac{\partial E_\alpha(i)}{\partial z}\right) \qquad (5.7)$$

where i corresponds to each of the 36 instants in time, and $\vec{m}(i)$ is the related dipole moment induced in the particle, given at each instant by equations (5.2-5.3).

5.3 Results and Discussion

5.3.1 Electric Field Distributions

Using a facility provided by MATLAB 4 (The Mathworks, Inc), the field distributions for each 10° phase angle were sequentially displayed in order through full 360° cycles to produce an animated motion picture. By this means the key features of the potential and field distributions became evident. For example, the instantaneous field minima are found to occur in the central region of the channel and travel synchronously with the voltage signals applied to the electrodes. Also, in a plane 3μm above the electrodes the field maxima occur near the electrode tips and over the electrode surfaces, and move discontinuously in the opposite direction to that of the applied voltage waves. These two effects are evident in a plot of the equipotentials (figure 5.2) as the voltage signals on the electrodes are advanced at 30° intervals through a quarter cycle. Furthermore, as will be described in more detail, the behaviour of the travelling field above the electrodes is dependent on the height above the electrode plane.

The field features were further examined by plotting each field component as a function of time at the point of interest. This revealed that everywhere the three orthogonal field components $E_x(t)$, $E_y(t)$ and $E_z(t)$ vary sinusoidally with time. The spatial variations of the magnitude and phase for each field component in a plane 3μm above the electrodes are shown in figure 5.3. At the centre of the channel, within limits approaching not less than around 5μm from the electrode tips, the field is dominated by its $\vec{a}_x$-component and the other two components ($\vec{a}_y$, $\vec{a}_z$) are very small (figure 5.3(a, c, e)). The linear variation of the phase φ_x (figure 5.3(b)) in the channel region agrees well with the expression:

$$E_x(x,y,t) = A(x)\cos(\omega t - 2\pi y/\lambda)\vec{a}_x \tag{5.8}$$

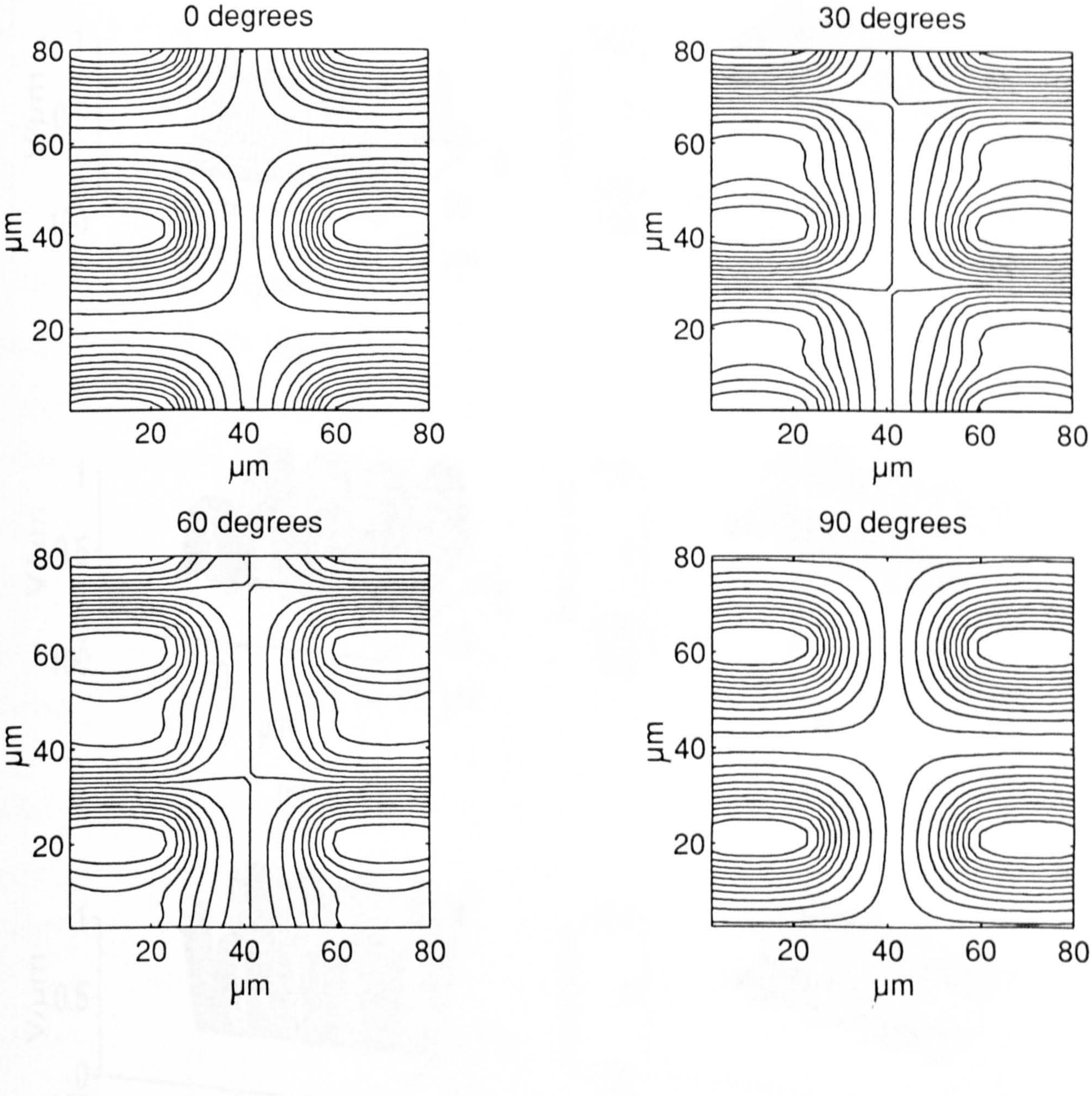

5.2 The equipotentials in the x-y plane, located 3μm above the electrode surfaces defined in Figure 5.1, that are generated as a sinusoidal voltage applied to the electrodes is progressed in 30° steps for a quarter of a cycle. A continuous animation of such plots through several cycles reveals that the field minima at the centre of the channel travel in synchrony with the applied travelling potential wave, whereas the field maxima at the electrode edges travel in the opposite direction (ie against the arrow V of figure 5.1).

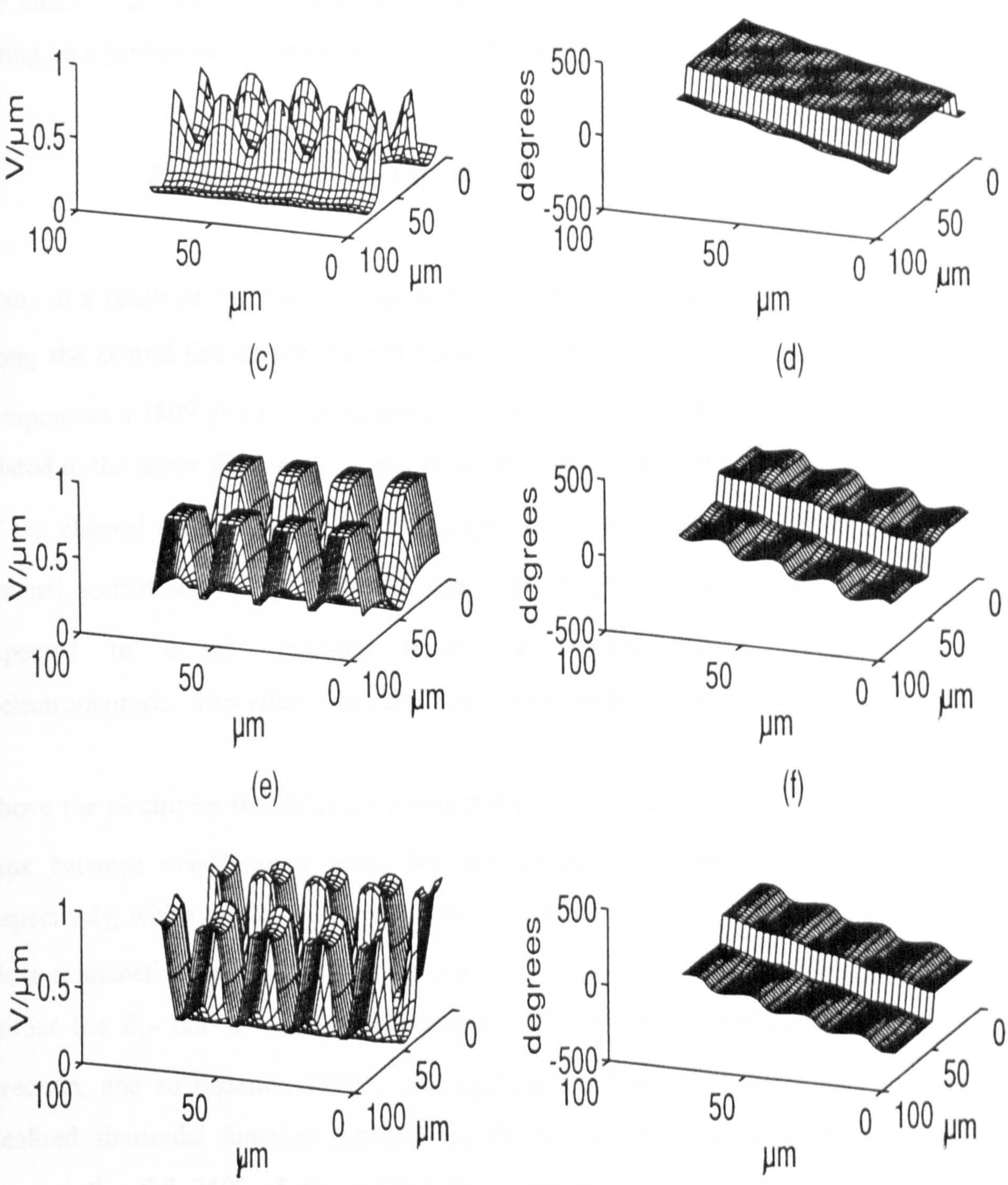

5.3 The magnitude (a, c, e) and phase (b, d, f) distributions of the x-, y- and z-components of the electric field generated in the X-Y plane 3µm above the electrodes defined in Figure 5.1.

proposed by Huang *et al* [5], where the wavelength λ of the travelling field is equal to the repetitive distance between electrodes of the same phase (80μm for the electrodes and phase sequence shown in figure 5.1). This indicates that a near-ideal travelling field, propagating in the same direction as the applied potential wave, is established in the channel, and confirms the earlier conclusion [5] that the travelling wave force acting on a particle at the centre of the channel is given by:

$$F(\omega) = -\frac{4\pi\varepsilon_m r^3}{\lambda}\mathrm{Im}[f_{CM}]E^2 \qquad (5.9)$$

Also, as a result of the electrode symmetry, the phase for the $\vec{a}_x$- field is mirrored along the central line of the channel (figure 5.3(b)), whilst for the other two field components a 180° phase jump occurs (figure 5.3(d, f)). The effective rotating field is related to the factor $E_x E_y \sin(\varphi_x - \varphi_y)$ [14]. Since φ_x is symmetrical about the centre of the channel (Figure 5.3(b)) and φ_y steps up by 180° (figure 5.3(d)) across the channel, so that $\sin(\varphi_x - \varphi_y)$ changes sign, cells on opposite sides of the channel are expected to exhibit opposing senses of rotation during travelling-wave dielectrophoresis. This effect was observed experimentally in earlier work [5].

Above the electrodes the fields are dominated by the $\vec{a}_y$- and $\vec{a}_z$- components, at the gaps between neighbouring electrodes and directly over the electrode surfaces respectively, whilst the $\vec{a}_x$- field component is of small magnitude (figure 5.3(a, c, e)). Close examination of the phase distribution for these regions shows that the phases for neither the $\vec{a}_y$- nor $\vec{a}_z$- component exhibit a monotonic dependence along the y-direction, and so equation (5.9) is not applicable. This phase distortion from an idealised sinusoidal function results from the electrodes being of finite size, and because the full 360° of the applied sinusoidal potential is quantised into four components in quadrature, rather than being a continuous function. This effect, coupled with the magnitude variations of the field components, results in the field maxima travelling discontinuously above the electrode regions, and in an opposite

sense to that of the field at the centre of the channel. The animated sequences of the field-time variations also reveal these features.

5.3.2 Dielectrophoretic Force

Equations (5.2-5.7) used to model the dielectrophoretic force acting on a particle in an AC electric field show that this force is given by the real and imaginary components of the Clausius-Mossotti factor f_{CM} (equation (5.4)). The results obtained in the computer simulations are shown in figure 4 and can be summarised as follows:

(i) $\mathrm{Re}[f_{CM}] >> |\,\mathrm{Im}[f_{CM}]\,|$; $\mathrm{Re}[f_{CM}] > 0$. The force vectors in figure 5.4(a) always point towards strong field regions at the electrode edges, an effect which is the same as conventional positive dielectrophoresis [10,11] and depends on the non-uniformity of the electric field. Further, it is found that the magnitudes of the force vectors are proportional to $\mathrm{Re}[f_{CM}]$. Reversing the polarity of $\mathrm{Re}[f_{CM}]$ results in the force vectors reversing so as to be directed towards weak field regions, away from the electrode edges and towards the channel and the gaps between the electrodes. The dielectrophoretic force is thus proportional to both the real part of the Clausius-Mossotti factor and to the gradient of the field strength. Because the particles can be immobilised at *either* strong or weak field regions, the dielectrophoretic force can be termed a *trapping force*.

(ii) $\mathrm{Im}[f_{CM}] >> |\mathrm{Re}[f_{CM}]\,|$; $\mathrm{Im}[f_{CM}] > 0$. In the channel and the regions located more than 5 μm above the electrodes the force vectors are directed in the $\vec{a}_y$-direction opposing that of the travelling field. For these cases the translational force acting on the particle is of the form of equation (5.9). However, in the plane 3 μm above the electrode surfaces, and as a consequence of the phase distortions from an idealised sinusoidal waveform, the force vectors act in the same direction as the applied travelling wave, as shown in figure 5.4(b). Changing the polarity of $\mathrm{Im}[f_{CM}]$ results in a reversal of the force vectors. Furthermore, the simulations indicate that the magnitudes of the force vectors are proportional to $\mathrm{Im}[f_{CM}]$. This $\mathrm{Im}[f_{CM}]$ dependent force term depends on the non-uniform distribution of the phase values for each field

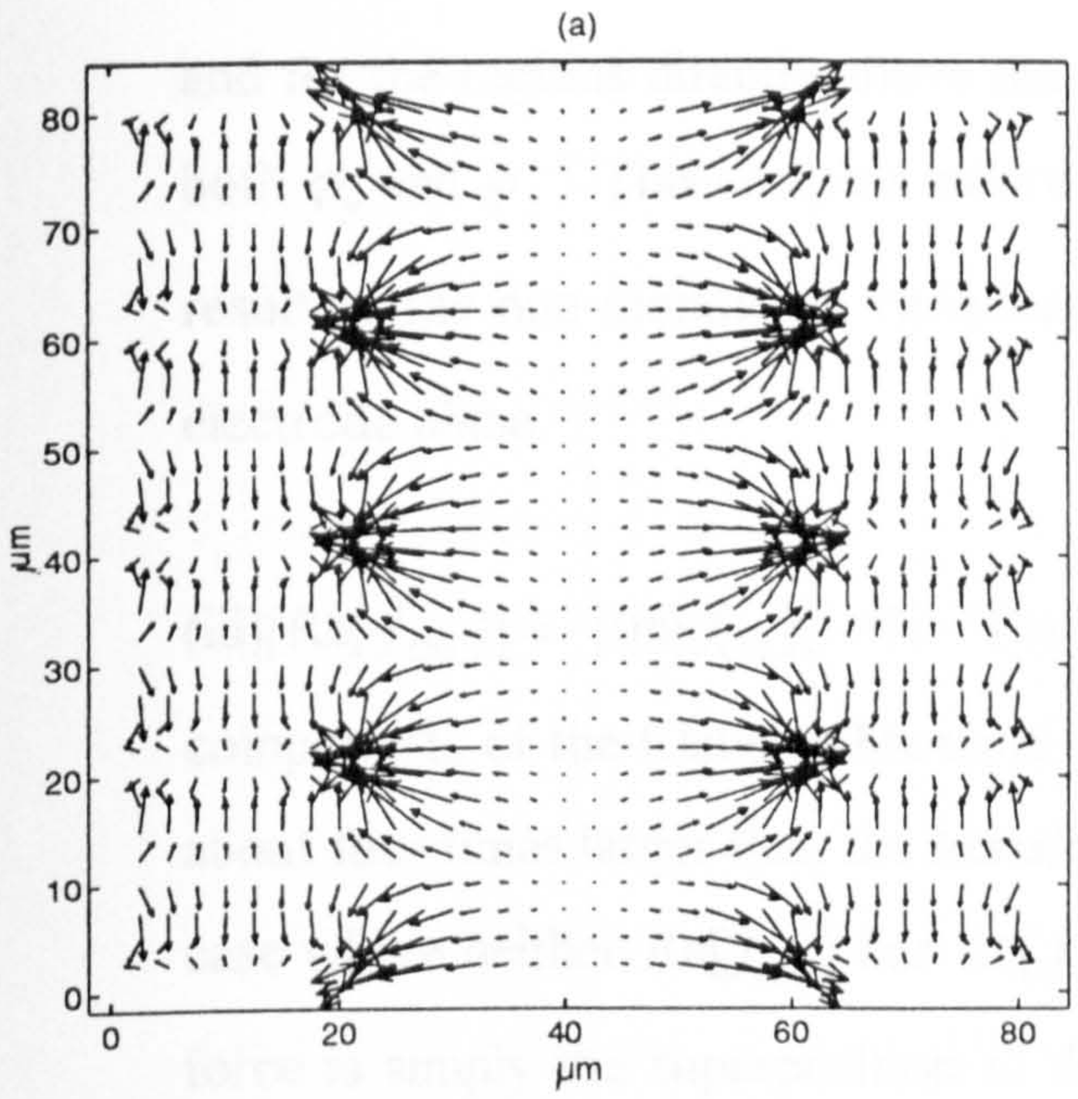

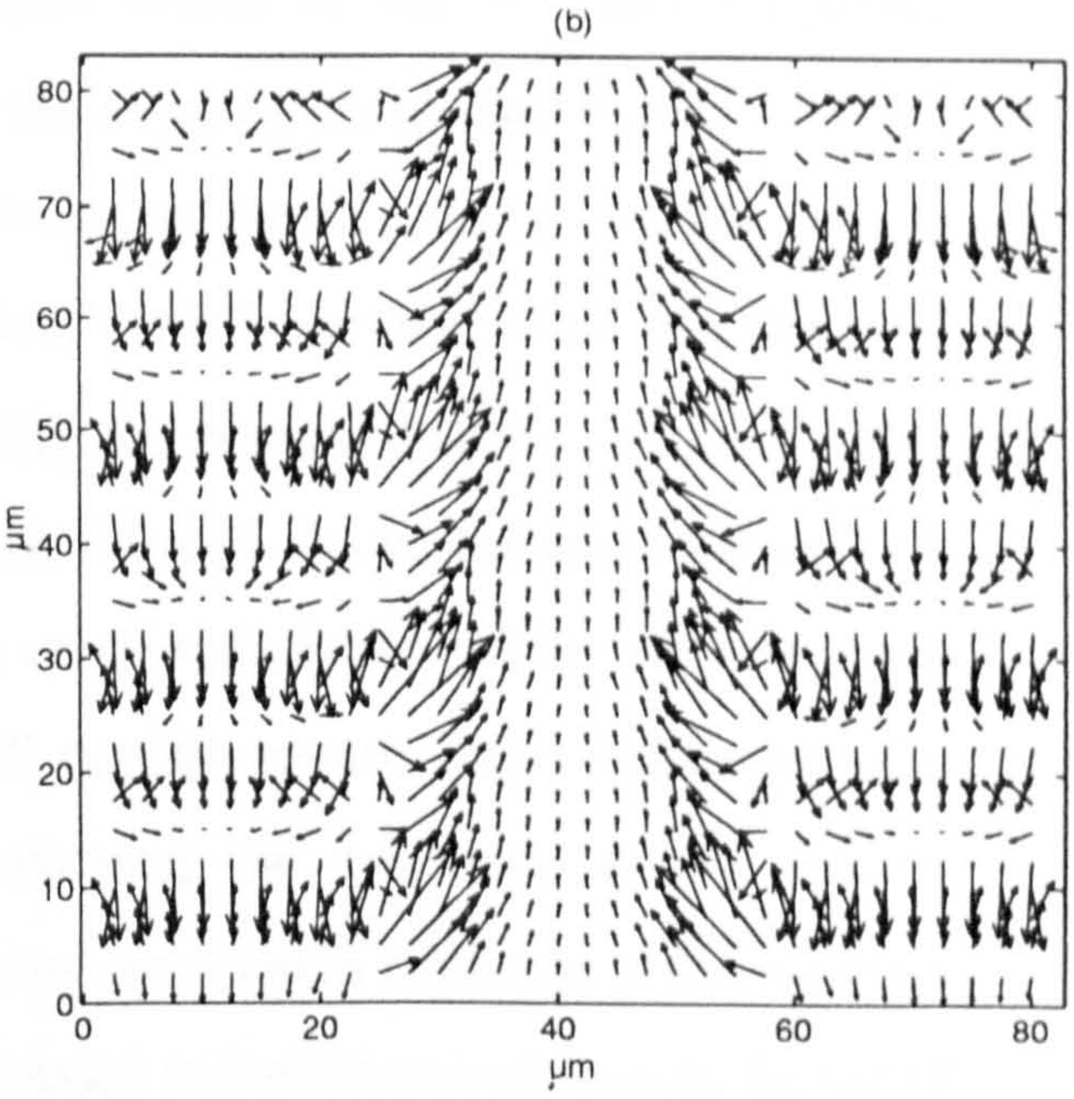

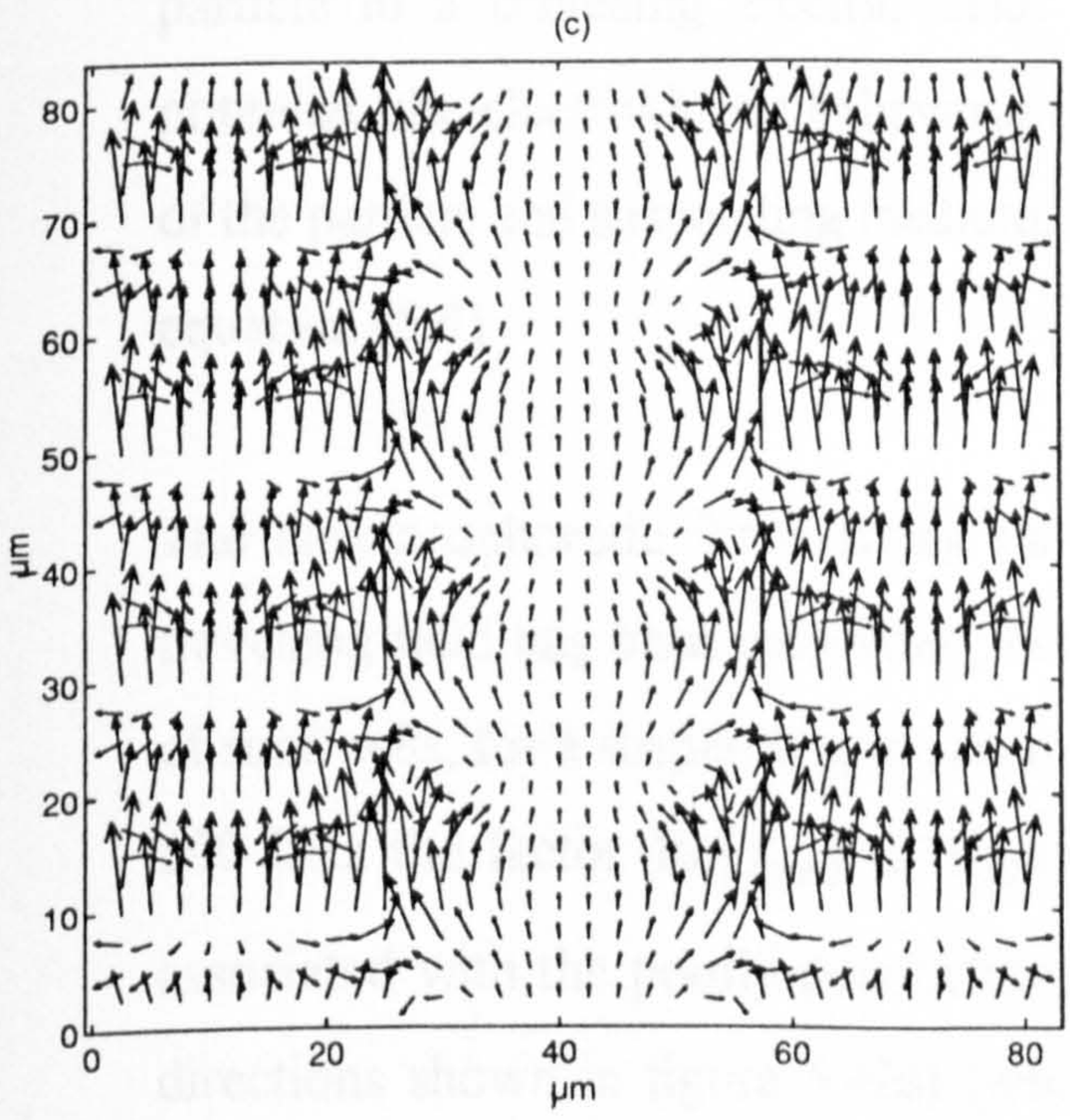

5.4 Dielectrophoretic forces acting on a particle of 3 μm radius in a travelling wave generated by the electrode geometry of figure 5.1 with applied 10 V pk sinusoidal signals, and for various relative values of the real (Re) and imaginary (Im) components of the Clausius-Mossotti factor f_{CM}.

(a) $\mathrm{Re}[f_{CM}] = 0.5$ and $\mathrm{Im}[f_{CM}] = 0$ in a plane 3μm above the electrodes.

(b) $\mathrm{Re}[f_{CM}] = 0$ and $\mathrm{Im}[f_{CM}] = 0.5$ in a plane 3μm above the electrodes.

(c) $\mathrm{Re}[f_{CM}] = 0$ and $\mathrm{Im}[f_{CM}] = 0.5$ in a plane 10μm above the electrodes.

component (Wang *et al* [15]), and because it gives rise to linear particle motion we term it a *translational force*. In the channel this force arises from the variation of φ_x, and for the regions directly above the electrode surface it depends on the variation of both φ_y and φ_z. This complex nature of the force vectors in the y-direction is a direct result of the non-monotonic variations of φ_y and φ_z with varying height above the electrode plane.

(iii)$|\mathrm{Re}[f_{CM}]| \approx |\mathrm{Im}[f_{CM}]| > 0$. For near equal values of the real and imaginary components of the Clausius-Mossotti factors, the *trapping force* (see figure 5.4(a)) is about four times larger than the *translational force* (see figure 5.4(b)). For the general case where neither $\mathrm{Re}[f_{CM}]$ nor $\mathrm{Im}[f_{CM}]$ is zero, the calculations reveal that the total force is simply the superposition of the trapping and translational force terms. This indicates that the real and imaginary parts of the induced dipole moment interact with the applied field *independently*, such that the combined effects of the trapping force and translational force determines the overall particle electrokinetic behaviour of a particle in a travelling electric field. On changing the frequency of the applied potential, the electrokinetic behaviour depends on the relative dielectric polarisabilities of the particle and suspending medium, as expressed in the Clausius-Mossotti factor of equation (5.4).

The dielectrophoretic force acting on yeast cells as a function of frequency of the travelling field has been calculated, based on the reported [5,16] dielectric properties of such cells, for a suspending medium conductivity of 40 mS/m. At frequencies below 500 kHz the factor $\mathrm{Re}[f_{CM}]$ is negative due to the low polarisability of yeast cells associated with the poorly-conducting cell membrane. On reversing the force vector directions shown in figure 5.4(a) (which corresponds with $\mathrm{Re}[f_{CM}]$ being negative), the trapping force can be seen to direct cells away from the electrode edges into the central regions of the channel. At such frequencies the cell's dielectric response time is much larger than that of the suspending medium, so that the induced dipole moment lags behind the applied field by more than half of the field period and a positive value is attained for $\mathrm{Im}[f_{CM}]$ (Huang *et al* [16]). Thus, a small translational force will act on

the cells and cause linear motion in the channel in the *opposite* direction to that of the travelling wave. However, cells located less than 5 μm above the electrode arrays will travel in the *same* direction as the travelling wave (see figure 5.5). As the frequency increases to 1MHz, Im[f_{CM}] increases and with it the rate of linear motion of the cell. Within a narrow frequency band where Im[f_{CM}] is between 4-6 times greater than Re[f_{CM}], the trapping and translational forces are of similar magnitude. This results in a highly complex force distribution, which contributes to the unpredictable particle behaviour observed experimentally at these frequencies and is referred to as the FUN effect [5].

For frequencies above 1 MHz, Re[f_{CM}] becomes positive as the applied field begins to penetrate the resistive plasma membrane and into the conductive cell interior [17]. At these frequencies the trapping force is much stronger than the translational force, causing cell motion towards electrode edges irrespective of their initial positions. Cells will remain trapped at electrode edges even though a translational force exists. Cell trapping continues until the frequency of the applied field increases to around 30 MHz, at which point the polarisability becomes dominated by permittivity rather than conductivity [8, 10]. Above 50 MHz the simulation predicts that yeast cells will be repelled again from the electrodes and undergo linear motion in the *same* direction as the travelling electric wave. This is summarised in figure 5.6, and the predictions concerning the travelling wave behaviour correlate well with experimentation [5 and unpublished work] using red blood cells, viable and non-viable yeast cells, and bacteria. The verified prediction that viable and non-viable cells will travel in opposite directions is of particular interest and of potential practical application.

Simulation of the dielectrophoretic force in the X-Y plane 10μm above the electrodes is shown in figure 5.4(c). An interesting result emerges, namely that the dielectrophoretic force above the electrodes is directed in the *same* sense as that in the channel, unlike the situation in the 3μm plane (figure 5.4(b)) where the forces in the channel and above the electrodes oppose each other. This effect occurs because the phase distortions arising from the physical presence of the electrodes is absent, and this has been confirmed by us (unpublished work) using yeast cells. Thus, with sinusoidal

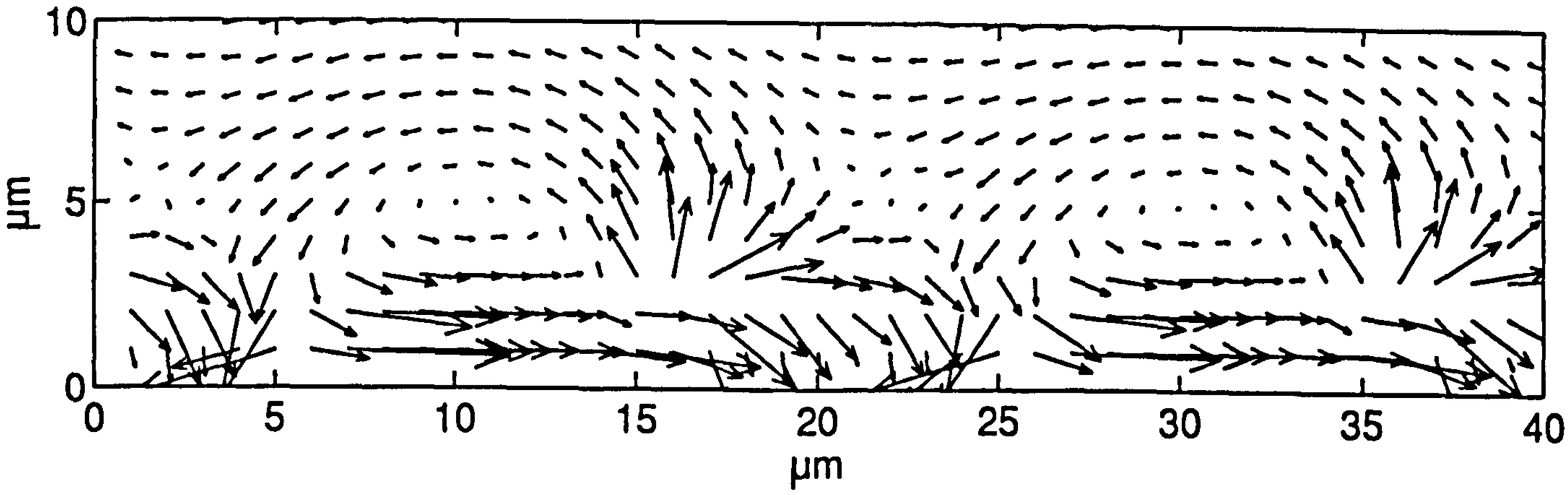

5.5 Imaginary force component ($\mathrm{Re}[f_{CM}] = 0$ and $\mathrm{Im}[f_{CM}] = 0.5$) acting in the vertical Y-Z plane intersecting the centre of an electrode array. The electrodes are depicted as bars at the bottom of the diagram.

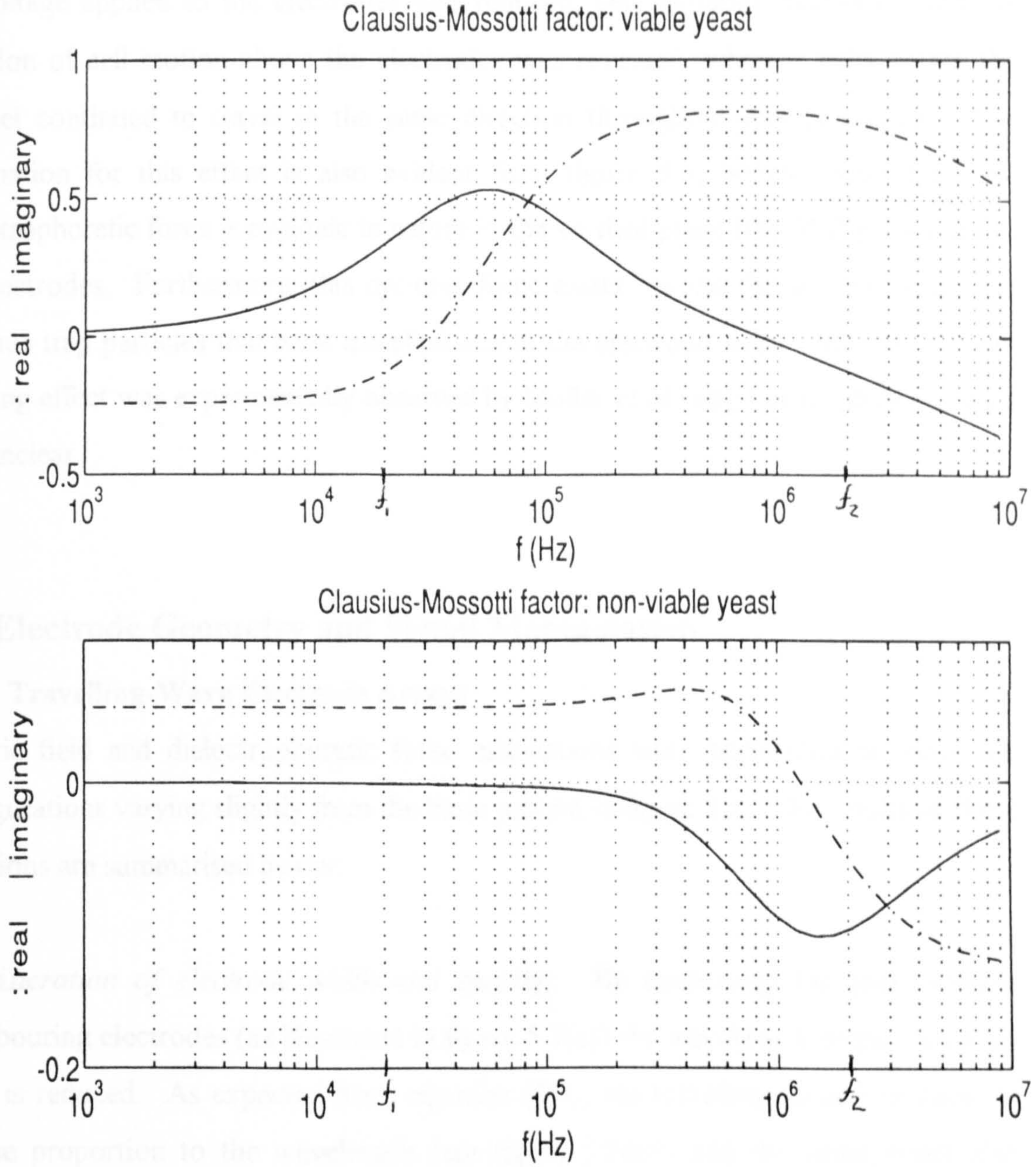

5.6 (a) Variations of $\mathrm{Re}[f_{CM}]$ and $\mathrm{Im}[f_{CM}]$ typically observed for viable cells in the frequency range 1kHz to 10MHz (eg. [5]). Travelling wave motion of particles will occur in the frequency range f_1. (b) Variations of $\mathrm{Re}[f_{CM}]$ and $\mathrm{Im}[f_{CM}]$ typically observed for non-viable cells (eg. [16]). Travelling wave motion of particles will occur in the frequency range f_2, and in the opposite direction to that occuring at f_1.

voltages of sufficient amplitude in the frequency range from 10kHz to 50kHz, yeast cells were levitated to a height of about 15μm above the electrodes and were observed to travel in the same direction as cells located in the central regions of the channel. As the voltage applied to the electrodes was reduced, cell levitation decreased and the direction of cell motion above the electrodes was reversed, whereas cells within the channel continued to travel in the same direction throughout this procedure. The explanation for this effect is also evident from figure 5.5, which shows how the dielectrophoretic force is cyclonic in nature in the vertical plane (the Y-Z plane) above the electrodes. Furthermore, this cyclonic force exists beyond the last electrode and can thus trap particles that have travelled across the electrode array. Such a particle-trapping effect was experimentally observed by Müller *et al* [18], but its physical cause was unclear.

5.4 Electrode Geometry and Signal Manipulation

5.4.1 Travelling-Wave Electrode Arrays

Electric field and dielectrophoretic force calculations were performed on electrode configurations varying slightly from the basic pattern in figure 5.1. The results of these variations are summarised below:

(i) *Alteration of electrode width and spacing.* By decreasing the gap between neighbouring electrodes (as illustrated in figure 5.7(a)) the wavelength of the travelling wave is reduced. As expected from equation (5.8), the travelling force increases in inverse proportion to the wavelength (see figure 5.7(b)), and the same result also occurs for the trapping force.

(ii) *Alteration of the channel width.* As opposing electrode pairs are progressively moved closer together, reducing the channel width (figure 5.7(c)), larger electric fields and hence larger travelling forces (figure 5.7(d)) and trapping forces are generated. Thus, through alteration of either the electrode spacing or channel width (or a combination of both) it should be possible to use the amplified trapping force which exists at the points of shortest wavelength or narrowest channel width to selectively

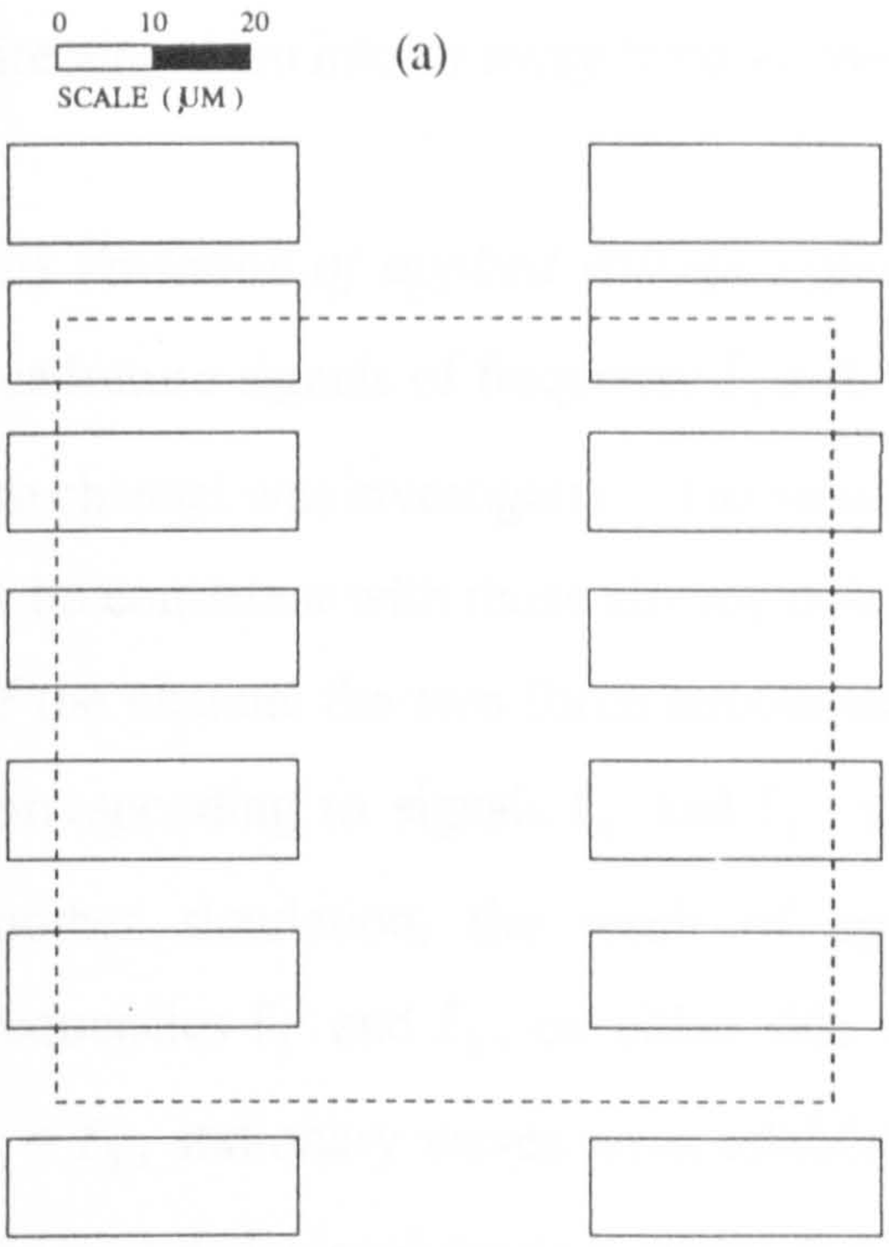

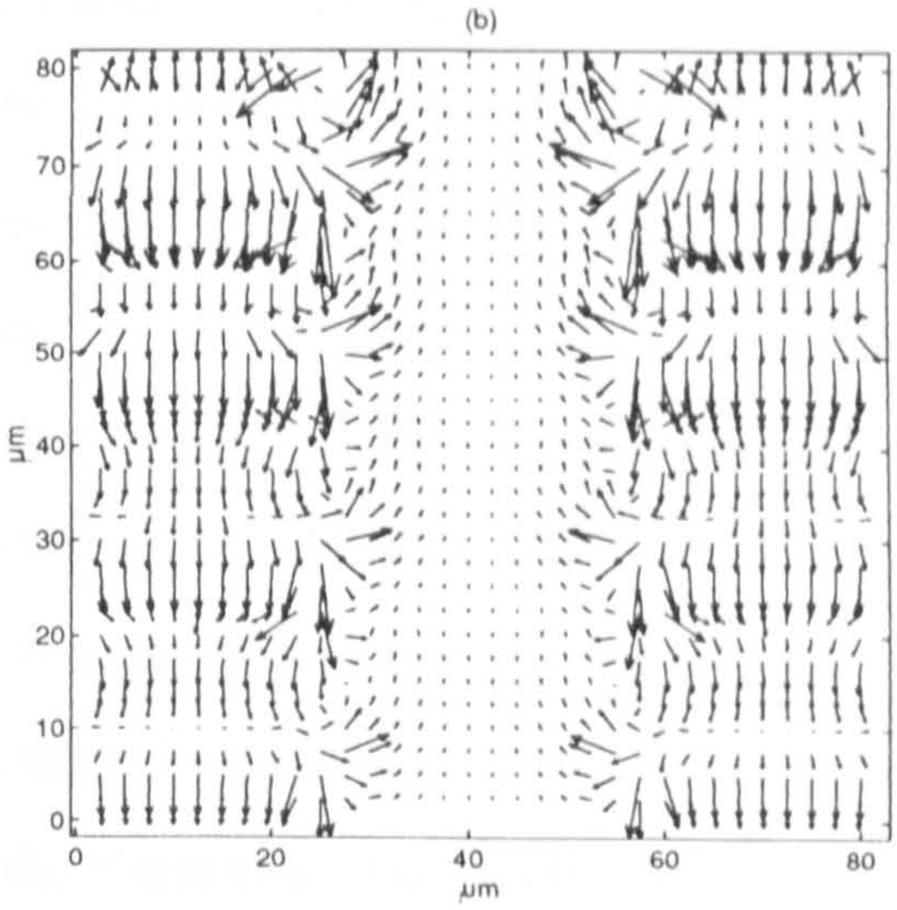

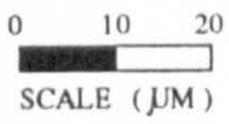

(c)

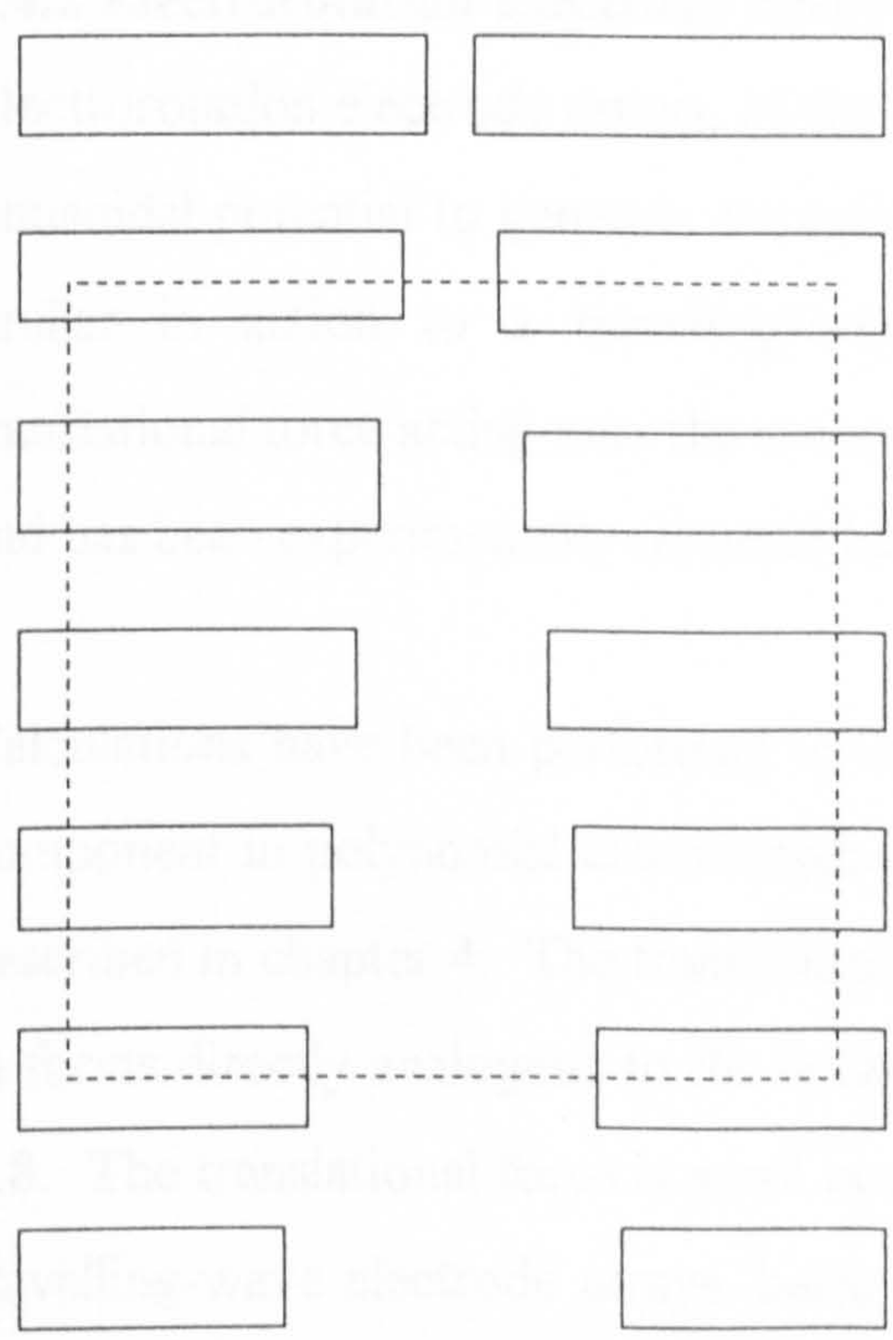

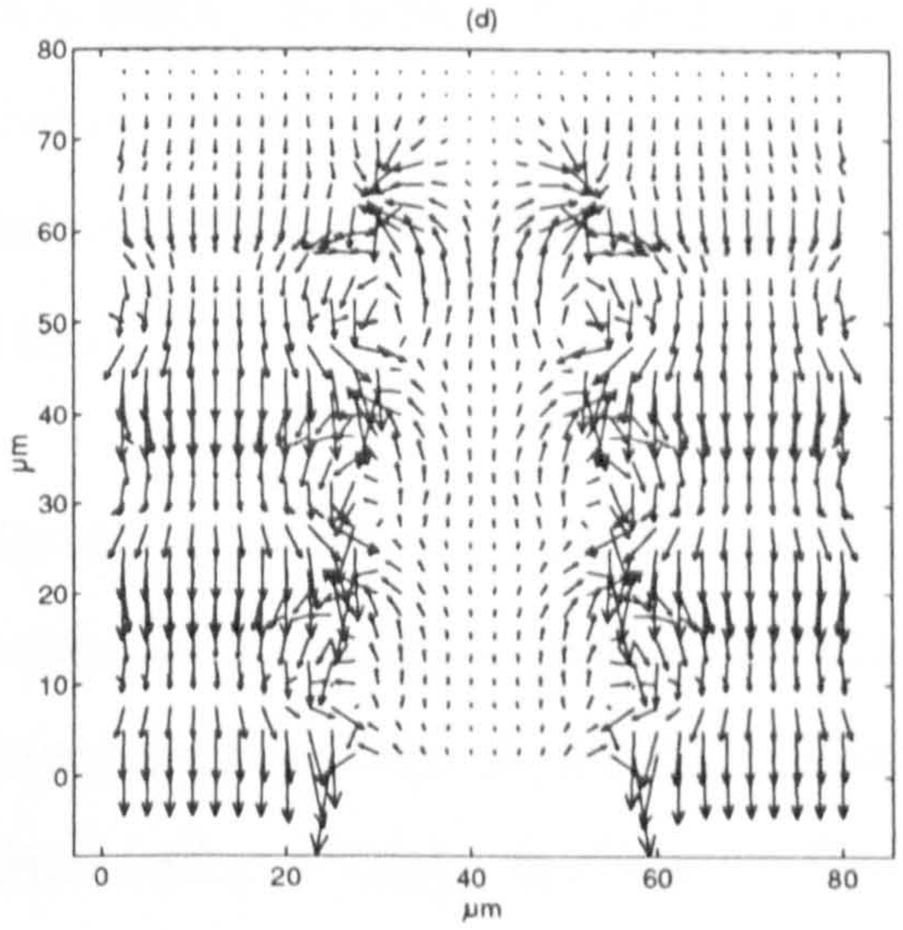

5.7 Examples of alternative electrode geometries, with the translational ($\mathrm{Im}[f_{CM}]$-related) force component illustrated: (a, b) variation of wavelength λ; (c, d) variation of channel width.

manipulate a subpopulation of particles in a mixture, either by trapping them or directing them into or away from a channel constriction.

(iii) *Variation of applied voltage signals.* The effect of applying two different phase quadrature signals of frequency f_1 and f_2 to the two electrode arrays on each side of the channel was investigated. The resultant forces acting over the electrodes are found to be consistent with those already described here for each frequency, but at the centre of the channel the two force structures are superimposed. Thus, translational forces corresponding to signals f_1 and f_2, are generated independently of each other. In another simulation, the result of applying counter-directed travelling waves, of frequencies f_1 and f_2, on either side of the channel was investigated. For the case $f_1 = f_2$, stationary waves were established in the channel so that under conditions of negative dielectrophoresis particles formed stationary and slowly rotating aggregations at the sites of the field minima.

5.4.2 Electrorotation Electrode Arrays

Electrorotation electrode arrays, of the type described in Chapter 4, employ a 4-phase sinusoidal potential to generate a rotating electric fields. In principle such an array is similar in action to a travelling-wave electrode array, and the presence of a translational force acting near the electrodes has been predicted by Hagedorn *et al* [19] and has been experimentally reported by Wang *et al* [20].

Calculations have been performed to investigate the presence of a translational force component in polynomial electrorotation electrode arrays, using the simulation model described in chapter 4. The translational and trapping forces were found to be present in forms directly analogous to the linear case described previously, as shown in figure 5.8. The translational force is small in comparison with the forces generated by linear travelling-wave electrode arrays, being some two orders of magnitude smaller at the electrode tips. As the electrode dimensions in this geometry are widely-spaced in comparison to those of the conventional travelling-wave array, the translational force is only of significant strength near the electrode edges. However, at greater heights

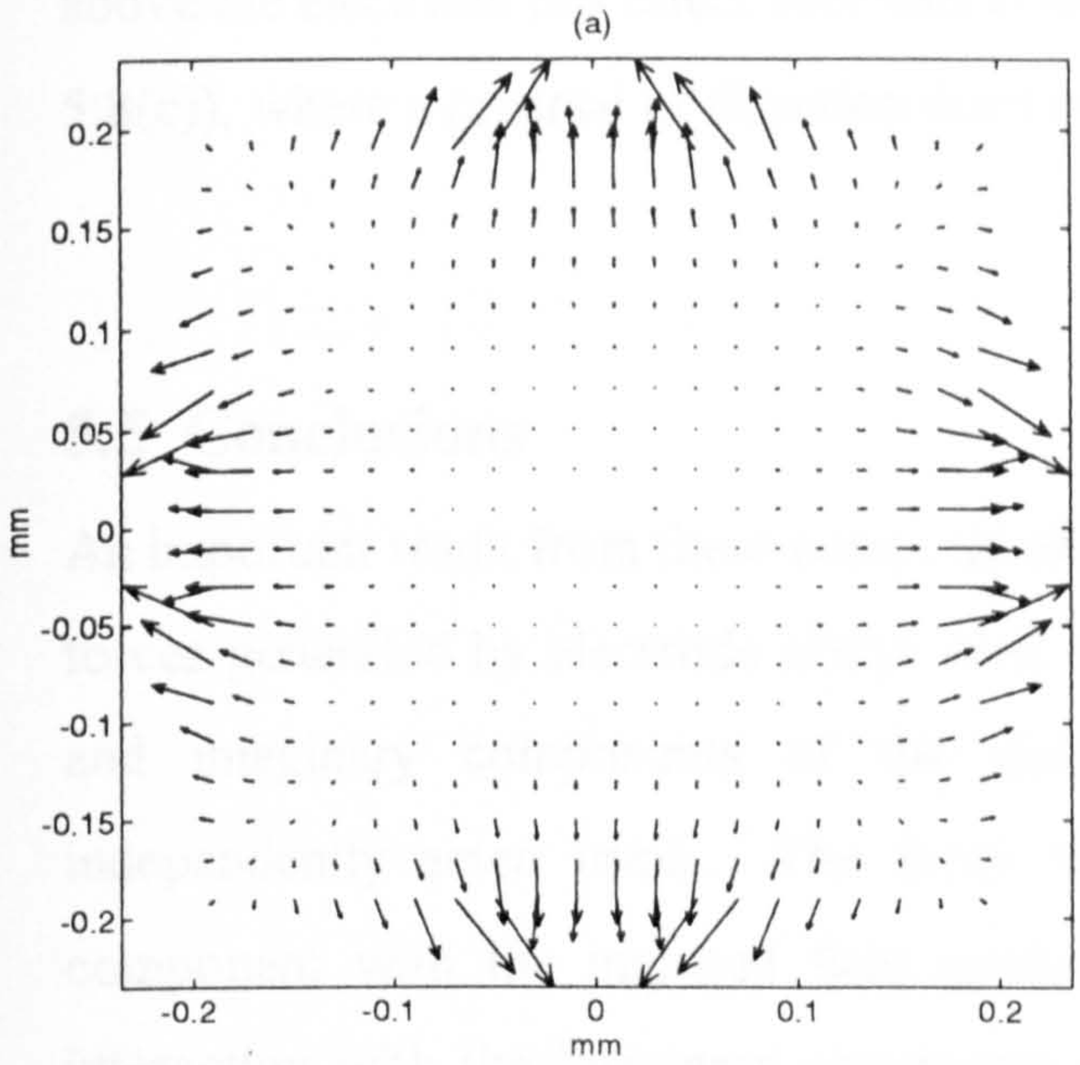

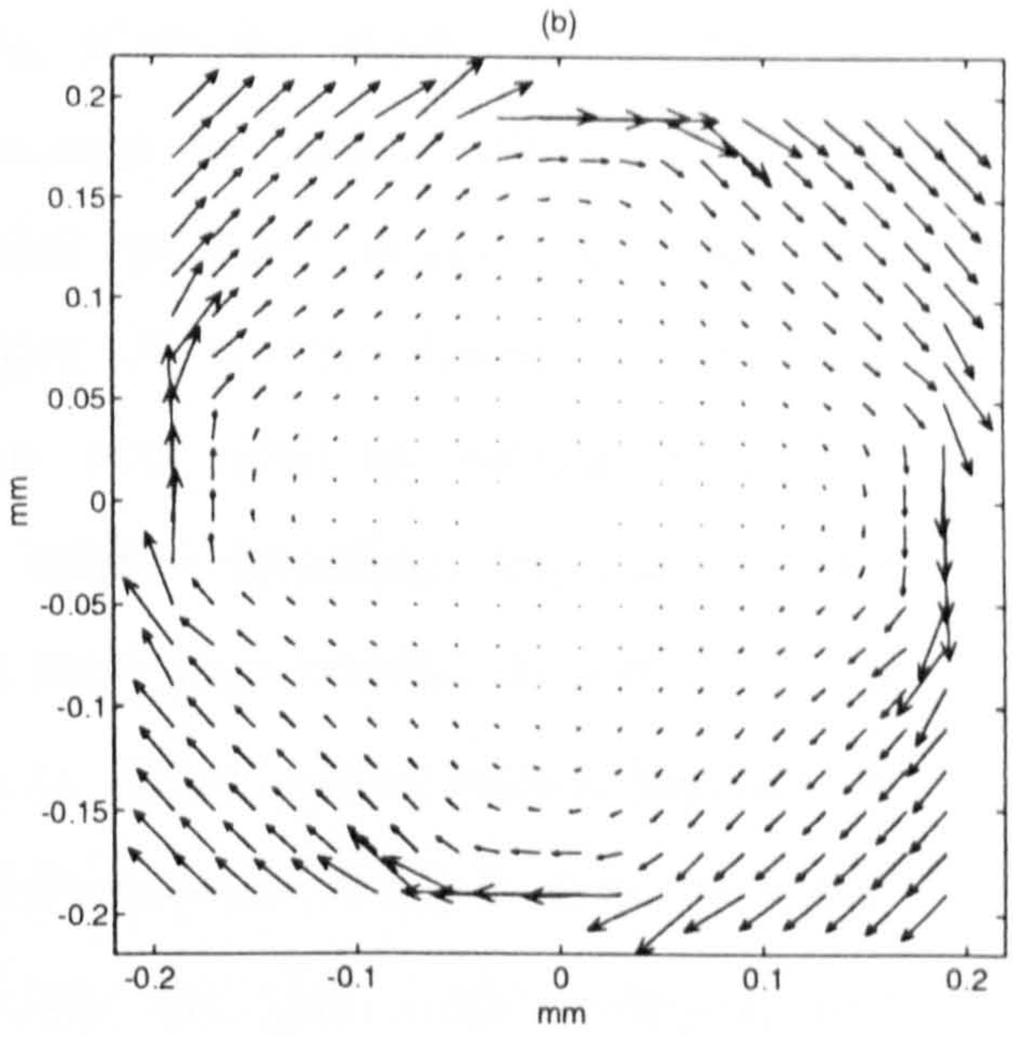

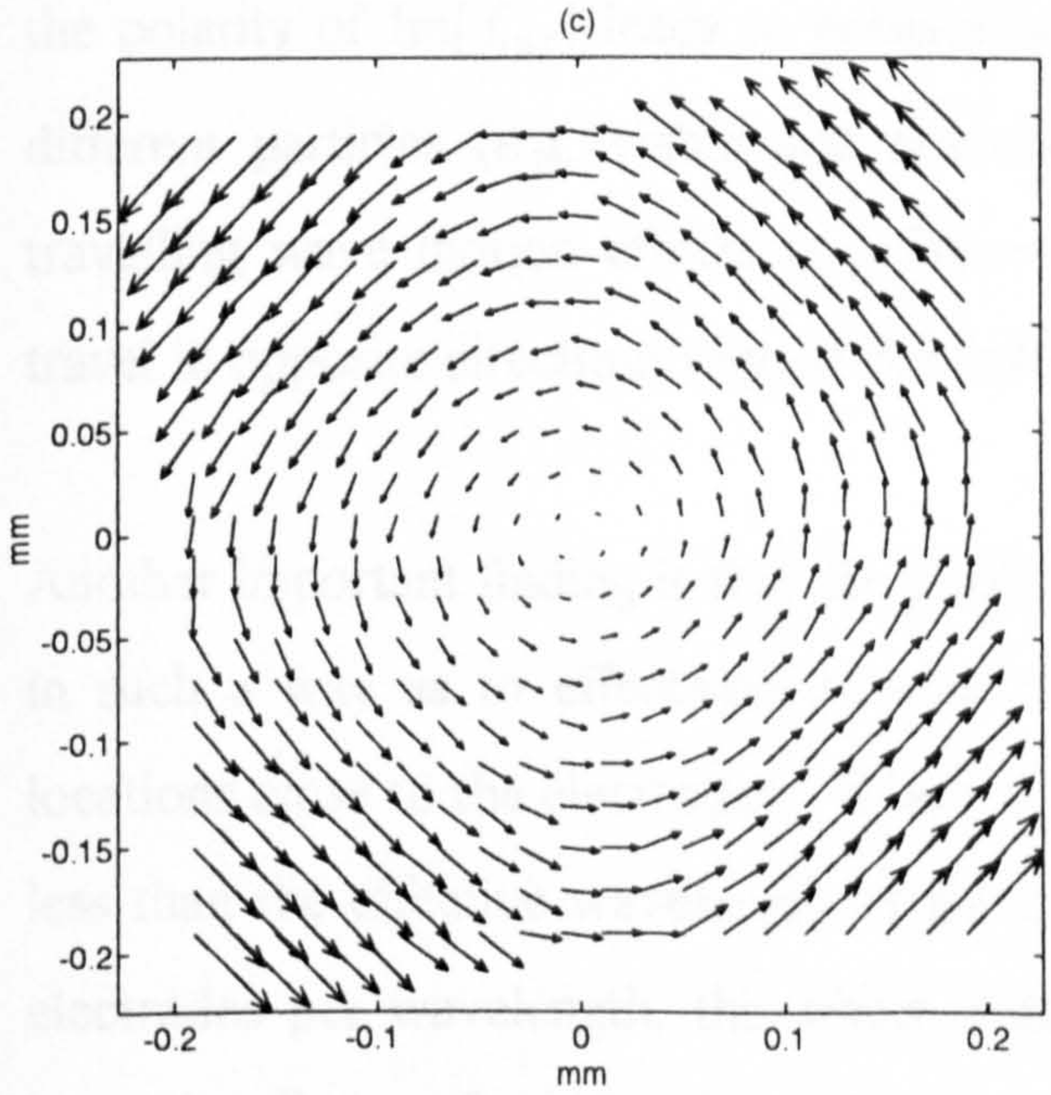

5.8 Dielectrophoretic forces acting on a particle of radius 3μm within a rotating electric field generated by polynomial electrodes of the type discussed in chapter 4, with applied 10 V pk sinusoidal signals, and for various relative values of the real (Re) and imaginary (Im) components of the Clausius-Mossotti factor f_{CM}.

(a) $\mathrm{Re}[f_{CM}] = 0.5$ and $\mathrm{Im}[f_{CM}] = 0$, in a plane 3μm above the electrodes.

(b) $\mathrm{Re}[f_{CM}] = 0$ and $\mathrm{Im}[f_{CM}] = 0.5$ in a plane 3μm above the electrodes.

(c) $\mathrm{Re}[f_{CM}] = 0$ and $\mathrm{Im}[f_{CM}] = 0.5$ in a plane 200μm above the electrodes..

above the electrode this effect becomes evident across the rotation chamber (see figure 5.8(c)), where a reversal of direction due to phase distortion is evident.

5.5 Conclusions

An important result from these computer simulations of the fields and dielectrophoretic forces generated by electrode arrays used to produce travelling fields is that the real and imaginary components of the dipole moment induced in a particle are independently acted upon. The force resulting from the interaction of the real component with the imposed field gradients induces a trapping effect, whilst the interaction with the imaginary component provides the force required to induce the lateral motion of a particle. As summarised in figure 5.6, the combination of these two forces results in particle travelling wave motion over relatively narrow frequency "windows", and is a sensitive function of the relative dielectric properties of the particle and surrounding medium as embodied in the Clausius-Mossotti factor f_{CM} of equations 5.3 and 5.4. The fact that the direction of induced lateral motion depends on the polarity of $\mathrm{Im}[f_{CM}]$ leads to potentially important practical applications in which different particles (e.g. viable and non-viable cells) not only exhibit trapping and travelling wave motion effects at different frequencies, but can also be induced to travel in opposite directions (e.g. at frequencies f_1 and f_2 in figure 5.6).

Another important finding is that the phase structure of the travelling field is distorted in such a way as to effectively reverse the direction of travelling wave motion in locations *close* to the electrodes. Where the electrodes approach a width that is much less than the effective wavelength of the travelling wave, and for a large number of electrodes per wavelength, this effect is reduced. For the case where a particle is located well away from the electrodes, phase distortion does not occur.

The Travelling wave effect may be compared with dielectrophoretic ratchets as described in Chapter 3. The method presented here offers greater scope for particle manipulation, separation and continuous transport than the ratchet method, and thus presents a more viable method for practical separation applications.

References

[1] Masuda S, Washizu M and Iwadare M 1987 *IEEE Trans. Ind. Appl.* **23** 474-81

[2] Masuda S, Washizu M and Kawabata I 1988 *IEEE Trans. Ind. Appl.* **24** 217-23

[3] Fuhr G, Hagedorn R, Müller T, Benecke W, Wagner B and Gimsa J 1991 *Studia Biophys.* **140** 79-102

[4] Hagedorn R, Fuhr G, Müller T and Gimsa J 1992 *Electrophoresis* **13** 49-54

[5] Huang Y, Wang X-B, Tame J A and Pethig R 1993 *J. Phys. D: Appl. Phys.* **26** 1528-35

[6] Fuhr G 1985 *Über die Rotation dielektrischer Körper in rotierenden Feldern, Dissertation,* Humboldt-Universität, Berlin, pp24-53

[7] Sauer F A and Schlögl R W 1985 *Interactions Between Electromagnetic Fields and Cells,* ed A Chiabrera *et al* (New York: Plenum) pp 203-51

[8] Wang X-B, Huang Y, Hölzel R, Burt J P H and Pethig R 1993 *J. Phys. D: Appl. Phys.* **26** 312-22

[9] Kaler K V I S and Jones T B 1990 *Biophys. J.* **57** 173-82

[10] Pethig R, Huang Y, Wang X-B and Burt J P H 1992 *J. Phys. D: Appl. Phys.* **25** 881-888

[11] Gascoyne P R C, Huang Y, Pethig R, Vykoukal J and Becker F F 1992 *Meas. Sci. Technol.* **3** 439-45

[12] Birtles A B, Mayo B J and Bennet A W 1973 *Proc. IEE* **120** 213-20

[13] Wang X-B, Huang Y, Burt J P H, Markx G H and Pethig R 1993 *J. Phys. D: Appl. Phys.* **26** 1278-85

[14] Hughes M P, Wang X-B, Becker F F, Gascoyne P R C and Pethig R 1994 *J. Phys. D: Appl. Phys.* **27** 1564-70

[15] Wang X-B, Huang Y, Gascoyne P R C and Becker F F 1994 *J. Phys. D: Appl. Phys.* **27** 1571-74

[16] Huang Y, Hölzel R, Pethig R and Wang X-B 1992 *Phys. Med. Biol* **37** 1499-1517

[17] Pethig R and Kell D B 1987 *Phys. Med. Biol.* **32** 33-970

[18] Müller T, Arnold W M, Schnelle T, Hagedorn R, Fuhr G and Zimmerman U 1993 *Electrophoresis* **14** 764-772

[19] Hagedorn R, Fuhr G, Mller T, Schnelle T, Schnakenberg U and Wagner B 1994 *J. Electrostatics* **33** 159-185

[20] Wang X-B, Hughes M P,Huang Y, Becker F F and Gascoyne P R C 1995 *Biochim. Biophys Acta* **1243** 185-194

Chapter 6

Conclusions

This work represents the first major study of all the principal forms of AC electrokinetics, including dielectrophoresis, electrorotation and travelling-wave dielectrophoresis, through the medium of computer simulation. Numerical study of the electric field, both in static and dynamic senses, for a wide range of microelectrode structures has presented the opportunity to examine the forces generated by AC electric fields directly. This has led to the affirmation of current dielectrophoretic theory by both accurately modelling the action of particles in previous experiments and by predicting new forms of behaviour within existing electrode structures.

Computer models have been devised using two numerical approximation methods, the Finite Element Method and the Method of Moments. Both models have been implemented for a range of problems and their characteristics, advantages and weaknesses have been evaluated. The Finite Element Method offers rapid simulation in either 2D or 3D problems, offers great accuracy at electrode edges and can be run on a small workstation, but provides results in a disordered fashion which may cause incompatibility when comparing two results directly or when several simulations of the same points in space are required. This method is thus more ideally suited to general AC studies where phase is not a factor in determining forces, such as the study of dielectrophoresis. The Method of Moments does offer that regularity of result positioning for repeated simulations and is more applicable to analyses of conditions where the model is stepped through several conditions, as is required in studies of electrorotation and travelling-wave effects. However, it is computationally inefficient and requires large computer facilities such as mainframes or supercomputers.

Dielectrophoresis is the motion of a particle due to its interaction with local non-uniform electric field gradients. The non-uniform nature of the field generates Coulombic forces of differing magnitudes at either pole of the particle dipole, resulting in a non-zero net force and resultant particle motion. The motion of the particle is dictated by the gradient of the field and the polarisability of the particle, a function related to the dielectric properties of both the body and the medium surrounding it. If the particle is more polarisable than the medium, net motion acts in the direction of highest electric field regions; if the medium is more polarisable, net motion acts towards low-field regions. Since these properties are dependent on frequency of the applied electric field, careful choice of medium and frequency enables the separation of a heterogeneous population of particles according to whether they experience positive or negative dielectrophoretic force.

Recent work has shown that the possibility exists for continuous transport of particles using asymmetrical "Christmas tree" -shaped electrodes. This principle has been established experimentally, but is inefficient and slow. Work presented here examines the principle of transport by "ratcheting" particles through a series of electrodes, and suggests principles for optimisation which should enhance the operation of these electrode structures. Furthermore, two advances to the design are proposed. Firstly, the introduction of an additional layer of electrodes would enable continuous particle motion based entirely on dielectrophoretic forces rather than employing particle diffusion as a means of particle transport,. Secondly, a study has been made of the use of such electrodes for continuous particle separation, based either on positive dielectrophoretic forces to draw particles of one type from a medium, or both positive and negative forces to actively separate particles by driving the two types in opposite directions.

Electrorotation is the phenomenon of induced torque in dielectric particles suspended in rotating electric fields. It arises due to the interaction of the dipole moment of the particle and the electric field, when the dielectric properties of the particle cause a phase difference between the rotation of the dipole and that of the applied field. This manifests as an induced torque as the dipole attempts to align with the rotating electric

field. Computations have been undertaken to provide a detailed analysis of the magnitudes and phases of the X, Y and Z components of the electric field across the inter-electrode space. These studies have shown that the phases of the X and Y components are not orthogonal, as has been assumed in the past, but deviate from this condition in areas away from the centre of the electrode chamber. Hence it is not only the electric field strength but the phase of the field components which determines electrorotational torque. The variation between the rotation of particles at the centre of the chamber and particles suspended nearer to the electrode tips can be considerable, varying by up to a factor of 2. Calculations show that torque remains within +/- 0.1 of the value at the centre of the chamber within a boundary covering only 13% of the area of a square defined by the electrode tips. Using a quality factor defined as a product of the area of the chamber which lies within this limit, and the relative torque produced at the centre of the chamber, ten different electrode geometries have been studied and evaluated according to their suitability for electrorotation studies.

By calculating the torque across the electrode chamber, it has been possible to create an accurate method for correcting the measured electrorotation rate of a given particle anywhere within the chamber. Two methods of correction have been supplied, both of which may be incorporated into image-processing software for the automatic calculation of rotation. In the first method, the simulation provides a normalisation factor against which the rotation of a particle may be corrected, according to its position within the chamber, in relation to the rotation or particles at the centre of the chamber. For the second method, a series of masks are provided which define the areas of the chamber where the variation of torque falls within well-defined limits. Both methods have advantages according to the circumstances and the needs of the experimentalist.

Travelling-wave dielectrophoresis is similar in principle to electrorotation; AC electric fields are swept laterally through a particle by means of a linearly-arranged electrode assembly. The properties of the particle cause a displacement between the electric field wave and the dipole moment, which results in a force moving the particle in the

direction of the applied wave. Phase differences greater than 180° will cause the particle to move in a direction contrary to the applied field.

Computer simulations of the electric fields and dielectrophoretic forces generated by electrode arrays have been studied. An important feature presented here is that the real and imaginary components of the dipole moment induced in a particle are independently acted upon. The real component of the dipole moment interacts with the imposed electric field gradient, is in phase with the applied field and induces dielectrophoresis. However, the imaginary component of the dipole moment is out of phase with the applied electric field wave, inducing the lateral motion of a particle as described above. Actual particle motion under arbitrary conditions of frequency, particle and medium properties is the superimposition of these two forces, where the magnitudes of the forces are dependent on the values of the real and imaginary components as described by the Clausius-Mossotti factor. This suggests possible means of using the different properties of particles in the separation of heterogeneous populations by selecting conditions (such as the suspending medium conductivity and the applied frequency) whereby the one particle type may be trapped whilst the other undergoes lateral motion, or even the induction of motion in opposite directions.

Close study of the predicted behaviour of particles indicates that particles reverse direction of travel when within approximately 5μm of the electrode surfaces, an observation later confirmed in experimental work. This phenomenon was found to be due to distortions in the phase of the electric field in the Y and Z directions. The effect may be minimised by using a greater number of electrodes per wavelength, thereby reducing the physical dimensions of the electrodes and inter-electrode gaps.

Travelling wave dielectrophoresis has also been studied in a range of alternative geometries, including studies of the manipulation of linear electrodes and alteration of the phase relationship between travelling potential waves on opposing sides of the channel. These studies have provided insights into potential applications in particle manipulation and separation. The travelling wave mechanism may be compared with the dielectrophoretic ratcheting system, which indicates that travelling wave

mechanisms are more flexible and effective in principle. However, the constructional simplicity of the latter method, requiring two electrodes rather than many, suggests that it may be more applicable as an embedded part of a larger electrode system. The first studies were also performed on the induction of travelling-wave effects in electrorotation electrodes.

This work has concentrated largely on the effects of electric fields on "unit" particles, in that the forces discussed here consider particles as though they do not interfere with the electric field surrounding them. Further work in this vein should incorporate modelling of particles such as cells between electrode structures, thereby considering any effects such particles may have on the electric field and each other, via dipole-dipole interactions. This could be extended to provide a highly detailed study, through simulation, of the electric fields through a cell considering factors such as the effects of organelles and examining the electric distribution through the cell in detail.

6.1 Publications Arising From This Work

Journals:

3 MP Hughes, R Pethig, X-B Wang 1995 **Forces on Particles in Travelling Electric Fields: Computer-Aided Simulations** Submitted to *J Phys D: Appl Phys*

2 X-B Wang, MP Hughes, Y Huang, FF Becker, PRC Gascoyne 1995 **Non-uniform Spacial Distributions of both the Magnitude and Phase of AC Electric Fields determine Dielectrophoretic Forces** *Biochim. Biophys. Acta* **1243** 185-194

1 MP Hughes, X-B Wang, FF Becker, PRC Gascoyne, R Pethig 1994 **Computer-Aided Analyses of Electric Fields Used in Electrorotation Studies** *J Phys D: Appl Phys* **27** 1564-1570

Conferences:

7 JPH Burt, R Pethig, MP Hughes, JP Kerslake, A Parton, D Dawson **Electrorotation Assay (ERA) for Cryptosporidium and Giardia from Raw Water Supplies** 9th International Conference on Electrostatics (York 1995)

6 MP Hughes, X-B Wang, JPH Burt, R Pethig, LR Watkins **Simulation of Travelling Electric Field Manipulation of Bioparticles,** 2nd International conference on Computation in Electromagnetics (Nottingham 1994)

5 JPH Burt, KL Chan, MP Hughes, GH Markx, R Pethig, MS Talary, X-F Zhou **AC Electrokinetic Manipulation of Cells and Bioparticles,** 1st Joint Institute of Physical Sciences in Medicine and Biological Engineering Society Annual Conference (Keele 1994)

4 X-B Wang, Y Huang, MP Hughes, R Pethig, PRC Gascoyne, FF Becker **Separation of Biological Cells using Travelling Electric Fields,** 38th Biophysical Society Annual Conference (New Orleans 1994)

3 PRC Gascoyne, Y Huang, MP Hughes, X-B Wang, R Pethig, FF Becker **Manipulation of Erythroleukaemia Cells using Travelling Electric Fields** 16th Annual IEEE EMBS International Conference (Baltimore 1994)

2 X-B Wang, Y Huang, MP Hughes, R Pethig, PRC Gascoyne, FF Becker **Separation of Friend Murine Erythroleukaemic Cells using Travelling Electric Fields** 1st International Conference on Cellular Engineering (Keele 1993)

1 R Pethig, FF Becker, JPH Burt, KL Chan, PRC Gascoyne, R Hölzel, Y Huang, MP Hughes, GH Markx, MS Talary, H-W Tang, X-B Wang, X-F Zhou **Characterisation and Manipulation of Cells using AC Electrical Fields** 1st International Conference on Cellular Engineering (Keele 1993)

Appendix I

Finite Element Method
Field Calculation Program

The two programs presented in Appendix I are collectively used to perform the travelling-wave dielectrophoresis problem described in Chapter 2 section 2.5 via the Finite Element method. The suite comprises a data generator which is specific to the problem described here, and a generic Finite Element solver which may be used for any problem proveded the inpou is of a similar format.

The first program generates the numbers and co-ordinates of the nodes, and specifies the locations of known potentials and material properties. Known potentials are determined after the user has entered the starting phase angle. This data is saved in a data file (input.dat) which is loaded by the second program.

This is a generic Finite Element solver which follows the procedures described in section 2.2, to which references are made throughout the program. The program produces as output a list of the potentials at all node locations in sequence, which are stored in file output.dat.

```
c       FEMgen      FINITE ELEMENT ANALYSIS PROGRAM FOR 3D
c                   ELECTRODE STUDY - DATA GENERATION MODULE
c
c       Written by: Michael Hughes
c
c
c
      OPEN          (10,file='input.dat',status='new')
c
c     Part 1: Generate the co-ordinates of all nodes; the order of nodes in the list
c     dictates the node number.  Note that the nodes are not all equally spaced.
c

      nodes=5406
      nelements=4160
      write(10,*) nelements,nodes,1088
      do 200 k=1,6
      if (k.eq.1) wm=0
      if (k.eq.2) wm=.1
      if (k.eq.3) wm=2.6
      if (k.eq.4) wm=5.1
      if (k.eq.5) wm=10
      if (k.eq.6) wm=100
c
      do 13 i=1,17
      write(10,*) (i*2.5e-6),(2.5e-6),wm*1e-6
13     continue
      do 15 i=1,17
      write(10,*) (i*2.5e-6),(3.75e-6),wm*1e-6
15     continue
      do 17 i=1,17
      write(10,*) (i*2.5e-6),(5e-6),wm*1e-6
17     continue
      do 19 i=1,17
      write(10,*) (i*2.5e-6),(6.25e-6),wm*1e-6
19     continue
      do 21 i=1,17
      write(10,*) (i*2.5e-6),(7.5e-6),wm*1e-6
21     continue
      do 1 j=1,43
      do 1 i=1,17
      write(10,*) (i*2.5e-6),((j+3)*2.5e-6),wm*1e-6
1      continue
      do 14 i=1,17
      write(10,*) (i*2.5e-6),(117.5e-6),wm*1e-6
14     continue
      do 16 i=1,17
      write(10,*) (i*2.5e-6),(118.75e-6),wm*1e-6
```

```
16     continue
       do 18 i=1,17
       write(10,*) (i*2.5e-6),(120e-6),wm*1e-6
18     continue
       do 20 i=1,17
       write(10,*) (i*2.5e-6),(121.25e-6),wm*1e-6
20     continue
       do 22 i=1,17
       write(10,*) (i*2.5e-6),(122.5e-6),wm*1e-6
22     continue
200  continue
c
c      Part 2:  Generate a table containing the number of nodes in a given element (in
       this case 8) followed by the number of nodes relating to that element.
c
       j=1
       k=1
       m=1
       do 25 i=1,nelements
       write(10,*) 8
       write(10,*) j
       write(10,*) j+1
       write(10,*) j+18
       write(10,*) j+17
       write(10,*) j+901
       write(10,*) j+902
       write(10,*) j+919
       write(10,*) j+918
       write(10,*) ' '
       j=j+1
       k=k+1
       m=m+1
       if (k.ne.17) goto 2
       k=1
       j=j+1
2      continue
       if (m.ne.833) goto 25
       m=1
       j=j+17
25     continue
c
c      Part 3: Define materials parameters (permettivity and current density) for all
       elements
c
       do 3 i=1,nelements
       write(10,*) 8.84e-12,0
3      continue
c
c
```

```
c       Part 4: Determine boundary potentials for a given phase of the travelling wave
c       potentials, and assign these potentials to the nodes coinciding with the
c       electrode boundaries.
c
        print *,'Please enter primary wave angle (whole degrees) :'
        read *, iangle
        angle=float(iangle)*0.0175
        do 4 k=1,2
        do 4 i=1,7
        do 4 n=1,5
        j=(i-1)*136 + (n-1)*17 + (k-1)*901
        w=1.57*(i-1)
        v=10*cos(angle+w)
        write(10,*) 1+j,v
        write(10,*) 2+j,v
        write(10,*) 3+j,v
        write(10,*) 4+j,v
        write(10,*) 5+j,v
        write(10,*) 6+j,v
        write(10,*) 7+j,v
        write(10,*) 8+j,v
        write(10,*) 9+j,v
        write(10,*) 10+j,v
        write(10,*) 11+j,v
4       continue
c
        end
```

```
c       FEM3D:      FINITE ELEMENT ANALYSIS PROGRAM FOR 3D
c                   ELECTRODE STUDY - CALCULATION MODULE
c
c
c
c
c       PROGRAM STRUCTURE:
c
c       Section One:   Read in data files and generate variables
c       Section Two:   Generate system matrices
c       Section Three: Impose boundary conditions
c       Section Four:  Solve the equation and save results
c       Section Five:  Subroutines
c
c
c       Variable declarations:
c
        REAL        NC,EC,BC,NodePotential
        REAL        EP,Potential,SV,SM,w
        REAL        jacob,ijacob,kk,fact,dpsi,nu,xi,eta
c
        INTEGER     NumNodes,NumElements,EN,NPE
        INTEGER     Node,E
c
        DIMENSION xi(8),eta(8),nu(8),w(8),apsi(8),dpsidz(8)
        DIMENSION ijacob(3,3)
        DIMENSION dpsi(3,8),dpsidx(8),dpsidy(8),jacob(3,3)
        DIMENSION NPE(5500),NC(5500,3)
        DIMENSION EN(5500,8),BC(5500,2)
        DIMENSION EP(5500,2),EC(5500,8,3)
        DIMENSION SM(5500,5500)
        DIMENSION SV(5500,2),SV2(5500)
        DIMENSION workspace(5500),NodePotential(5500)
c
        OPEN        (20,file='input.dat',status='old')
        OPEN        (10,file='output.dat',status='new')
c
c       Variables list:
c       NC - nodal co-ordinates                          EC - element coordinates
c       BC - boundary conditions table                   EP - element properties
c       EN - table of nodes in each element
c       NPE - list of the number of nodes in each element
c       NodePotential - output potential at all nodes SM- system matrix
c       Potential - boundary condition potentials      SV-system vector
c       NumNodes - total number of nodes               w - weightings
c       NumElements - total number of elements
c       jacob - the Jacobian matrix                    ijacob - inverse Jacobian matrix
c       nu, eta, xi - dimensions of the master element
c       dpsi, dpsidx, dpsidy, dpsidz - differentials for mapping to the master element
```

```
c       SECTION 1 :: READ IN DATA FILES AND GENERATE VARIABLES
c
        print *,'Reading data file...'
        read(20,*) NumElements,NumNodes,NumBC
        print *,NumNodes,NumElements,NumBC
        do 1 l=1,NumNodes
        read(20,*) NC(l,1),NC(l,2),NC(l,3)
1       continue
        do 2 i=1,NumElements
        read(20,*) NPE(i)
        do 2 j=1,NPE(i)
        read(20,*) EN(i,j)
2       continue
        do 3 i=1,NumElements
        read(20,*) EP(i,1),EP(i,2)
3       continue
        do 20 i=1,NumBC
        read(20,*) BC(i,1),BC(i,2)
        print *, BC(i,1),BC(i,2)
20      continue
        print *,'Done.'
        do 4 i=1,NumElements
        do 4 j=1,NPE(i)
        do 4 k=1,3
        EC(i,j,k)=NC((EN(i,j)),k)
4       continue
c
c
c       SECTION 2 :: GENERATE SYSTEM MATRICES
c
        print *,'Generating system matrices...'
        do 5 E=1,NumElements
c
c       Gauss Quadrature points (see Thesis, section 2.2.3):
c
        x=-0.57735
        xi(1)=x
        xi(2)=-x
        xi(3)=x
        xi(4)=-x
        xi(5)=x
        xi(6)=-x
        xi(7)=x
        xi(8)=-x
        eta(1)=x
        eta(2)=x
        eta(3)=-x
        eta(4)=-x
```

```
      eta(5)=x
      eta(6)=x
      eta(7)=-x
      eta(8)=-x
      nu(1)=x
      nu(2)=x
      nu(3)=x
      nu(4)=x
      nu(5)=-x
      nu(6)=-x
      nu(7)=-x
      nu(8)=-x
c
c     weightings:
c
      w(1)=1
      w(2)=1
      w(3)=1
      w(4)=1
      w(5)=1
      w(6)=1
      w(7)=1
      w(8)=1
c
c
c     The following section determines the potential across a single element,
c     following a method based on that described in section 2.2.3, expended to 3D
c     elements
c
      do 5 i=1,8
      call shape(apsi,dpsi,xi(i),eta(i),nu(i))
      call jacobian(jacob,E,EC,dpsi)
      call ijacobian(ijacob,jacob)
      call calcdpsidxyz(dpsidx,dpsidy,dpsidz,dpsi,ijacob)
      fact=determinant(jacob)
      do 5 j=1,8
      SV(EN(E,j),1)=SV(EN(E,j),1)+EP(E,2)*apsi(j)*fact
      do 5 k=1,8
      RK=EP(E,1)*(dpsidx(j)*dpsidx(k)+dpsidy(j)*dpsidy(k)+
     1     dpsidz(j)*dpsidz(k))*fact
      SM(EN(E,j),EN(E,k))=SM(EN(E,j),EN(E,k))+RK
5     continue
      print *,'Done.'
c
c
c     SECTION 3 :: IMPOSE BOUNDARY CONDITIONS
c     (see thesis section 2.2.5)
c
      print *,'Calculating boundary conditions...'
```

```
      do 6 i=1,NumBC
      Node=BC(i,1)
      Potential=BC(i,2)
      do 7 j=1,NumNodes
      if (SV(j,2).eq.0) SV(j,1)=SV(j,1)-(SM(j,Node)*Potential)
7     continue
      SV(Node,1)=Potential
c     print *,Potential
      SV(Node,2)=1
6     continue
c
c
      do 8 i=1,NumBC
      Node=BC(i,1)
      do 9 j=1,NumNodes
      SM(j,Node)=0
      SM(Node,j)=0
9     continue
      SM(Node,Node)=1
8     continue
      print *,'Done.'
c
c
c     SECTION 4 :: SOLVE THE EQUATION AND SAVE RESULTS
c     Solve the system equation using NAG routine F04ARE
c
      do 15 i=1,NumNodes
      SV2(i)=SV(i,1)
c     print *, SV2(i)
15    continue
      print *,'Solving the equation...'
      call F04ARE(SM,5500,SV2,NumNodes,NodePotential,workspace,ifail)
      do 10 i=1,NumNodes
c     write(10,*) i,NC(i,1),NC(i,2),NodePotential(i)
      write(10,*) NodePotential(i)
10    continue
      do 18 i=1,4
      do 18 j=1,4
18    continue
      print *,'Done. End program'
      end
c
c
c     SECTION 5 :: SUBROUTINES
c
c     Generate the shape function in terms of the Gaussian quadrature points.
c
      subroutine shape(apsi,dpsi,z,q,r)
      DIMENSION apsi(4),dpsi(3,8)
```

```
      REAL          apsi,dpsi,q,r,z
      apsi(1)=0.125*((1-z)*(1-q)*(1-r))
      apsi(2)=0.125*((1+z)*(1-q)*(1-r))
      apsi(3)=0.125*((1+z)*(1+q)*(1-r))
      apsi(4)=0.125*((1-z)*(1+q)*(1-r))
      apsi(5)=0.125*((1-z)*(1-q)*(1+r))
      apsi(6)=0.125*((1+z)*(1-q)*(1+r))
      apsi(7)=0.125*((1+z)*(1+q)*(1+r))
      apsi(8)=0.125*((1-z)*(1+q)*(1+r))
      dpsi(1,1)=0.125*((1-q)*(1-r))*(-1)
      dpsi(1,2)=0.125*((1-q)*(1-r))
      dpsi(1,3)=0.125*((1+q)*(1-r))
      dpsi(1,4)=0.125*((1+q)*(1-r))*(-1)
      dpsi(1,5)=0.125*((1-q)*(1+r))*(-1)
      dpsi(1,6)=0.125*((1-q)*(1+r))
      dpsi(1,7)=0.125*((1+q)*(1+r))
      dpsi(1,8)=0.125*((1+q)*(1+r))*(-1)
      dpsi(2,1)=0.125*((1-z)*(1-r))*(-1)
      dpsi(2,2)=0.125*((1+z)*(1-r))*(-1)
      dpsi(2,3)=0.125*((1+z)*(1-r))
      dpsi(2,4)=0.125*((1-z)*(1-r))
      dpsi(2,5)=0.125*((1-z)*(1+r))*(-1)
      dpsi(2,6)=0.125*((1+z)*(1+r))*(-1)
      dpsi(2,7)=0.125*((1+z)*(1+r))
      dpsi(2,8)=0.125*((1-z)*(1+r))
      dpsi(3,1)=0.125*((1-z)*(1-q))*(-1)
      dpsi(3,2)=0.125*((1+z)*(1-q))*(-1)
      dpsi(3,3)=0.125*((1+z)*(1+q))*(-1)
      dpsi(3,4)=0.125*((1-z)*(1+q))*(-1)
      dpsi(3,5)=0.125*((1-z)*(1-q))
      dpsi(3,6)=0.125*((1+z)*(1-q))
      dpsi(3,7)=0.125*((1+z)*(1+q))
      dpsi(3,8)=0.125*((1-z)*(1+q))
      return
      end
c
c
c     Determine the Jacobian of the co-ordinate transform (equation 2.27)
c
      subroutine jacobian(jacob,E,EC,dpsi)
      DIMENSION jacob(3,3),EC(5500,8,3),dpsi(3,8)
      REAL      jacob,EC
      INTEGER   E
      do 50 i=1,3
      do 50 j=1,3
      jacob(i,j)=0
      do 50 k=1,8
      jacob(i,j)=jacob(i,j)+(dpsi(j,k) * EC(E,k,i))
50    continue
```

```
      return
      end
c
c
c     Perform Thesis equation 2.28
c
      subroutine calcdpsidxyz(dpsidx,dpsidy,dpsidz,dpsi,ijacob)
      DIMENSION dpsidz(8),dpsi(3,8),ijacob(3,3)
      DIMENSION dpsidx(8),dpsidy(8)
      REAL      ijacob
      do 51 i=1,8
      dpsidx(i)=dpsi(1,i)*ijacob(1,1)-
     1     dpsi(2,i)*ijacob(2,1)+dpsi(3,i)*ijacob(3,1)
      dpsidy(i)=(-1)*dpsi(1,i)*ijacob(1,2)+
     1     dpsi(2,i)*ijacob(2,2)-dpsi(3,i)*ijacob(3,2)
      dpsidz(i)=dpsi(1,i)*ijacob(1,3)-
     1     dpsi(2,i)*ijacob(2,3)+dpsi(3,i)*ijacob(3,3)
51    continue
      return
      end
c
c
c     Calculate the inverse of the Jacobian matrix
c
      subroutine ijacobian(ijacob,matrix)
      DIMENSION ijacob(3,3),matrix(3,3)
      REAL      ijacob,determinant,det1,matrix
      det1=determinant(matrix)
      ijacob(1,1)=matrix(2,2)*matrix(3,3) -
     1     matrix(3,2)*matrix(2,3)
      ijacob(2,1)=(matrix(2,1)*matrix(3,3) -
     1     matrix(2,3)*matrix(3,1))*(-1)
      ijacob(3,1)=matrix(2,1)*matrix(3,2) -
     1     matrix(2,2)*matrix(3,1)
      ijacob(1,2)=(matrix(1,2)*matrix(3,3) -
     1     matrix(1,3)*matrix(3,2))*(-1)
      ijacob(2,2)=matrix(1,1)*matrix(3,3) -
     1     matrix(1,3)*matrix(3,1)
      ijacob(3,2)=(matrix(1,1)*matrix(3,2) -
     1     matrix(1,2)*matrix(3,1))*(-1)
      ijacob(1,3)=matrix(1,2)*matrix(2,3) -
     1     matrix(2,2)*matrix(1,3)
      ijacob(2,3)=(matrix(1,1)*matrix(2,3) -
     1     matrix(1,3)*matrix(2,1))*(-1)
      ijacob(3,3)=matrix(1,1)*matrix(2,2) -
     1     matrix(1,2)*matrix(2,1)
      do 51 i=1,3
      do 51 j=1,3
      ijacob(i,j)=ijacob(i,j)/det1
```

```
51      continue
        return
        end
c
c
c       Calculate the determinant of a matrix
c
        function determinant(matrix)
        DIMENSION matrix(3,3)
        REAL      matrix,det1,det2,det3,determinant
        det1=(matrix(1,1))*(matrix(2,2)*matrix(3,3)-
     1      matrix(3,2)*matrix(2,3))
        det2=(matrix(1,2))*(matrix(2,1)*matrix(3,3)-
     1      matrix(2,3)*matrix(3,1))
        det3=(matrix(1,3))*(matrix(2,1)*matrix(3,2)-
     1      matrix(2,2)*matrix(3,1))
        determinant=det1 - det2 + det3
        return
        end
```

Appendix II

Method of Moments
Field Calculation Program

As in the previous section, the programs presented here are those used to perform the Method of Moments simulation in section 2.5. Furthermore, the solver program (the second listed here) was also used to perform the simulation work for chapers 4 and 5. As with the Finite Element program, this model comprises two parts. An input datafile (s.dat) is generated by the "front-end" program EDGE, which contains the locations and dimensions of the electrode subareas, and all simulation output format instuctions. This datafile is read by a generic Moments simulation package (FieldGen) which follows the procedures described in section 2.3, to which references are made throughout the program. Program output is in the form of three electric field files Ex.dat, Ey.dat and Ez.dat, a charge density list cd.dat and a potential file vo.dat. These files contain a list of values which should be organised into a rectangular mesh of the preset dimensions.

```
c       EDGE ::     A PROGRAM FOR GENERATING ELECTRODE SOURCE
c                   DATA FILES FOR TRAVELLING WAVE ANALYSIS.
c                   FOR USE WITH THE FieldGen D.E.P. FIELD SIMULATOR.
c
c       written by  MICHAEL PYCRAFT HUGHES, IMBE, BANGOR
c
c
c
c
c       PART 1 :: Variable declarations
c
        DIMENSION ev(3000),xo(3000),yo(3000),zo(3000)
        DIMENSION lz(3000),lx(3000),ly(3000)
        DIMENSION xqp(3000),yqp(3000),zqp(3000),xe(3000)
        DIMENSION v(3000),ye(3000),ze(3000)
        REAL      rot,ev,beta,alpha1
        CHARACTERplane,test2,mode,rplane
        INTEGER   nt,nx0,ny0,nz0,test,d1,d2,d3,xsm,ysm,zsm,nplanes,n1
        INTEGER   xo,yo,zo,xoffset,yoffset,zoffset,lx,ly,lz,n2,x0,y0
        INTEGER   dx,dy,dz,repetitions,ratio,alpha
        OPEN      (10,file='s.dat',status='new')
c
c
c
c
c       PART 2 :: Simulation Data
c
c       Read in angle of primary wave
        print *,' '
        print *,' '
        print *, 'EDGE: the Travelling Wave Electrode Simulation Generator'
        print *,' '
        print *,'Please enter primary wave angle (whole degrees) :'
        read *,alpha
        alpha1=float(alpha)*0.0175
c
c       Set the number of travelling-wave electrode pairs to be simulated
        repetitions=8
        print *,'Electrode pairs simulated :',repetitions+1
c
c       Size of the volume to be analysed in x,y,z directions
        d1=40
        d2=40
        d3=0
c
c       Define the offset of the simulation output volume, relative to the origin
        xoffset=95
        yoffset=-5
        zoffset=0
```

```
c
c       No. of samples in each direction
        nx0=40
        ny0=40
        nz0=1
c
c       Electric field gradient resolution; set the distance of extra sample points
c       from the central output point
        xsm=1.0
        ysm=1.0
        zsm=1.0
c
c       Point charge distribution; set the size of all subareas
        dx=2
        dy=4
        dz=1
c
c
c
c       PART 3 :: Electrode Geometry
c
c       Divide the electrodes into subareas, based on the division of the electrode
c       surfaces into rectangular planes which are further divided into subaareas.
c       Parameters xo, yo, zo are the plane corner coordinates; lx, ly and lz are
c       dimensions
        k=0
        xo(1)=30
        yo(1)=-20
        zo(1)=0
        ly(1)=40
        lz(1)=1
        ev(1)=10*cos(alpha1)
        m=1
        call divrec(xqp,yqp,zqp,xe,ye,ze,v,1,
     1          xo(m),yo(m),zo(m),1,ly(m),lz(m),1,dy,dz,k,ev(m))
        xo(2)=30
        yo(2)=-20
        zo(2)=0
        lx(2)=10
        lz(2)=1
        ev(2)=10*cos(alpha1)
        m=2
        call divrec(xqp,yqp,zqp,xe,ye,ze,v,2,
     1          xo(m),yo(m),zo(m),lx(m),1,lz(m),dx,1,dz,k,ev(m))
        xo(3)=30
        yo(3)=20
        zo(3)=0
        lx(3)=10
        lz(3)=1
```

```
ev(3)=10*cos(alpha1)
m=3
call divrec(xqp,yqp,zqp,xe,ye,ze,v,2,
1        xo(m),yo(m),zo(m),lx(m),1,lz(m),dx,1,dz,k,ev(m))
xo(4)=40
yo(4)=-20
zo(4)=0
ly(4)=40
lz(4)=1
ev(4)=10*cos(alpha1)
m=4
call divrec(xqp,yqp,zqp,xe,ye,ze,v,1,
1        xo(m),yo(m),zo(m),1,ly(m),lz(m),1,dy,dz,k,ev(m))
xo(5)=30
yo(5)=-20
zo(5)=1
lx(5)=10
ly(5)=40
ev(5)=10*cos(alpha1)
m=5
call divrec(xqp,yqp,zqp,xe,ye,ze,v,3,
1        xo(m),yo(m),zo(m),lx(m),ly(m),1,dx,dy,1,k,ev(m))
c
c
c       Copy the first electrode electrode a distance lmove along in the x direction.  A
c       further distance linx, liny per electrode in the x, y directions.  This generates a
c       further set of subareas with centre coordinates xqp, yqp, zqp and lengths xe,
c       ye, ze.
        lmove=20
        linx=0
        liny=0
        ktotal=k
        linxtotal=0
        linytotal=liny
        do 1102 i=1,repetitions
        lplanex=(lmove*i)+linxtotal
        lplaney=linytotal
        do 1101 j=1,ktotal
        x=xqp(j)
        y=yqp(j)
        z=zqp(j)
        xem=xe(j)
        yem=ye(j)
        zem=ze(j)
        vm=V(j)
        k=k+1
        call tw(i,lplanex,lplaney,
        1        x,y,z,xem,yem,zem,xqp,yqp,zqp,xe,ye,ze,V,vm,k,alpha)
1101    continue
```

```
      linxtotal=linxtotal+linx*i
      linytotal=linytotal+liny
1102  continue
c
c
c     generate oppsing electrodes (for zero charge) by mirroring the first set along
      the centre of the channel
c
      call mirror(xqp,yqp,zqp,xe,ye,ze,V,70,k)
c
c
c
c     PART 4 :: Write results to file
c     (nt is the total number of subareas)
      nt=k
      print *,'number of charges:', nt
      print *,'The source datafile (s.dat) is currently being generated'
      write(10,*) nt,nx0,ny0,nz0,d1,d2,d3,xsm,ysm,zsm,xoffset,yoffset,
      1       zoffset
      do 2 m=1,nt
      write(10,*) xqp(m),yqp(m),zqp(m),xe(m),ye(m),ze(m),v(m)
2     continue
      close(10)
      print *,' '
      print *,'File generation complete. Type RUN FGX (or FGE) to begin'
      print *,'simulation or SUBMIT the appropriate NEW batch statement'
      print *,' '
      print *,'  ** Remember to RENAME the s.dat file if necessary **'
      stop
      end
c
c
c
c
c     Subroutines
c
c
c
c
c     Divide subareas into rectangles, generate co-ordinates and lengths
c     for charge calculation
c
      subroutine divrec(xqp,yqp,zqp,xe,ye,ze,v,plane,
      1       xo,yo,zo,dim1,dim2,dim3,n1,n2,n3,k,ev)
      dimension xqp(3000),yqp(3000),zqp(3000),xe(3000)
      dimension ye(3000),ze(3000),v(3000)
      integer xo,yo,zo,plane,dim1,dim2,dim3,n1,n2,n3
      delta1=float(n1)
      delta2=float(n2)
      delta3=float(n3)
```

```
      if (plane.eq.1) goto 310
      if (plane.eq.2) goto 320
      if (plane.eq.3) goto 330
310   do 311 m=1,dim3/n3
      do 311 j=1,dim2/n2
      k=k+1
      v(k)=ev
      xqp(k)=xo
      yqp(k)=yo+dim2-float(j)*delta2+0.5*delta2
      zqp(k)=zo+dim3-float(m)*delta3+0.5*delta3
      xe(k)=0
      ye(k)=delta1
      ze(k)=delta2
311   continue
      goto 300
320   do 321 m=1,dim3/n3
      do 321 i=1,dim1/n1
      k=k+1
      v(k)=ev
      xqp(k)=xo+dim1-float(i)*delta1+0.5*delta1
      yqp(k)=yo
      zqp(k)=zo+dim3-float(m)*delta3+0.5*delta3
      xe(k)=delta1
      ye(k)=0
      ze(k)=delta2
321   continue
      goto 300
330   do 331 m=1,dim2/n2
      do 331 j=1,dim1/n1
      k=k+1
      v(k)=ev
      xqp(k)=xo+dim1-float(j)*delta1+0.5*delta1
      yqp(k)=yo+dim2-float(m)*delta2+0.5*delta2
      zqp(k)=zo
      xe(k)=delta1
      ye(k)=delta2
      ze(k)=0
331   continue
300   continue
      return
      end
c
c     Copy existing electrode to new location
c
      subroutine tw
     1     (i,lpx,lpy,x,y,z,xem,yem,zem,xqp,yqp,zqp,xe,ye,ze,V,vm,k,ndeg)
      dimension xqp(3000),yqp(3000),zqp(3000),xe(3000)
      dimension ye(3000),ze(3000),V(3000)
      rad=float(ndeg)*0.0175
```

```
xqp(k)=x+lpx
yqp(k)=y+lpy
zqp(K)=z
xe(k)=xem
ye(k)=yem
ze(k)=zem
a=1.57*i
V(k)=10*cos(a+rad)
return
end
c
c
c       Copy the current set of electrodes across the centre of the channel
c
        subroutine mirror(xqp,yqp,zqp,xe,ye,ze,v,cht,k)
        dimension xqp(3000),yqp(3000),zqp(3000),xe(3000)
        dimension ye(3000),ze(3000),v(3000)
        klim=k
        do 4321 i=1,klim
        k=k+1
        xqp(k)=xqp(i)
        yqp(k)=70.0-yqp(i)
        zqp(k)=zqp(i)
        xe(k)=xe(i)
        ye(k)=ye(i)
        ze(k)=ze(i)
        v(k)=-v(i)
4321    continue
        return
        end
```

```
c       FieldGen ::     A PROGRAM FOR CALCULATING THE ELECTRIC
                        FIELD, POTENTIAL AND DIELECTROPHORETIC FORCE
                        ABOUT 3D ELECTRODES.

c
c
c       PROGRAM STRUCTURE:
c
c       Section One:    Input the geometrical parameters and define the electrode
                        surfaces;
c       Section Two:    Calculate Charge distribution
c       Section Three:  Calculate fields
c       Section Four:   Subroutines & Functions
c
c
c
c
c       Variable declarations:
c
        REAL            xqp,yqp,zqp,xe,ye,ze,pot,ct
c
        INTEGER         nx0,ny0,nz0,d1,d2,d3
        INTEGER         xsm,ysm,zsm,xoffset,yoffset,zoffset
c
        DIMENSION aa(2000,2000),aai(2000),vdt(20),s(2000)
        DIMENSION xqp(2000),yqp(2000),zqp(2000),wkspace(2000)
        DIMENSION xe(2000),ye(2000),ze(2000),v(2000),cd(2000)
        DIMENSION xdt(20),ydt(20),zdt(20),ex(2000),ey(2000),ez(2000)
c
        OPEN            (20,file='s.dat',status='old')
        OPEN            (60,file='vo.dat', status='new')
        OPEN            (61,file='ex.dat',status='new')
        OPEN            (62,file='ey.dat',status='new')
        OPEN            (63,file='ez.dat',status='new')
        OPEN            (64,file='cd.dat',status='new')
c
c
c       Variables list:
c       nt - total number of subareas           ct - total electrode charge
c       cd - subarea charge density list        v - potential on subareas
c       aa - charge-relationship matrix         aai - as aa, in list form
c       nx0, ny0, nz0 - dimensions of the study volume
c       d1, d2, d3 - number of output samples in the x, y and z directions
c       xsm, ysm, zsm - distances of extra field sample points from the master points
c       xoffset, yoffset, zoffset - offset of simulation volume from origin
c       xqp, yqp, zqp - coordinates of subarea centres
c       xe,ye,ze - subarea dinensions
c       xdt, ydt, zdt - coodinates of electric field sample grid
c       ex, ey, ez - electric field at a given node
```

```
c       SECTION ONE :: READ AND DIVIDE THE ELECTRODE PLANES
c
c       This section will read in the dimensions of the planes from
c       the electrode plane by plane, dividing the planes into
c       subrectangles as it goes.  Parameters: x,y,zqp: co-ordinates of
c       subarea centre;  x,y,ze: dimensions; v:: potential
c
        read(20,*)
        1 nt,nx0,ny0,nz0,d1,d2,d3,xsm,ysm,zsm,xoffset,yoffset,zoffset
        print *,'Analysing Electrode Parameters....'
        do 21 m=1,nt
        read(20,*) xqp(m),yqp(m),zqp(m),xe(m),ye(m),ze(m),v(m)
21      continue
        print *,'Done.'
c
c       .
c
c       SECTION TWO ::  CHARGE CALCULATUIONS
c
c
c       This section will generate the Charge-Potential-Relation Matrix
c       AA(ntotal,ntotal). aa(i,j) means the potential at point
c       (xqp(i),yqp(i),0) caused by a unit charge at the subarea
c       (xqp(j),yqp(j),0). Then it will use intrinsic function F04ARE to
c       solve the equation ' AA*CD=V'  (equation 2.51 in Thesis text)
c       to obtain the charge distribution vector CD.
c
c
        print *,'Calculating charge distribution....'
        print *,'stage 1: coefficient matrix'
        do 50 i=1,nt
        xv=xqp(i)
        yv=yqp(i)
        zv=zqp(i)
        ntotal=nt
        call Mtrx(aai,xv,yv,zv,xqp,yqp,zqp,d1,d2,ntotal,xe,ye,ze)
        do 50 j=1,nt
        aa(i,j)=aai(j)
50      continue
        print *,'stage 2: charge'
        ifail=0
        call f04ARE(aa,2000,v,nt,cd,wkspce,ifail)
        print *,'Done.'
        ct=0
        do 25 i=1,nt
        ct=ct+cd(i)
        write(64,*) cd(i)
25      continue
c
```

```
c       SECTION THREE :: FIELD CALCULATIONS
c
c
c
c       Calculate the position of  the 6 extra points around the sample point to
c       calculate the electric field.
c
c
        print *,'Calculating field and potential....'
        do 200 i=1,7
        xdt(i)=0.0
        ydt(i)=0.0
        zdt(i)=0.0
200     continue
        ydt(2)=ysm
        ydt(3)=-ysm
        xdt(4)=-xsm
        zdt(5)=-zsm
        xdt(6)=xsm
        zdt(7)=zsm
c
c
c       Calculation of the potentials of points at the space between the
c       electrode determined by Nx0,Ny0 (No.of Divisions of interval between
c       the electrodes)
c
c
        k=0
        xdelta=d1/float(nx0)
        ydelta=d2/float(ny0)
        zdelta=d3/float(nz0)
        zco=3.1
        do 700 m=1,nz0
        zco=zco+zdelta
        yco=-ydelta*0.5+float(yoffset)
        do 700 j=1,ny0
        yco=ydelta+yco
        xco=-xdelta*0.5+float(xoffset)
        do 700 i=1,nx0
        xco=xco+xdelta
        k=k+1
        xup(k)=xco
        yup(k)=yco
        zup(k)=zco
700     continue
        npoint=nx0*ny0*nz0
        do 750 i=1,npoint
        do 745 k=1,7
        xu=xup(i)+xdt(k)
        yu=yup(i)+ydt(k)
        zu=zup(i)+zdt(k)
```

```
      call Mtrx(aai,xu,yu,zu,xqp,yqp,zqp,d1,d2,nt,xe,ye,ze,na)
      call mulmatr(pot,aai,cd,ntotal)
      vdt(k)=pot
745   Continue
      calv(i)=vdt(1)
      ex(i)=(vdt(6)-VDT(4))/(2.0*xsm)
      ey(i)=(vdt(2)-VDT(3))/(2.0*ysm)
      ez(i)=(vdt(7)-vdt(5))/(2.0*zsm)
      write(60,*) calv(i)
      write(61,*) ex(i)
      write(62,*) ey(i)
      write(63,*) ez(i)
750   continue
      end
c
c
c
c
c     SECTION FOUR :: SUBROUTINES AND FUNCTIONS
c
c
c
c
c
c     Calculate the charge-potential relation by evaluating equation 2.47
c
c
      subroutine Mtrx(aai,xv,yv,zv,xqp,yqp,zqp,d1,d2,nt,xe,ye,ze)
      dimension aai(2000),xqp(2000),yqp(2000),zqp(2000)
      dimension ye(2000),ze(2000),xe(2000)
      real xcq,ycq,xl,yl,d1,d2,s1,xmax, xv,yv,zv,xmq,ymq,zmq,xq,yq,zq
      do 120 j=1,nt
      xq=xqp(j)
      yq=yqp(j)
      zq=zqp(j)
      xl=xe(j)
      yl=ye(j)
      zl=ze(j)
      aai(j)=0.0
      s1=0.0
      do 20 iz=1,2
      if (iz.eq.1) zsign=1.0
      if (iz.eq.2) zsign=-1.0
      xmq=xq
      ymq=yq
      zmq=zq*zsign
      if (zl.eq.0.0) goto 52
      if (yl.eq.0.0) goto 54
      if (xl.eq.0.0) goto 56
52    call fdistance(xv,yv,zv,xmq,ymq,zmq,xl,yl,fdst)
```

```
      s1=fdst
      goto 50
54    call fdistance(xv,zv,yv,xmq,zmq,ymq,xl,zl,fdst)
      s1=fdst
      goto 50
56    call fdistance(zv,yv,xv,zmq,ymq,xmq,zl,yl,fdst)
      s1=fdst
50    continue
      aai(j)=aai(j)+s1
20    continue
120   continue
      return
      end
c
c
c
c
c     Calculation of the potential function caused by the charge at a
c     rectangle (equation 2.47)
c
c
      subroutine fdistance(xv,yv,zv,xcq,ycq,zcq,xL,yL,fdst)
      REAL fdst,xL,yL,xv,yv,zv
      REAL xcq,ycq,x1,x2,y1,y2,zcq
      zp=abs(zv-zcq)
      x1=xcq-xL/2.0-xv
      x2=xcq+xL/2.0-xv
      y1=ycq-yL/2.0-yv
      y2=ycq+yL/2.0-yv
      IF (((x1*x2).ge.0.0).and.((y1*y2).ge.0.0)) goto 10
      IF (((x1*x2).ge.0.0).and.((y1*y2).lt.0.0)) goto 20
      IF (((x1*x2).lt.0.0).and.((y1*y2).ge.0.0)) goto 30
      IF (((x1*x2).lt.0.0).and.((y1*y2).lt.0.0)) goto 40
      STOP
10    fdst=fcalcu(x1,y1,x2,y2,zp)
      return
20    fdst=fcalcu(x1,0.0,x2,y2,zp)+fcalcu(x1,0.0,x2,abs(y1),zp)
      return
30    fdst=fcalcu(0.0,y1,x2,y2,zp)+fcalcu(0.0,y1,abs(x1),y2,zp)
      return
40    fdst=fcalcu(0.0,0.0,x2,y2,zp)+fcalcu(0.0,0.0,x2,abs(y1),zp)
      fdst=fdst+fcalcu(0.0,0.0,abs(x1),abs(y1),zp)
      fdst=fdst+fcalcu(0.0,0.0,abs(x1),abs(y2),zp)
      return
      end
c
c
c
c
c
```

```
c       Performance of the "Multi-Matrix" operation
c       Simplest form: sum=a(1)*b(1)+a(2)*b(2)+....+a(n-1)*b(n-1)+a(n)*b(n)
c
c
        subroutine mulmatr(sum,a,b,n)
        DIMENSION a(2000),b(2000)
        REAL sum
        sum=0.
        do 220 i=1,n
        sum=sum+a(i)*b(i)
220     continue
        return
        end
c
c
c       The remaining subroutines collectively evaluate the result of equation 2.49
c
        Function fcalcu(x1,y1,x2,y2,zp)
        real x1,y1,x2,y2,fcalcu
        real xa,xb,ya,yb
        real xx1,xx2,yy1,yy2
        xx1=abs(x1)
        xx2=abs(x2)
        yy1=abs(y1)
        yy2=abs(y2)
        xa=((xx1+xx2)-abs(xx1-xx2))*0.5
        xb=((xx1+xx2)+abs(xx1-xx2))*0.5
        ya=((yy1+yy2)-abs(yy1-yy2))*0.5
        yb=((yy1+yy2)+abs(yy1-yy2))*0.5
        fx=flog(xa,ya,zp)+flog(xb,yb,zp)
        fy=flog(xa,yb,zp)+flog(xb,ya,zp)
        fcalcu=fx-fy
        return
        end
c
c
c
c
        function flog(xx,yy,zz)
        real flog,xx,yy,zz
        xys=xx*xx+yy*yy
        If (zz.gt.0.0) goto 20
        flog=0.0
        if (xx.ne.0.0) goto 10
        if (yy.ne.0.0) goto 5
        flog=0.0
        return
5       flog=yy*log(xx+sqrt(xys))
        return
```

```
10      flog=xx*log(yy+sqrt(xys))+yy*log(xx+sqrt(xys))
        return
20      continue
        fx1=yy/sqrt(xx*xx+zz*zz)
        fx2=xx/sqrt(yy*yy+zz*zz)
        flog=xx*log(fx1+sqrt(1.+fx1*fx1))
        flog=flog+yy*log(fx2+sqrt(1.+fx2*fx2))
        if ((xx.ne.0.0).and.(yy.ne.0.0)) goto 25
        flog=flog+zz*3.1415926/2.0
        return
25      fx3=zz*sqrt(xx*xx+yy*yy+zz*zz)/xx/yy
        flog=flog+zz*atan(fx3)
        return
        end
```